Aus der Radiologischen Universitätsklinik Tübingen

Abteilung für Diagnostische und Interventionelle Neuroradiologie

Ärztliche Direktorin: Professor Dr. U. Ernemann

Development of CSI without Water Suppression for the Purpose of Clinical Applications in the Human Brain

Inaugural-Dissertation
zur Erlangung des Doktorgrades
der Humanwissenschaften

der Medizinischen Fakultät
der Eberhard Karls Universität
zu Tübingen

vorgelegt von
Grzegorz Łukasz Chądzyński
aus
Katowice, Polen
2012

Dekan: Professor Dr. I. B. Autenrieth
1. Berichterstatter: Professor Dr. U. Klose
2. Berichterstatter: Professor Dr. D. Kern

Summary

Over past years proton magnetic resonance spectroscopy (^{1}HMRS) has benefited from the ongoing development in magnetic resonance imaging. Therefore it became a valuable tool which provides additional information about chemical composition of the tissue and together with magnetic resonance imaging (MRI) deliver more comprehensive information about various pathologies such as: tumors or neurodegenerative diseases.

Thanks to the recent hardware improvements (development of 16 and 32 bit analog-to-digital converters) MRS without water suppression has become feasible. This technique enables the measurements of the full water signal without any losses in the sensitivity of detecting much smaller metabolite resonances. Water signal may be then used for baseline and phase correction as well as an internal reference for absolute quantification of metabolite concentrations. However, non-water-suppressed proton spectra are hampered by the sideband artifacts. Those originate from the mechanical vibration of the gradient coils and lead to sinusoidal perturbations of the static magnetic field. This result in spurious peaks placed symmetrically around the water signal which are overlapped with the metabolite resonances and thus need to be reduced. An additional problem is the presence of the unsuppressed water signal which is typically three to six orders in magnitude greater than metabolite resonances. Consequently its tail may be overlapped with the spectral baseline. Therefore, this signal has also to be reduced before quantification of the metabolites. To overcome these problems and to implement the non-water-suppressed MRS it was necessary to optimize the existing acquisition methods and to develop special postprocessing routines.

The aim of the thesis was to develop a reliable non-water suppressed MRSI technique, to test its performance in *in-vivo* measurements and to find possible applications in which it could be used.

All measurements were carried out on 3T whole body clinical MR scanner (TimTrio, Siemens, Erlangen, Germany). In all the cases chemical shift imaging (CSI) was performed with point resolved spectroscopy sequence (PRESS). All software necessary for postprocessing and visualization of non-water-suppressed spectra was written with Matlab (MathWorks, Natick, MA, USA).

Measurements of the gradient induced sidebands demonstrated that for the used magnet and gradient systems, the strongest artifacts occur between 3 and 4 ppm, therefore resonances of myo-inositol (mI), choline (Cho) and creatine (Cr) are mostly affected. Additionally it was shown that sidebands are linear dependent from the strength of the crusher gradient pulses and the strongest artifacts are associated with the gradient in *x*-direction. Subsequently the performance of the PRESS sequence with the optimized crusher gradients has been tested. This revealed that it is possible to reduce the strength of the crushers from 11 to 5 mT/m without introducing additional distortions due to insufficient spoiling of unwanted signals produced during volume selection. Moreover, *in-vivo* measurements showed that further minimization of the influence of the sidebands on non-water-suppressed spectra may be achieved by using PRESS sequence with *y*- and *z*-gradients only (without *x*-gradient, as it generates the strongest sidebands).

For the purposes of in-*vivo* validation of the developed technique a software for postprocessing and visualization of the measured spectra has been developed. Those included special routines for reducing the water signal and the sidebands. Water signal minimization was performed in time domain and consisted on subtraction of the signal convoluted with the Gauss function from the *in-vivo* free-induction decay (FID) signal. Minimization of the sideband artifacts was achieved by subtraction of the FID signal measured for water phantom from the *in-vivo* FID. Both datasets were measured with the same sequence parameters. A comparison of spectra obtained with the proposed technique and spectra measured with water suppression revealed that there were not major differences in baseline and in parameters of the metabolite peaks. Moreover it has been demonstrated that the non-water-suppressed spectra do not require additional manual phase correction which is often necessary for measurements with multichannel receive coils. This is because the unsuppressed water signal may be used as a reference for the automated phase

correction. This correction is applied by the scanner's software individually to the signals measured by the each channel of multichannel coil before calculating the final spectrum. If the water signal is distorted or its amplitude is to small the algorithm may not be able to calculate correct coefficients needed for phase correction.

Further *in-vivo* validation has been performed at the level of substantia nigra (brainstem) and in the nucleus dentatus (cerebellum). Because of high tissue inhomogeneity and elevated iron content (especially within the substantia nigra) both areas are known to be difficult to access with proton MR spectroscopy. In this thesis it was demonstrated that the developed technique combined with the manual shimming for compensation of B_0 field inhomogeneities offers the possibility to acquire high quality spectra from those regions. Moreover, as the non-water-suppressed spectra postprocessed with the proposed method do not require additional phase correction, it was possible to calculate average spectra. Those offers even higher signal-to-noise ratio (SNR) and better spectral resolution compared to the single MRSI spectrum and may be calculated from an asymmetric area which can better corresponds to the certain anatomical structures.

Since the developed technique offers the availability of unsuppressed water signal which can be quantified, it has been used for *in-vivo* determination of differences in resonance frequencies of water and metabolites between gray and white matter in the human brain. In order to avoid the influence of B_0 field inhomogeneities on the results, frequency distances between water and choline, water and creatine and water and N-acetyl aspartate (NAA) where evaluated. It has been found that for all the cases the biggest values of those frequency distances were observed for CSI voxels associated with gray matter. The greatest regional differences were observed for the water to NAA frequency distance. The same frequency difference between the frequencies of water in white and gray matter were reported in the literature as detected in phase imaging studies. This may suggest that the resonance frequency of NAA appears to be constant while the resonance frequencies of the other metabolites (Cho and Cr) could be influenced by proton exchange and susceptibility effects also seen in phase images for the water signal.

Despite the implementation of non-water-suppressed CSI involves some effort toward software development and optimization of measurement procedures, the results

presented in this dissertation proves that this technique may be feasible. In comparison to classical approach (water suppressed CSI), the presented technique provide access to the full water signal. It has been shown that full water signal can be successfully used for automated phase correction, so that non-water-suppressed spectra do not require additional phasing performed in postprocessing. In addition it has been demonstrated that quantification of water signal itself may also provide important information. Especially, the evaluation of resonance frequencies of the water and metabolite signals revealed interesting information about tissue dependent variations of those frequencies. Finally the developed technique could be beneficial at ultra-high magnetic fields where the accurate water suppression may be difficult as it requires higher bandwidth of the water-suppressing RF pulses.

Zusammenfassung

Die *in-vivo* Magnetresonanzspektroskopie (^{1}H-MRS) wurde in den vergangenen Jahren zu einer wertvollen Methode entwickelt, die zusätzliche Informationen über die chemische Zusammensetzung der Gewebe liefert und gemeinsam mit der Magnetresonanztomographie (MRT) umfassende Erkenntnisse über verschiedene Erkrankungen wie z. B. Tumore oder neurodegenerative Erkrankungen ermöglicht.

Während MRS-Messungen in der Regel mit einer Sättigung des Wassersignals durchgeführt werden, wurde durch Hardware-Verbesserungen (Entwicklung von 16 und 32 Bit Analog-Digital-Wandler) auch MRS ohne Wasserunterdrückung möglich. Diese Technik ermöglicht die Messung des gesamten Wassersignals ohne Verluste in der Empfindlichkeit bei der Detektion sehr kleiner Metabolitresonanzen. Das Wassersignal kann dann zur Basislinien- und Phasenkorrektur sowie als interne Referenz zur absoluten Quantifizierung von Metabolitkonzentrationen verwendet werden. Allerdings sind die Protonenspektren ohne Wasserunterdrückung durch die Seitenbandenartefakte gestört, die durch mechanische Vibrationen der Gradientenspulen produziert werden, welche zu sinusoidalen Störungen des statischen Magnetfeldes führen. Diese manifestieren sich als falsche Peaks, die mit den Metabolitresonanzen überlappen und daher reduziert werden müssen. Ein weiteres Problem ist die Dominanz des nicht unterdrückten Wassersignals, das typischerweise drei bis sechs Größenordnungen größer ist als das der Metabolitresonanzen. Folglich kann der Fuß des Wassersignals die spektrale Basislinie überlagern, so dass dieses Signal vor der Quantifizierung der Metabolite reduziert werden muss. Um diese Probleme zu überwinden und die MRS ohne Wasserunterdrückung umzusetzen, war es notwendig, die bestehenden Aufnahmemethoden zu optimieren und spezielle Nachbearbeitungsroutinen zu entwickeln.

Das Ziel der Doktorarbeit war es, eine verlässliche MRS-Technik ohne Wasserunterdrückung zu entwickeln, ihre Leistungsfähigkeit in *in-vivo* Messungen zu

testen und mögliche Anwendungen zu finden, die durch den Verzicht auf die Wassersättigung ermöglicht werden.

Alle Messungen wurden an einem klinischen 3T-Ganzkörper-MR-Tomographen (TimTrio, Siemens, Erlangen, Deutschland) durchgeführt. In allen Fällen wurden für die MRS-Messungen eine spezielle PRESS-Sequenz verwendet. Sämtliche Software, die für die Nachbearbeitung und Visualisierung der Spektren ohne Wasserunterdrückung notwendig war, wurde in Matlab (MathWorks, Natick, MA, USA) programmiert.

Messungen der gradienteninduzierten Seitenbänder zeigten, dass für die verwendeten Magnet- und Gradientensysteme die stärksten Artefakte zwischen 3 ppm und 4 ppm auftreten, also die Resonanzen von *myo*-Inositol (mI), Cholin (Cho) und Kreatin (Cr) am meisten betroffen sind. Zusätzlich wurde gefunden, dass die Seitenbänder linear abhängig sind von der Stärke der Gradientenpulse und die stärksten Artefakte mit dem Gradienten in x-Richtung verbunden sind. Bei der Untersuchung der Leistungsfähigkeit der PRESS-Sequenz mit optimierten Gradientenpulsen zeigte sich, dass es möglich war, die Stärke dieser speziellen Gradientenpulse von 11 auf 5 mT/m zu reduzieren, ohne zusätzliche Verzerrungen zu erzeugen, die aufgrund einer unzureichenden Dephasierung der unerwünschten Signale während der Volumenauswahl auftreten können. Darüber hinaus zeigten *in-vivo* Messungen, dass durch die Verwendung einer PRESS-Sequenz, bei der nur y- und z-Gradienten für die Signaldephasierung eingesetzt wurden, eine weitere Minimierung des Einflusses der Seitenbänder auf Spektren ohne Wasserunterdrückung erreicht werden kann.

Für eine Validierung der entwickelten Technik *in vivo* wurde ein Computerprogramm für die Nachbearbeitung und Visualisierung der gemessenen Spektren entwickelt. Dieses enthält spezielle Routinen zur Reduzierung des Wassersignals und der Seitenbänder. Die Minimierung des Wassersignals wurde im Zeitbereich durchgeführt und bestand aus der Subtraktion des mit einer Gauß-Funktion gefalteten Signal von dem ursprünglichen *in-vivo* Zeitsignal. Die Minimierung der Seitenbandartefakte wurde mittels Subtraktion des in einem Wasserphantom gemessen Zeitsignals realisiert. Im Signal des Wasserphantoms werden weitgehend identische Seitenbandsignale erwartet, es sind aber keine Metabolitensignale vorhanden. Beide Datensätze wurden mit den gleichen

Sequenzparametern gemessen. Ein Vergleich der Spektren, die mit und ohne Wasserunterdrückung gemessen wurden, ergab eine weitgehende Übereinstimmung bei der Darstellung der Metabolitensignale.

Zusätzlich wurde eine in vivo Validierung bei Probandenmessungen in der Höhe der Substantia Nigra (Mittelhirn) und des Nukleus Dentatus (Kleinhirn) durchgeführt. Aufgrund der großen Gewebeinhomogenitäten und der erhöhten Eisenkonzentrationen speziell in der Substantia Nigra gelten beide Regionen als schwierig für die 1H-MRS. In dieser Arbeit wurde gezeigt, dass die entwickelte Technik in Kombination mit einer manuellen Shimprozedur zur Kompensation von B_0-Feldinhomogenitäten die Möglichkeit bietet, Spektren mit hoher Qualität in diesen Regionen zu erhalten. Da die Spektren bei einem Verzicht auf die Wasserunterdrückung keine zusätzliche Phasenkorrektur erforderten, wenn sie nach der verwendeten Methode nachverarbeitet worden sind, war es möglich, gemittelte Spektren zu berechnen. Diese zeigten ein besseres Signal-zu-Rausch-Verhältnis und eine geringere Linienbreite verglichen mit Einzelvolumenspektren. Sie könnten auch von asymmetrischen Regionen berechnet werden, die besser mit den untersuchten anatomischen Strukturen übereinstimmen.

Da die entwickelte Technik ein nicht unterdrücktes Wassersignal liefert, für das sowohl die Amplitude als auch die genaue Resonanzfrequenz bestimmt werden können, kann sie für die Bestimmung von Unterschieden in der Resonanzfrequenzen von Wasser und Metaboliten *in-vivo* in grauer und weißer Substanz des menschlichen Gehirns eingesetzt werden. Durch die Bestimmung von Frequenzabständen wird der Einfluss von B_0-Feldinhomogenitäten auf die Ergebnisse vermieden. Es wurden die Frequenzabstände zwischen Wasser und Cholin, Wasser und Kreatin und Wasser und N-Acetylaspartat (NAA) ausgewertet. Es hat sich gezeigt, dass die größten Werte für diese Frequenzabstände für Voxel, die mit grauer Substanz assoziiert waren, beobachtet wurden. Zusätzlich wurden die größten regionalen Unterschiede für den Frequenzabstand zwischen Wasser und NAA beobachtet. Diese Unterschiede waren vergleichbar mit denen, die in der Literatur für die Resonanzfrequenz des Wassersignals in weißer und grauer Substanz in Phasenmessungen gefunden werden. Daraus könnte man ableiten, dass die Resonanzfrequenz von NAA konstant ist, während die Resonanzfrequenzen der anderen Metaboliten (Cho und Cr) durch

Protonenaustausch und Suzeptibilitätseffekte ähnlich beeinflusst werden, wie es in der Phasen bildgebung für Wasserstoffkerne gezeigt wurde.

Im Vergleich zum „klassischen" Ansatz (MRSI mit Wasserunterdrückung) bietet die vorgestellte Technik Zugriff auf das gesamte Wassersignal. Dieses kann zur absoluten Quantifizierung der gemessenen Metabolite oder zur Basislinien- und Phasenkorrektur verwendet werden. Es hat sich gezeigt, dass das vollständige Wassersignal erfolgreich für eine automatisierte Phasenkorrektur verwendet werden kann, so dass Spektren ohne Wasserunterdrückung keine zusätzliche Phasenkorrektur während der Nachbearbeitung benötigen. Darüber hinaus wurde nachgewiesen, dass die Quantifizierung des Wassersignals selbst wichtige Informationen liefern kann. Nicht zuletzt könnte sich die entwickelte Messtechnik im Ultrahochmagnetfeld als sinnvoll erweisen. In diesem Umfeld ist eine präzise Wasserunterdrückung sehr schwierig, da hier eine höhere Bandbreite der Wasserunterdrückungspulse notwendig ist.

Table of Contents:

Chapter 1:
Introduction

In-vivo proton magnetic resonance imaging (^{1}H MRI) in clinical practice utilizes the magnetic properties of the hydrogen nuclei for the purposes of the diagnostic. Years of development of MRI enabled to measure various physical properties such as: relaxation times, proton density, diffusion, perfusion and chemical shift. This resulted in an expansion of different MR modalities which employ those properties. One can distinguish the following: T_1, T_2 and proton density (PD) weighted imaging, functional MRI (fMRI), diffusion weighted imaging and diffusion tensor imaging (DWI, DTI), perfusion imaging (PWI) and finally MR spectroscopy (MRS) and MR spectroscopic imaging (MRSI). The scope of this thesis is magnetic resonance spectroscopy, particularly, magnetic resonance spectroscopy imaging (MRSI), also known as chemical shift imaging (CSI).

The nuclear magnetic resonance (NMR) phenomenon was discovered simultaneously in 1946 by two independent research groups: the group of Edward M. Purcell [1] (University of Cambridge) and the group of Felix Bloch [2, 3] (University of Stanford). The principle of this phenomenon is that in the presence of a strong external magnetic field each nucleus performs a precession with a characteristic frequency. This is described by the Larmor equation and the frequency is called the Larmor frequency. MRS employs the fact that the protons are immersed in the local magnetic field, which is slightly different from the field produced by the magnet alone [4]. This is because the nucleus is surrounded by a cloud of electrons which provides the shielding from an external magnetic field. Since the structure of the electron cloud is characteristic to molecule or compound, the scale of the shielding effect will be characteristic to the environment of single nuclei. Due to this effect, different chemical compounds are producing slightly different local magnetic fields. This results in a chemical shift of the local Larmor frequency from the main frequency of the sample and is the basis of MR spectroscopy [4, 5].

First MR spectra were recorded in a continuous wave mode. This could be realized in two approaches: either the radio frequency was swept through the sample while the magnetic field was fixed, or the magnetic field was swept through the sample in the presence of constant radio frequency [6]. The first pulsed NMR scans combined with the Fourier transformation were acquired in 1966 by Ernst and Anderson [7]. Since then pulsed or Fourier transform NMR is an integral part of all modern NMR systems [6].

The progress in MRS was ongoing in parallel to the development of the various MRI techniques. Spectroscopy benefited from the evolution of the MR hardware which was induced by expansion of different MRI modalities and evolved from a simple radio-frequency (RF) pulse sequences to a complex techniques including: spatial localization, water and lipid suppression, spectral editing or ultra-fast and multi-parametric acquisition schemes for MRI [6]. Recently the sensitivity of *in-vivo* MRS in detecting various metabolites was improved by moving from 1.5 T or 3 T to ultra-high magnetic fields like: 7 T [8], 9.4 T [9] (humans) or even 16.4 T (rodents) [10].

Furthermore, recent progress in the field of hardware enabled the development of 16 and 32 bit analog-to-digital converters (ADC) which allowed sampling the entire water signal without losses in sensitivity of sampling the metabolite resonances. This technique enables the simultaneous detection of the water and metabolite signals. The main drawback of MR spectroscopy without water suppression is the presence of unwanted sideband artifacts, which are associated with the mechanical vibration of the gradient coils during the measurement [11]. The main advantage of this technique is the availability of the full water signal which can be used for the absolute quantification of the metabolites [12] or for non-invasive mapping of such physiological parameter like temperature [13] and pH [14].

MRS without water suppression provides an additional information about the water signal. However, due to the presence of sideband artifacts this technique demands a development of methods which will reduce their influence on measured spectra. Because of this, it is necessary to perform an *in-vivo* validation before using this technique for clinical applications. On the other hand non-water suppressed MRS avoids some problems which may influence spectra acquired with conventional MRS. Altogether, this gives an evidence that non-water suppressed CSI may have a high potential to be used in the field of clinics.

1.1 Aim of the work

The main aim of this thesis was to develop a reliable non-water-suppressed MRSI technique and to test its performance in *in-vivo* measurements. Since this technique requires

development and optimization of the acquisition and postprocessing methods, the following sub-aims can be distinguished:

Assessment of the gradient induced sideband artifacts

The aim of this part was to determine which of the crusher gradients have the most influence on the intensity of the sideband artifacts present in non-water suppressed spectra. Additionally, the potential possibilities of optimization of the crusher gradients in point resolved spectroscopy (PRESS) sequence for the purpose of chemical shift imaging (CSI) without water suppression were investigated. This sub-aim is described in chapter 3.

In-vivo **validation**

The aim of this part was to develop a fast and easy postprocessing method to apply CSI without water suppression in clinical routine with reduced sideband artifacts. The time-domain water signal was modeled using a low-pass filter calculated with Gaussian convolution. Subsequently this modeled signal was subtracted from the original data, which resulted in reduction of the water signal. For the reduction of the sidebands, a free induction decay (FID) signal measured for the water phantom was subtracted from the *in-vivo* FID. Finally the non-water suppressed spectra were compared with the spectra obtained with water suppression. Development of acquisition and postprocessing strategies together with *in-vivo* validation are described in chapter 4.

The robustness of the developed technique was confirmed in further *in-vivo* measurements performed at the level of substantia nigra (within the brainstem) and nucleus dentatus (within the cerebellum). Those particular regions are known to introduce B_0 field inhomogeneities thus, are difficult to access with MRSI. Since spectra acquired from both of regions may provide relevant information about different pathologies, the aim was to demonstrate the feasibility of high resolution non-water-suppressed MRSI. As the developed technique allows to acquire spectra without phase problems, the possibility of calculating the average spectrum was also examined. Such spectrum could be calculated for a number of voxels from an asymmetric region which could better correspond to the certain

anatomical structures therefore, an improvement in SNR and spectral resolution could be expected. This sub-aim is described in chapter 5 of the thesis.

Potential application

The developed stable postprocessing method for spectra acquired without water suppression allowed to access the unsuppressed water signal. Among many parameters, particularly the spatial distribution of resonance frequency of water signal revealed to be off interest. In this part non-water suppressed *in-vivo* spectra from the gray and white matter (GM and WM) were compared and the differences between the resonance frequencies and water and metabolites were analyzed. The aim was to determine if there are any regional differences in those frequencies. Furthermore, the potential influence of the chemical shift displacement effect on the mentioned frequency differences was evaluated. The work done in this field is described in chapter 6.

Chapters which are describing the realization of the aims of the thesis were published as separate manuscripts therefore their original structure was preserved. The only exception is the research material presented in the chapter 5, which is currently under preparation and will shortly be submitted. Parts of this chapter were published in the book of abstracts of 'The World Congress on Medical Physics and Biomedical Engineering' conference (IFMBE Proceedings 2009;25/2:177-180) which took place in Munich in 2009.

In the dissertation those manuscripts were organized to follow the logical order determined by the aims of the thesis. However, the chronological order of publishing those manuscripts was different: the manuscript presented in the chapter 4 was published as the first one, the second was the manuscript presented in the chapter 6, the manuscript presented in the chapter 3 was submitted as the third and the last one was the manuscript which is presented in the chapter 5 (currently under preparation). This may explain why the approach for minimization of the sideband artifacts presented in the third chapter was not used to acquire non water-suppressed spectra described in subsequent chapters.

Prior to the mentioned chapters a brief overview of theory is given. The theoretical part of the thesis incorporates all the physical description which facilitates understanding of the results section (chapters 3 to 6). This theory is presented in the chapter 2 of the thesis.

The last part of the thesis focuses on a brief summary and common conclusions, which can be drawn from the presented results. This has been gathered in the chapter 7 of the thesis.

Chapter 2:
Theory

2.1   Spins in the magnetic field- quantum approach

In quantum mechanics the angular momentum of each particle is quantized (can have a certain values only) and is given by:

$$P = \left(\frac{h}{2\pi}\right)\sqrt{I(I+1)}$$

(2.1)

where h is the Planck's constant and I is the quantum spin number (can only be integral or half integral). The direction of the angular momentum is specified by a second quantum number m, which is also discrete and can have only certain values (m = I, I-1, I-2, …, -I) with respect to the given direction.

Similarly to the classical theory, in quantum mechanics the relation between the angular momentum and the magnetic moment μ (quantized) is described by:

$$\mu = \gamma P$$

(2.2)

where γ is the gyromagnetic ratio. The gyromagnetic ratio is characteristic to each nuclei. The direction of the magnetic momentum is also described by the quantum number m.

In the presence of an external magnetic B_0, field the particle acquires energy. The energy of this particle is described by the following equation:

$$E = -\mu B_0 = -\gamma\left(\frac{h}{2\pi}\right)m B_0$$

(2.3)

As m is quantized the energy levels will be also quantized. For a hydrogen nuclei the quantum spin number I is equal to ½, so the quantum number m can only be ½ or -½, which represents the parallel and the anti-parallel direction of the magnetic moment to the direction of the B_0 field. Therefore, there are two possible energy levels:

$$E_1 = \frac{1}{2}\gamma \left(\frac{h}{2\pi}\right) B_0$$

(2.4)

$$E_2 = -\frac{1}{2}\gamma \left(\frac{h}{2\pi}\right) B_0$$

(2.5)

This splitting of the energy levels is called the Zeeman effect.

The energy which induces the passage of the spins between those two energy levels can be delivered by an application of an electro-magnetic pulse. However, this will happen only when the electro-magnetic pulse will carry the energy identical to the gap between E_1 and E_2. Since the energy of the electro-magnetic pulse is described by its frequency and is equal to $h\upsilon_0$, the resonance condition is given by:

$$E_1 - E_2 = \Delta E = h\upsilon_0 = \gamma \left(\frac{h}{2\pi}\right) B_0 \Rightarrow \upsilon_0 = \left(\frac{\gamma}{2\pi}\right) B_0$$

(2.6)

The last segment is the Larmor equation. Since the gyromagnetic ratio is constant for a given nucleus, the resonance frequency will only depend from the external magnetic field B_0. The resonance frequency υ_0 is called the Larmor frequency.

In the presence of the external field B_0 the spins will be randomly distributed between the parallel (n_α) and anti-parallel (n_β) states. Since the energy difference between those states is small, there will be a small difference in the population of those spin states. This difference in the spin populations is described by a Boltzman relation:

$$\frac{n_\alpha}{n_\beta} = exp\left(\frac{\Delta E}{kT}\right) = exp\left(\frac{h\upsilon}{kT}\right)$$

(2.7)

An equal distribution of the spins between the n_α and n_β states will occur only for very high temperatures (as the value inside the exponent in eq. 2.7 goes to zero). For a

typical *in-vivo* temperature (36.6 C°) a small surplus of spins in parallel direction will create the macroscopic magnetization M_0 parallel to the direction of the B_0 magnetic field. The basis of the MRI experiment consists in measuring of this magnetization.

2.2   Bloch equations in the presence of relaxation

In addition to the static magnetic field B_0, MR experiment employs the radio-frequency (RF) pulses used for excitation of the spin system. Those pulses are addressed as a variable magnetic field B_1. The excitation with the RF pulses will cause the magnetization to execute the motion. Considering the combined effect of B_0 and B_1 fields on the components of the magnetization (M_x, M_y and M_z) will lead to the following:

$$\frac{dM_x(t)}{dt} = \gamma\big[M_y(t)B_0 - M_z(t)B_1\sin(\omega t)\big]$$

(2.8)

$$\frac{dM_y(t)}{dt} = \gamma[M_z(t)B_1\cos(\omega t) - M_x(t)B_0]$$

(2.9)

$$\frac{dM_z(t)}{dt} = \gamma\big[M_x(t)B_1\sin(\omega t) - M_y(t)B_1\cos(\omega t)\big]$$

(2.10)

These are the Bloch equations in the laboratory reference frame and without the influence of the relaxation processes. The laboratory reference frame can be identified with the NMR system, where the x and y axes perpendicular and z axis parallel to the direction of the B_0 field.

An application of a RF pulse to the population of spins will result in a disturbance of an equilibrium state in which the magnetization is parallel to the B_0 field. The magnetization vector will rotate in the transverse plane and its components (M_x, M_y and M_z) will return to the state of equilibrium in an exponential manner. This process of returning to the equilibrium after a perturbation is called the relaxation. After excitation the

perpendicular (M_x and M_y) components of the magnetization vector will relax with a different time constant than the parallel component (M_z). This is described by the following equations:

$$\frac{dM_x(t)}{dt} = -\frac{M_x(t)}{T_2}$$

(2.11)

$$\frac{dM_y(t)}{dt} = -\frac{M_y(t)}{T_2}$$

(2.12)

$$\frac{dM_z(t)}{dt} = -\frac{M_z(t) - M_0}{T_1}$$

(2.13)

where T_1 and T_2 are relaxation time constants describing longitudinal and transversal relaxation respectively.

Longitudinal relaxation is a process describing the return of longitudinal magnetization. During T_1 relaxation energy from the spins is transferred to the surrounding lattice (can be solid or liquid). Therefore, this process is also called the spin-lattice relaxation. The energy absorbed during excitation is converted to translational or rotational energy and the nuclei return to the lower energy state.

Transverse relaxation describes the energy exchange between the spins, therefore the T_2 relaxation is also called the spin-spin relaxation. This process describes the disappearance of the transverse magnetization. During T_2 relaxation there is no net energy transport and the spins exchange energy between themselves. Therefore, this is an entropy process, which leads to a dephasing of the spins.

Including both, longitudinal and transverse relaxation processes to the equations 2.11- 2.13 will give the complete Bloch equations in the laboratory frame [3]:

$$\frac{dM_x(t)}{dt} = \gamma \left[M_y(t)B_0 - M_z(t)B_1 \sin(\omega t) \right] - \frac{M_z(t)}{T_2}$$

(2.14)

$$\frac{dM_y(t)}{dt} = \gamma[M_z(t)B_1\cos(\omega t) - M_x(t)B_0] - \frac{M_y(t)}{T_2}$$

(2.15)

$$\frac{dM_z(t)}{dt} = \gamma[M_x(t)B_1\sin(\omega t) - M_y(t)B_1\cos(\omega t)] - \frac{(M_z(t) - M_0)}{T_1}$$

(2.16)

2.3 Free induction decay signal

An excitation with RF pulse places the magnetization M_0 in the transverse plane of the rotating frame and causes a precession about the B_0 with the Larmor frequency. This induces the signal in a receiving coil placed in the transverse plane [6]. Due to T_2 relaxation, the transverse magnetization and the measured signal will decay in time.

The time evolution of the measured signal creates the free induction decay signal (FID). Since the motion of the transverse magnetization after excitation occurs in the transverse plane, changes in magnetization M_0 can be described by a time evolution of two components M_x and M_y:

$$M_x(t) = M_0\sin[(\omega_0 - \omega)t + \varphi]\,exp\left\{-\left(\frac{t}{T_2^*}\right)\right\}$$

(2.17)

$$M_y(t) = M_0\cos[(\omega_0 - \omega)t + \varphi]\,exp\left\{-\left(\frac{t}{T_2^*}\right)\right\}$$

(2.18)

where φ refers to the phase at t=0, M_x and M_y refers to the real and imaginary parts of the FID signal respectively and T_2^* describes the changes in the T_2 relaxation time caused by the B_0 field inhomogeneities which occurs when a macroscopic sample is measured.

A spectrum (frequency domain data) is produced by an application of the Fourier transform to the time domain data (FID). This transformation is defined as:

$$F(\omega) = \int\limits_{-\infty}^{+\infty} f(t)exp(-i\omega t)dt$$

(2.19)

where f(t) is a time domain signal and i is the imaginary unit (i^2 = -1). The Fourier transformation is reversible, so the FID signal can be calculated from the frequency domain signal by an application of the inverse Fourier transformation.

Since the FID is measured as a complex signal using so-called quadrature detection [6], after Fourier transformation the frequency domain data will also be complex. Real and imaginary parts of the frequency domain signal (spectrum) are given by:

$$Re(\omega) = A(\omega) \cos \varphi - D(\omega) \sin \varphi$$

(2.20)

$$Im(\omega) = A(\omega) \sin \varphi + D(\omega) \cos \varphi$$

(2.21)

where $A(\omega)$ and $D(\omega)$ are the absorption and dispersion components of a Lorenzian lineshape respectively. Both components are shown on fig. 2.1. It can be seen that the dispersion component is broader, while the absorption component is narrower and therefore easier to evaluate. For that reason, spectra in absorption mode are more desired.

In some circumstances (i.e. when $\varphi \neq 0$) the obtained spectrum can be a mixture of absorption and dispersion components. Then, to recover the pure absorption shape an additional phasing has to be performed. This procedure is described as follows:

$$A(\omega) = Re(\omega) \cos(\varphi - \varphi_c) + Im(\omega) \sin(\varphi - \varphi_c)$$

(2.22)

$$D(\omega) = -Re(\omega) \sin(\varphi - \varphi_c) + Im(\omega) \cos(\varphi - \varphi_c)$$

(2.23)

where φ_c denotes the phase correction. A pure absorption spectrum is obtained when $\varphi_c = \varphi$. However, under some conditions (i.e. hardware imperfections) the phase may depend on

the resonance frequency and the zero-order phase correction may not be sufficient. In most of the modern MR systems phasing takes into account the zero- and first-order phase correction, which is given by:

$$\varphi_c = \varphi_0 + (\omega_0 - \omega)\varphi_1$$

(2.24)

where φ_0 is the zero-order phase (constant phase) and φ_1 is the first-order phase (linear phase).

In a situation when the phase of the signal is not relevant or it cannot be corrected properly, the spectrum may be represent in magnitude mode (absolute value). The magnitude signal is defined as:
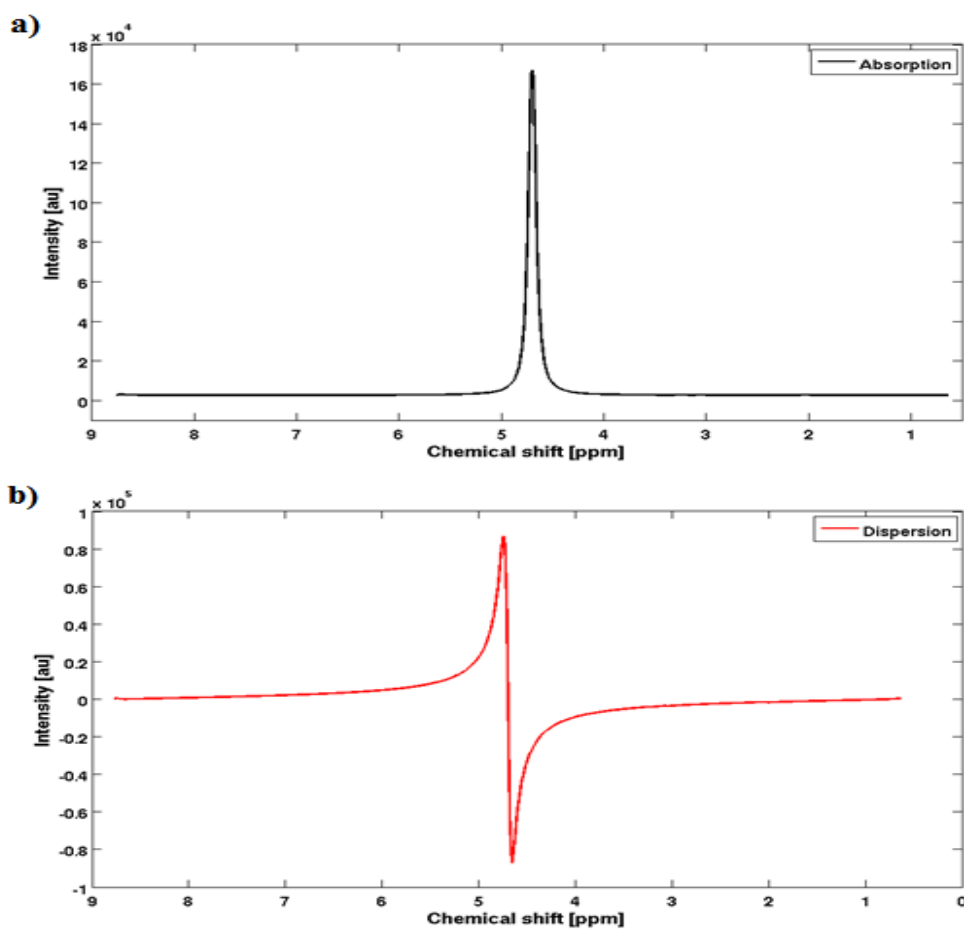

Fig. 2.1 Absorption (a) and dispersion (b) components of the spectrum

$$Abs(\omega) = \sqrt{Re(\omega)^2 + Im(\omega)^2}$$

$$(2.25)$$

Generally the resonances in spectra presented in magnitude mode are broader, because they contain the dispersive component. Moreover, in the case of *in-vivo* MR spectroscopy, this broadening of the resonances causes the overlap between different metabolite peaks to be higher. As a consequence, quantification of magnitude spectra would be more complicated and is usually not performed.

2.4   Chemical shift

In *in-vivo* situation measured sample contains multiple nuclei. Each single nucleus is surrounded by a cloud of electrons which will provide the screening from the external magnetic field. The screening effect is described with the following equation:

$$B = B_1(1 - \sigma)$$

$$(2.26)$$

where σ is a screening constant and is related to the chemical environment of the nucleus. In those circumstances the resonance frequency given by the Larmor equation will change accordingly:

$$v = \left(\frac{\gamma}{2\pi}\right) B_0(1 - \sigma)$$

$$(2.27)$$

Typically chemical shift expressed in a dimensionless unit part per million (ppm), which is defined as follows:

$$\delta = \frac{v_s - v_{ref}}{v_{ref}} \times 10^6$$

$$(2.28)$$

where υ_s is the frequency of investigated sample and υ_{ref} is the frequency of the reference compound.

In case of ^1H spectroscopy a widely used reference compound is tetramethylsilane (TMS) and therefore, its chemical shift δ according to the convention is equal to zero. The usage of TMS is restricted to NMR of organic solvents. Because of the absence of TMS in *in-vivo* systems, it cannot be used as an internal reference. In *in-vivo* measurements commonly used as an internal reference are the methyl resonances of N-acetyl aspartate (2.02 ppm) for ^1H MRS of the brain or the phosphocreatine resonance (0 ppm) for ^{31}P MRS of brain and muscle [6]. However, according to the mentioned convention, in proton spectroscopy the reference to TMS is kept, although its signal is not present. This facilitates the comparison between spectra obtained at different MR systems.

2.5   Spin-spin coupling

Nuclei with magnetic moment can influence each other through space or through chemical bounds. The first type of the interactions is the dipolar coupling and the second scalar coupling. In a liquid environment due to the rapid tumbling the dipolar coupling usually average out to zero and no interaction between nuclei remains [6]. In contrast to
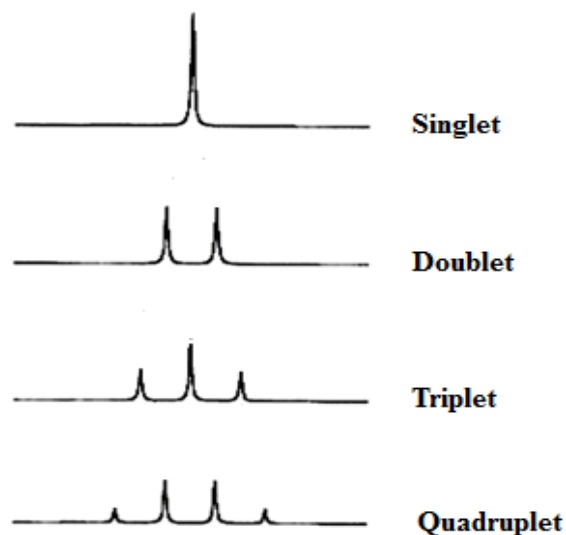

Fig. 2.2. Examples of a splitting pattern [6]

this, the scalar coupling (interactions through chemical bonds) however, remains and results in splitting the resonances into several smaller lines, as seen in fig 2.2. This interaction is called spin-spin coupling or J-coupling and is characterized by a coupling constant J which describes the frequency distance (in Hz) between the splited resonances [6]. The coupling constant J is independent from the external magnetic field.

The underlying principle of the scalar coupling is that in the B_0 field the coupled spins will experience a slight shift of the energy levels. This changes the frequencies of the transition between those energy levels and therefore will split the resonances and the splitting pattern for a magnetically equivalent nuclei (each nuclei in the coupled system must have identical coupling constant) follows the binomial distribution. An example of line splitting is shown in fig. 2.2. Additionally to the line splitting, scalar coupling causes the phase of the coupled resonances to evolve as a function of echo time (TE). For instance, if TE is equal to 1/J the two peaks of a doublet will be inverted in phase and when TE is equal to 2/J those will be visible as a positive signal [15]. An example of metabolite seen in ^{1}H spectra which experiences such a phase evolution is lactate (Lac).

2.6   In-vivo spectroscopy

[1]H possess the highest abundance among all the isotopes that occurs in the biological systems, thus this nucleus is the natural selection for *in-vivo* MRS. Furthermore, water as a container of protons is the most abundant substance in *in-vivo* samples. This however causes that the water signal is strongly dominating over the metabolite resonances and for quantification of the metabolites it needs to be suppressed.

The most straightforward method for water saturation is to use frequency selective suppression pulses which are placed before the main part of the pulse sequence. The frequency spectrum of these pulses is centered on the water signal to provide the frequency selective suppression. Alternatively, the water signal may be suppressed in post-processing and recently several approaches allowing such a suppression of the water signal have been developed [16- 19].
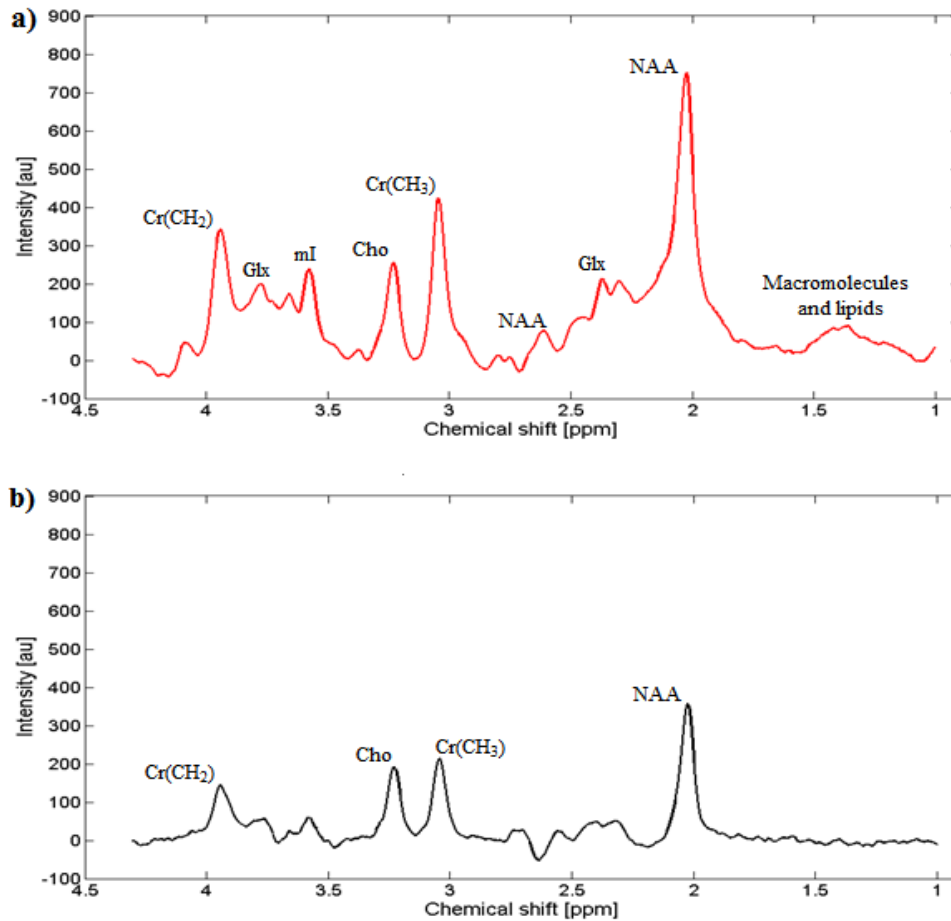
Fig. 2.3: An example of proton spectra acquired from the human brain of a healthy volunteer at TE of 30 ms (a) and 144 ms (b)

As seen on fig 2.3, in proton spectrum it is possible to identify several resonances simultaneously. Each of the resonances are associated with the metabolite (or metabolites) which plays an important role in various biochemical processes within the human brain. The role of those metabolites will be briefly described.

N-Acetyl Aspartate (NAA)

Although this metabolite has several resonances, the most legible occurs at 2.02 ppm. This particular signal has relatively long T_2 decay time, so it is visible in a broad range of TE's (fig. 2.3 b). It is assumed that NAA can only be found in neurons, therefore it is used as a neuronal marker. In many neurodegenerative diseases (i.e. tumors or multiple

sclerosis) a decrease of NAA signal is observed [20-22]. Despite of that the concentration of NAA is not uniform over the entire brain (higher in gray matter compared to white matter) [23], its signal is also used as a concentration marker [6]. Moreover, the signal of NAA can also be used for non-invasive temperature monitoring [24].

Creatine/Phosphocreatine (Cr)

It can be seen (fig 2.3) that this metabolite has two main resonances: at 3.03 ppm and at 3.93 ppm. The first resonance is associated with the protons in CH_3 group while the second with protons in CH_2 group. Both peaks are produced by the overlapped resonances of creatine and phosphocreatine. The difference in ppm between those two signals is practically indistinguishable thus, those peaks are referred as total creatine (tCr). Phosphocreatine serves as an energy buffer (providing the constant levels of ATP) and as an energy shuttle (diffusing from energy producing to energy utilizing sites: mitochondria and myofibrilles respectively) [6]. In the brain both creatine and phosphocreatine compounds are present in neuronal and glial cells.

Choline (Cho)

Choline is the third largest resonance observed in *in-vivo* spectra (fig. 2.3). The main peak can be seen as a singlet at 3.22 ppm. Other choline signals (3.54 and 4.05 ppm) due to their small intensity and overlapping with the other resonances are practically invisible. The main choline signal is composed from a number of overlapping resonances, thus it is referred as choline-containing compounds or total choline (tCho). Choline-containing compounds are involved in phospholipid synthesis and degradation therefore, they are mostly associated with the cell membrane.

Glutamine and Glutamate (Glx)

Glutamine and glutamate are entirely composed from J-coupled resonances, therefore their observation is difficult and strongly dependent from TE used in measurements (for long TE those signals are almost invisible). The combined signals of glutamine and glutamate can be seen between 2.1 to 2.6 ppm and between 3.6 to 3.9 ppm

and are overlapped with the other resonances (NAA, tCr or mI). Glutamate is associated with the excitatory neurotransmission and can be found in all brain cells [6]. Both compounds are involved in ammonia detoxification, which normally occurs in the liver. In the case of liver dysfunction this process is performed in the brain and this result in decrease of glutamate and increase of glutamine signals [25].

Inositol (mI)

In proton MRS it is possible to detect two isomers of inositol: myo- and scyllo-inosotol. Resonances of myo-inositol (mI) can be seen at 3.28, 3.54, 3.60 and 4.05 ppm, however the most prominent signal is at 3.54 ppm [6], while the signal of scyllo-inositol occurs at 3.35 ppm. It is assumed that mI plays an important role in intracellular signaling pathways [26] and can be noticeably reduced in several diseases [27, 28]. In healthy brain scyllo-inositol is not visible, however in some pathologies it can be highly elevated [29].

Lactate (Lac)

Lactate or lactic acid has two main groups of signals: a doublet at 1.33 ppm and a quadruplet 4.11 ppm. In *in-vivo* spectra the second signal of lactate is often partially suppressed by water saturation pulses. Lactate is a marker of tissue ischemia and hypoxia [30, 31]. Its signal rises quite rapidly even for a short periods of oxygen deficiency. Detection of lactate resonances can be complicated, since its resonances are J-coupled and at short echo times are overlapped with lipids and macromolecules. Under normal conditions (in a healthy brain tissue) lactate signal is not visible however, in some disorders [21, 30, 32] it can be highly elevated.

Macromolecules and lipids

Those signals are usually visible at short TE ($\sim$ 30 ms) spectra as a number of overlapped, broad resonances between 1 and 2 ppm. In MRS of the brain most of those signals are coming from unwanted resonances of the extracranial lipids. However, in some diseases variations in the concentration of lipids and macromolecules can provide additional information. Since the free fatty acids are associated with the cell membranes,

the increased lipid signal may be an evidence for the cell membrane damage, which can occur in the certain type of tumors and during ischemia [33]. As for macromolecules, their concentration may be elevated in tumors and during stroke [34 -36]. Moreover it has been shown previously, that their distribution within the brain is regionally dependent [37].

2.7   Single voxel measurements (Single Voxel Spectroscopy)

In *in-vivo* MRS, the dimensions of an area under investigation are much larger compared to the *in-vitro* samples and it often contain different tissues that possess slightly different magnetic properties. This spatial heterogeneity of the tissue increases the B_0 and B_1 field inhomogeneities. As a consequence, unlocalized spectrum will have broad resonances and might be contaminated by some unwanted signals (i.e. water and extracranial lipids). Since localized spectra are measured from a much smaller volume, the field homogeneity is better and the contamination by signals from other spatial positions (partial volume effect) is much lesser. Therefore, the usage of localization techniques improves spectral and spatial resolution. In ^{1}H MRS the volume selection is mostly based upon the usage of the B_0 field gradients accompanied by the RF pulse. The most widely
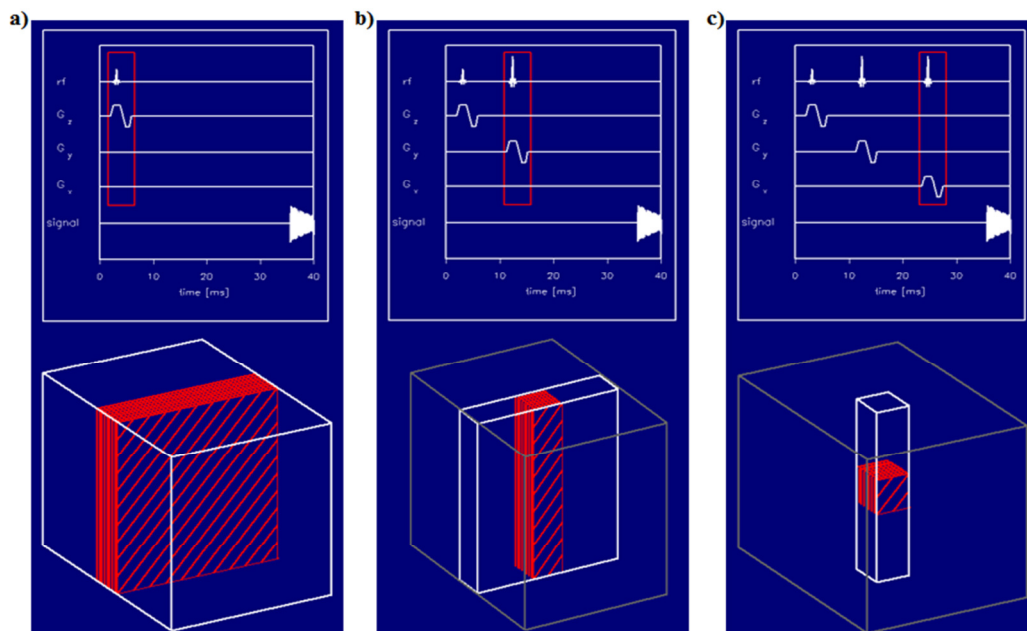

Fig. 2.4: Volume selection with Point Resolved Spectroscopy (PRESS) sequence (a-c) [38].

used localization techniques are stimulated acquisition mode (STEAM) and point resolved spectroscopy (PRESS).

Volume selection

Fig. 2.4 demonstrates the volume selection in the case of single voxel measurement. Since for both PRESS and STEAM sequences the principle of volume selection is very similar, the first sequence was used as an example. It can be seen that, the first RF pulse with the first gradient is responsible for slice selection (2.4 a), the second pulse together with the second gradient excites the entire bar (2.4 b) and finally the last RF pulse accompanied with the last field gradient choses the volume element (2.4 c). The excited volume element is situated at the cross-section of the three orthogonal planes successively chosen by each RF pulse.

Stimulated Echo Acquisition Mode (STEAM)

STEAM is a technique capable to perform a 3D localization in a single acquisition, therefore it is described as a single shot method. The diagram describing this sequence is shown on fig. 2.5. The main part of the sequence consists of three 90° excitation RF pulses accompanied with the gradients in x, y and z directions respectively. As described by Hahn in 1950 [39], a group of three excitation pulses will produce three FID's (formed after each excitation pulse) and five echoes. Four of those echoes are produced at different time points between the RF pulses (three spin echoes are formed by each pair of RF pulses while the double spin echo occurs after all three pulses) and the last echo (so-called stimulated echo) is produced at the end of the sequence. The position of the stimulated echo depends on the timing parameters of the sequence: echo time (TE) and mixing time (TM). As seen on fig. 2.5, TE refers to the sum of the time intervals between the first and second 90° RF pulse and between the last 90° RF pulse and the final echo, while TM denotes time interval between the second and third RF pulse.

In MRS the main signal of interest is the stimulated echo, which raises at the end of STEAM sequence. This is because the stimulated echo signal is affected by transverse relaxation within both TE/2 periods, while during the TM period this signal is affected by

longitudinal relaxation only. Therefore, with STEAM measurements with shorter TE are possible.

The other echoes produced by the sequence have to be eliminated. This is achieved by additional B_0 gradients (crusher gradients). The crusher gradient placed in the TM interval (fig. 2.5, dark gray) is destroying all the components which are not affected by the longitudinal relaxation. It also dephases all the signals except the FID produced by the last excitation pulse. This signal is eliminated by an additional crusher gradients placed within both TE/2 intervals (fig. 2.5, light gray).
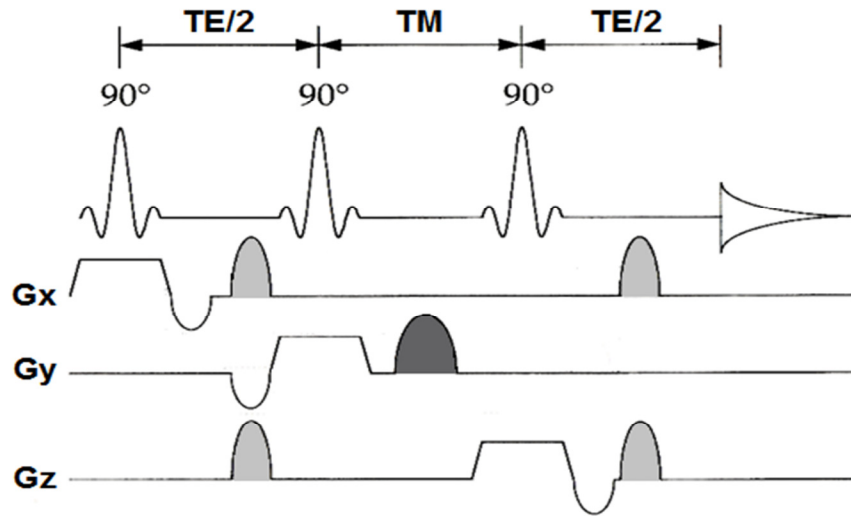

Fig. 2.5: STEAM sequence for 3D single voxel measurements. Crusher gradients used for dephasing the unwanted signals produced by RF pulses are marked with gray color [6].

In the STEAM sequence the final signal is reduced for approximately 50% [40] compared to the PRESS. This is because the second 90° pulse only rotates the half of transversal magnetization to the longitudinal axis, while the rest is dephased by a crusher gradient within the TM period [6].

Point Resolved Spectroscopy (PRESS)

The PRESS sequence is also a single shot technique. It was developed from a depth-resolved surface coil spectroscopy (DRESS) sequence [41, 42] by adding two refocusing
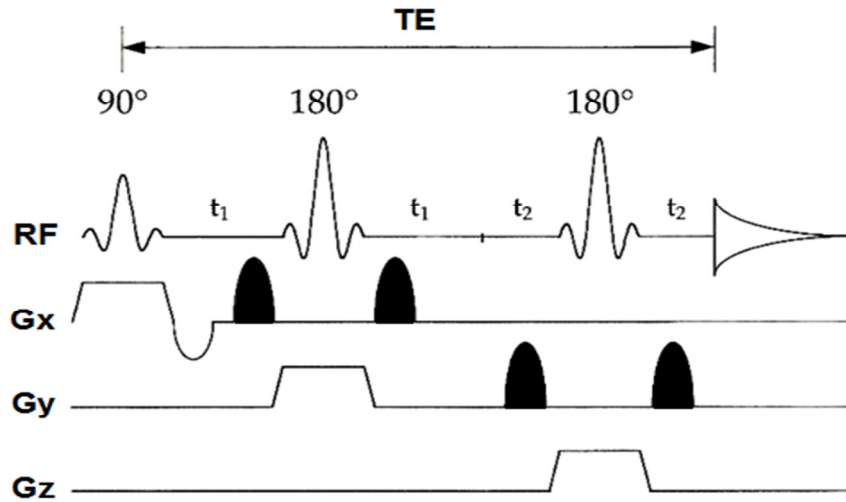
Fig. 2.6: PRESS pulse sequence for 3D single voxel measurements. Crusher gradients (black) surrounding the refocusing pulses are used for destroying the unwanted coherences produced during volume selection [6].

pulses to the excitation pulse. A sequence diagram for PRESS is shown on fig. 2.6. Signal produced by this sequence is a double spin-echo. The first echo is produced after the first 180° refocusing pulse and arises within the time period of $2t_1$. The second 180° pulse refocuses the spin-echo during a time period of $2t_2$, so the final signal is formed at time $2t_1 + 2t_2$, which is equal to TE. The first echo contains the signal from the spins located inside the column, which is formed by an intersection of two planes excited by 90° and first 180° RF pulses. The second spin-echo only contains the signal from the excited volume element which is determined by an intersection of all the planes selected by all the RF pulses.

In the PRESS sequence any deviation from the nominal flip angle value of two refocusing pulses will give a rise of the unwanted transverse magnetization, which have to be destroyed by additional crusher gradients placed around both 180° pulses (fig. 2.6, black color). A short comparison of both STEAM and PRESS sequences in presented in tab. 2.1:

Tab. 2.1 A comparison of main features of PRESS and STEAM pulse sequences

Sequence	PRESS	STEAM
Type of RF pulses	90°, 180°, 180°	90°, 90°, 90°
Type of the signal	Spin echo	Stimulated echo
Signal	100% of signal	50% of signal, due to losses in transverse magnetization
Sensitivity for motion artifacts	lower	higher
Echo times	Minimal TE is longer	Minimal TE can be shorter

2.8 Multiple voxel measurements (Spectroscopic Imaging)

The principles of volume selection in spectroscopic imaging are the same as for single voxel measurements. Since in MRSI signals from different spatial locations are detected simultaneously, it is necessary to add an additional phase encoding to PRESS or STEAM pulse sequence. This is achieved by additional gradients, which can be placed along any physical direction.

In the case of PRESS sequence, phase encoding gradients can be placed between the 90° excitation pulse and the first 180° refocusing pulse. The strength of this phase encoding gradient (or gradients) is incremented in subsequent acquisitions. In consequence, in each phase encoding step the precession frequencies of the spins are modified to include the spatial dependency. This is equivalent to a spatially dependent phase shift [6]. As a result, spatial localization of each voxel is encoded in phase. During each phase encoding step a spectrum from different localization is measured. The number and direction of those phase encodings depend on the number of physical dimensions explored by such a sequence.

Spatial encoding can be also described by using the concept of k-space. The k-space can be defined as a Cartesian grid where each single point corresponds to a single complex vector which describes the FID with specific phase encoding gradients. The position of a

single k-space point is described by the actual amplitude of the phase encoding gradients. During each phase encoding step a single k-space point is sampled. Spatially encoded spectral information can be therefore obtained by measuring each single point of the k-space [43].

In MRSI the spatial position of the measured signal does not exactly correspond to the rectangular shape of the voxel and after Fourier transformation it turns out that the signal from the particular voxel is contaminated with the signal from the other voxels [43]. This effect is described by the point spread function (PSF) which gives the information
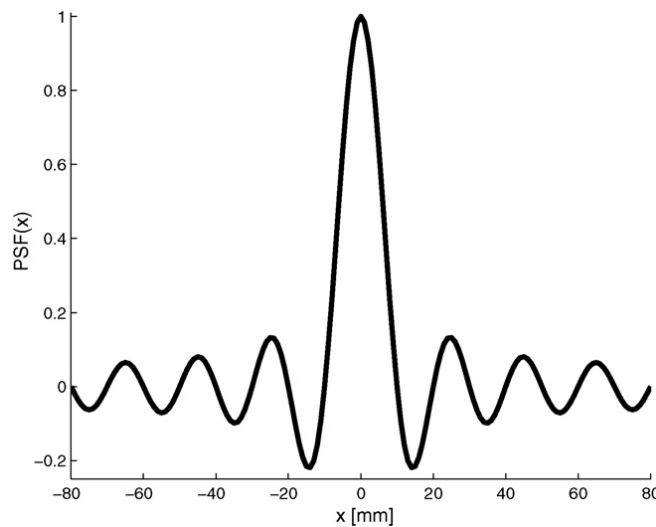

Fig. 2.7: Point spread function for 1D SI with 16 phase-encoding steps and field of view= 160 mm. The function shows how neighboring voxels contribute to the voxel positioned in the center of the PSF [43].

about the contribution of the neighboring voxels to the signal from particular voxel [43]. An example of PSF is depicted in fig. 2.7. The shape of PSF is strongly dependent from the number of phase encoding steps and the k-space sampling method used. A decreasing number of phase encodings causes broadening of the main lobe and of PSF while the side lobes become higher. It has been demonstrated, that for more than 64 phase encoding steps the PSF may have a minor influence [43]. However such a high number of steps strongly prolongs the measurement time thus, in *in-vivo* measurements typically 8-16 phase encoding steps in each direction are used [43].
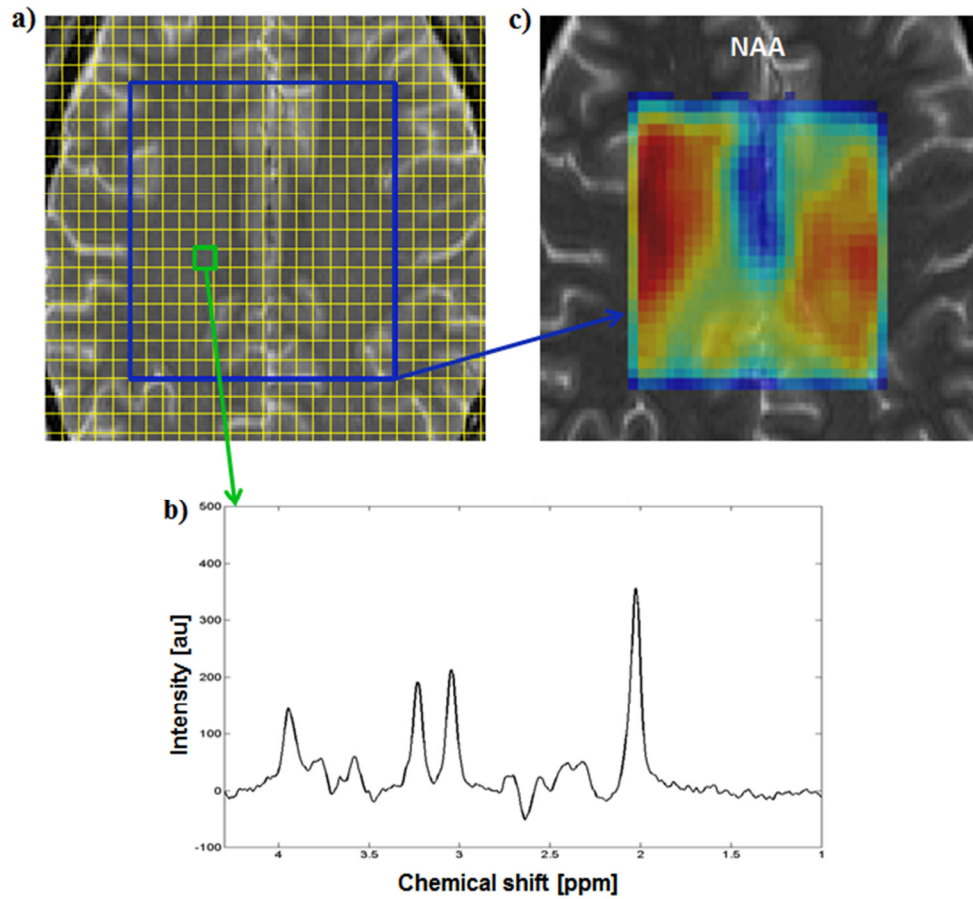
Fig. 2.8: An example of CSI acquisition in the human brain. The VOI excited by the pulse sequence (a- blue square) is subdivided in to voxels (a- green square). Each single voxel is represented by a spectrum (b). The so called metabolite map (c- here for NAA) depicts the spatial distribution of metabolites over the VOI.

An example of CSI acquisition is shown on fig. 2.8. Since in spectroscopic imaging the volume excited by the sequence (VOI, blue square) is subdivided into voxels and each voxel is represented by a single spectrum (2.8b), it is possible to calculate a spatial distribution of the metabolites (2.8c) seen in a single spectrum.

Spatial resolution of CSI can be either 1D, 2D or 3D. However, in case of 3D measurements the total acquisition time can be significantly prolonged, therefore not very feasible for clinical applications. Commonly a 2D acquisition is used, in which spectra are acquired from a single slice. On the other hand, there are several ways to reduce the

measurement time. One can distinguish the following: reduced k-space sampling, multi-echo MRSI or the so-called high-speed MRSI [6].

Reduced k-space sampling

This is one of the most straightforward methods allowing reducing total acquisition time. It consists on the fact that high spatial frequencies, which are located at the borders of the k-space, are having minimal contribution to the measured signal. Thus those need not to be sampled and may be zero-filled [44]. This results in a circular pattern of k-space sampling scheme. The radius of this circular region is the main factor, which decides about the reduction of the total acquisition time. Moreover, sampling the k-space in a circular fashion results in a more favorable point spread function [6]. This k-space sampling scheme can be modified in order to improve the distribution of point spread function to the so-called sparse k-space sampling. This scheme omits some specific k-space points, while the others are sampled twice. With the sparse k-space sampling it is possible to achieve a more optimal shape of the point spread function [6].

Unfortunately, reduction of the k-space sampling may enlarge the effective voxel size. This increases the signal overlap between the adjacent voxels and gives a rise in partial volume effects [45].

Multi-echo MRSI

Usually in MRS T_2 time is much longer than T_2^*, therefore during a single TR period it is possible to acquire more than one echo. Each single echo can be separately phase encoded and a reduction of the total acquisition time depends on the number of echoes [46]. With this technique even a threefold reduction of the measurement time can be achieved [46]. The presented approach is however limited to the metabolites with long T_2 relaxation time. An additional difficulty is to choose an optimal number of echoes. This depends on the ratio between T_2^* and T_2 and therefore on the B_0 field homogeneity [46]. Moreover, reduced echo sampling times causes the spectral resolution to be degraded which results in increased overlapping between the metabolite signals (especially between

41

tCho and tCr resonances) [46]. Finally, this technique is more sensitive to lipid contamination as reduced echo duration will lead to broadening of the spectral PSF [46].

An alternative approach is to uniformly encode several echoes. This will not reduce the measurement time, but will increase an amount of information obtained from a single SI experiment by a simultaneous acquisition of spectra at different TEs [47]. Hence, it is possible to optimize the individual metabolite signals including T_2 relaxation time or J-coupling effects [47]. This approach is however again more sensitive for lipid signals (especially for spectra acquired with short TE) and does not offer any time gain.

High-speed MRSI

In most of the fast MRSI techniques a time gain is achieved mainly by an application of more efficient k-space sampling schemes. Additionally some of those sequences uses magnetic field gradients during signal acquisition [6]. All together allows acquiring a complete 2D or 3D data sets in the time which is not achievable by conventional SI. High-speed SI sequences do not improve the signal-to-noise ratio or the sensitivity, but provide a more flexible tradeoff between the sensitivity and the minimal measurement time [6].

Recent development in the field of high-speed MRSI techniques resulted in a number of different approaches. Moreover a certain amount of them is based on a combination of several techniques in to one sequence. Such an example is the sequence proposed by Dreher et. al [48], which combines spectroscopic missing pulse steady-state free precession (spMP-SSFP) with echo planar spectroscopic imaging (EPSI).

2.9   MRS without water suppression pulses

As mentioned previously most of proton spectra are acquired with water suppression pulses. This is due to the dominating water signal which can be from 2 to 5 orders of magnitude higher than metabolite resonances (fig. 2.9) and is usually suppressed with frequency selective pulses to enable correct quantification of metabolite resonances.

This technique is the most straightforward one and therefore the water suppressing pulses are an integral part of usual MRS sequences. However, when the frequency of the water signal is shifted (B_0 field inhomogeneities), water suppressing pulses may suppress water signal only partially. This insufficient water suppression results in a complicated shape of the baseline and seriously hampers the quantification. Moreover, water suppressing pulses may interfere with the metabolite peaks, due to magnetization transfer effects [18, 49]. Non-water suppressed MRS not only avoids these problems but additionally offers the unsuppressed water signal which can be used as an internal reference for quantification or for baseline and phase correction.
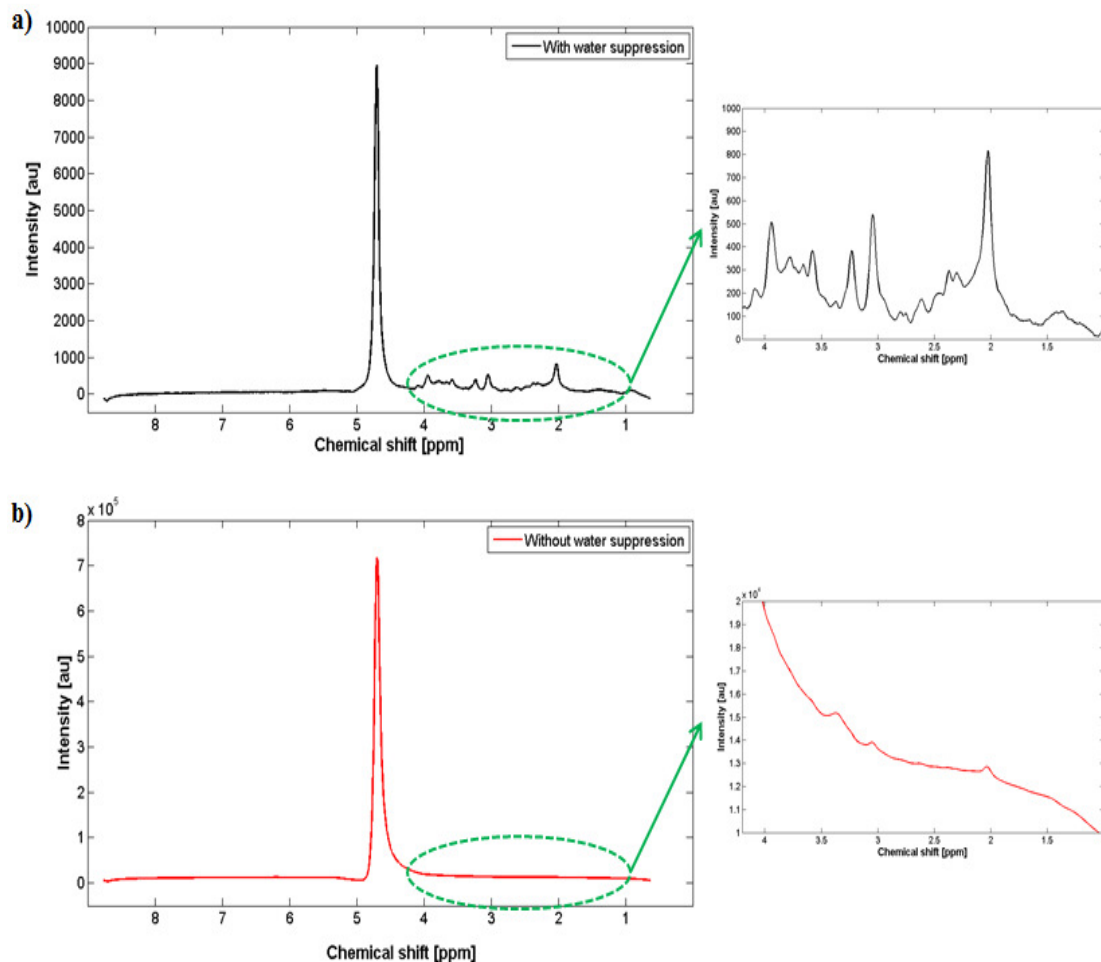

Fig. 2.9: An example of spectra acquired at TE of 30 ms with weak water suppression (a) and without water suppression (b). For better visualization of metabolite resonances the up-field region of the spectra was magnified.

Progress in non-water suppressed MRS was induced by the development of 16 and 32 bit ADC. This provided sufficient dynamic range to simultaneous sample the water and metabolite signals. Nevertheless, as seen in fig. 2.9b because of the overlap between the tail of the water signal and the metabolite resonances, the water signal still has to be reduced. This can be done in postprocessing and several strategies which enable water signal reduction has been established so far. Those employs different algorithms, such as low pass filtering with Gaussian convolution and subsequent subtraction of this filtered signal from the original FID [16], fitting with the FID signal with a combination of monoexponential functions and then subtraction of this fitted signal from the measured FID [17] or methods based on decomposition (SVS and MPM) [12, 18, 19].

Different methods of water signal reduction are more extensively described in the introduction to chapter 4.

2.10 Sideband artifacts

The common problem of spectra acquired without water suppression is the presence of sideband artifacts. It is assumed that sidebands originate from the mechanical vibrations of the gradient coils which lead to sinusoidal perturbations of B_0 field [11, 50]. This results in spurious peaks centered around NMR major signals like water or lipids [49, 51]. As the sidebands are related to the gradient coils, one may expect that due to the differences in construction of the hardware elements (gradient coils) different MR systems will show different sideband patterns.

As seen in fig. 2.10, water signal related sidebands occur in pairs which are having opposite phase and are equidistant from the water peak. The intensity of those spurious peaks depends not only from the echo time but also from the strength of the gradients and position of the MRS voxel regarding to the magnet's isocenter [11]. It can also be seen (fig. 2.10) that sideband peaks occur in almost the entire spectral range. Therefore, in non-water suppressed spectrum they will be overlapped with almost all the metabolite resonances. As a consequence, spurious peaks of the sidebands have to be reduced before quantification.
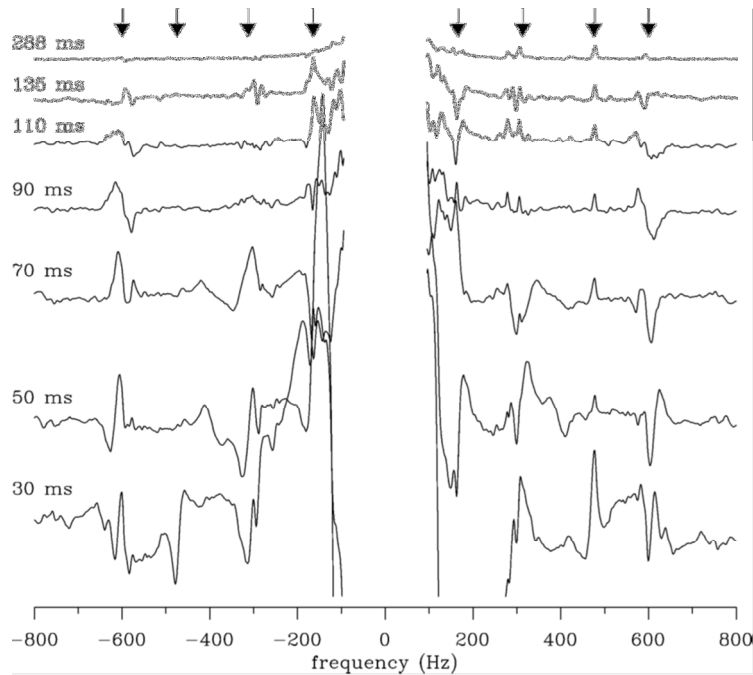
Fig. 2.10: PRESS acquisitions at various TE values from a single-voxel in the head phantom. Locations of prominent sidebands are indicated by the arrows. TE values are given at the left of each spectrum [11].

There are several techniques for reduction of the sideband artifacts. Those can be subdivided in to software- and hardware-based methods. The first category utilizes different software techniques such as: decomposition of the sidebands with Hankel-Lanczos singular value decomposition (HLSVD) [52], reconstruction of the real part of the spectrum from the modulus signal [53] or subtraction of the water phantom sideband pattern from the measured spectra [54]. The second category is based on modification of the pulse sequence or the hardware (MR scanner) used for measurements. Here, one can distinguish the following approaches: direct compensation of the B_0 field perturbations which lead to sidebands [50], oversampling and TE averaging of the acquired data [55] and different combinations of phase cycling and acquisition with alternating gradients [12].

More comprehensive description of the sideband artifacts has been given in the introduction to chapter 3. A detailed description of different techniques for sideband artifact reduction has been presented in the introduction to chapter 4.

Chapter 3:

Evaluation of Gradient Induced Sidebands for the Purposes of Proton Chemical Shift Imaging without Solvent Suppression

3.1 Introduction

The vast majority of in-vivo proton (1H) spectra are acquired with frequency-selective water suppression. This strategy guarantees that the metabolite resonances will not be superimposed by the tail of the water signal and, thus, will be accurately resolved for further quantification. However, within the past decade, several research groups have demonstrated that 1H magnetic resonance spectroscopy (MRS) and 1H magnetic resonance spectroscopic imaging (MRSI) are also feasible without water suppression [1 -10]. The major problem in unsuppressed 1H spectra is the presence of the so-called sideband artifacts, which manifest as frequency modulations related to the dominating water signal [2 -3].

Previous studies have indicated that the presence of the sidebands in unsuppressed spectra is associated with the gradient coil vibrations similar to that of the acoustic noise [3 -4, 11 -13]. These lead to sinusoidal perturbations of the B0 field and result in spurious peaks placed symmetrically around the NMR resonances [3, 8]. Typically, the sidebands are only a small part of the NMR resonances (in order of ppm) [8, 12], and therefore, they are only observable for the large signals such as water [3] and lipids [14]. In non-suppressed 1H MRS/I, the sidebands appear in pairs equidistant from the water resonance. Additionally, the up-field sideband is almost 180° out of phase, when compared with its down-field equivalent [3].

It has been shown that the amplitude of the sidebands depends on the echo time (TE), strength of the crusher gradients and spatial position [3, 8]. The amplitudes of the sidebands decrease with increase in the TE [3]. Moreover, the amplitude of the sidebands increases with the distance from the magnet's isocenter and the strength of the gradients [3, 8].

Recently, several solutions to the sideband problem have been demonstrated [2 -10, 15 -16]. These can be subdivided into two main categories: software- and hardware-based. The first category incorporates methods that are based on acquisition of spectra with unmodified pulse sequence and then reduction of the sidebands in the postprocessing. Different approaches for sideband reduction are used: Hankel-Lanczos Singular Value Decomposition (HLSVD) [15], reconstructing the real part of signal from the modulus of

the FID [5 -6] and the usage of the water phantom sideband pattern for reduction of the sidebands in in-vivo measurements [9, 16]. Hardware-based methods mainly consist of modification of the pulse sequence or the MR scanner used for data acquisition. The reduction of the sidebands may be achieved by the usage of phase cycling combined with positive and negative amplitude of the gradients [13], inversion of all gradients every second measurement [7], acquisition of the oversampled data [2] or compensation of the B0 field variation that causes sidebands [8].

Another possibility to reduce the sidebands is the optimization of the crusher gradients. Clayton et al. [3] demonstrated that the removal of the second pair of the crushers within a point-resolved spectroscopy sequence (PRESS) enables a significant reduction of the sidebands. However, these particular gradient pulses are necessary for dephasing unwanted signals produced during the volume selection [17 -18]. Therefore, this study focuses on the largest possible reduction of the strength of second pair of the crusher gradient pulses within a PRESS sequence without an increase in those unwanted signals.

As the logical crusher gradient is usually a combination of physical gradients applied in different directions, the aim of this study was to determine which of the physical gradients have the maximum influence on the sideband amplitude and to investigate the potential possibilities of optimization of the crusher gradients in PRESS sequence for the purpose of chemical shift imaging (CSI) without water suppression.

3.2   Material and Methods

CSI measurements were performed with a 60-cm bore 3-Tesla whole body MR scanner (TimTrio, Siemens, Erlangen, Germany) equipped with a gradient system with the following parameters: in x- and y- directions, the maximal amplitude was 40 mT/m, rise-up time was 204 μs, and slew rate was 180 T/m/s; in z-direction, the maximal amplitude was 45 mT/m, rise-up time was 204 μs, and slew rate was 220 T/m/s.

Spectroscopic data were collected with a 12-channel receive-only head coil. A PRESS sequence was used for volume selection. The sequence was modified for enabling the measurements with different strengths of the last pair of the crusher gradients (before

and after the second 180° refocusing pulse). The modifications were done in Numaris4 sequence development environment (Siemens, Erlangen, Germany).

Spherical water phantom measurements

For the sideband assessment, a spherical water phantom with the diameter of 16 cm (1.25 g of $NiSO_4$ aqueous solution per 1000 g of distilled water), provided by the scanner manufacturer (TimTrio, Siemens, Erlangen, Germany), was used. The phantom was placed in the magnet's isocenter, and non-water-suppressed CSI spectra were acquired in the transversal plane. The parameters of the acquisition were as follows: repetition time (TR) 1500 ms; TE 30 ms; field of view (FoV) 160×160 mm^2; excited volume of interest (VOI) 80×80×15 mm^3; voxel size 10×10×15 mm^3; CSI matrix 16×16 voxels; number of averages 3; vector size 512 oversampled to 1024 complex data points; and weighted k-space sampling scheme. With these parameters, the total acquisition time was 6 min and 5 s.

In these measurements, the strength of the crusher gradients was modified for each physical direction separately and was varied from 25 to -25 mT/m with the following steps in between: 15, 11 (default value), 5, -5 and -15 mT/m.

Agar phantom measurements

The influence of the different amplitudes of the crusher gradients on the MRS signal to be spoiled was evaluated by measurements with a homemade agar phantom with the diameter of 16 cm (9 g of NaCl per 1000 g of 2.5 % agar). Air space with the dimensions of 55×55×15 mm^3 was placed in the center of the phantom. Non-water-suppressed CSI was performed in the coronal plane (orientation necessary due to construction of the phantom) with the following parameters: TR 1500 ms; TE 30 ms; FoV 120×120 mm^2; VOI 50×50×7 mm^3; voxel size 7.5×7.5×7 mm^3; CSI matrix 16×16 voxels; number of averages 3; vector size 512 oversampled to 1024 complex data points; and weighted k-space sampling scheme. Excited volume of interest was carefully positioned to cover the air compartment. For comparison, spectra were also acquired from the agar compartment, for which a CSI sequence with the same geometrical parameters and with the unmodified crusher gradients

(all directions, 11 mT/m) was used. The total acquisition time was exactly the same as that for water phantom measurements.

In this case, the strength of the crusher gradients was modified for each physical direction separately. Crusher gradients with the following strengths were examined: 11 (default), 5, 4 and 1 mT/m.

In-vivo measurements

The performance of the CSI-PRESS sequence with different crusher gradient amplitudes was tested *in-vivo*. The CSI data from two healthy volunteers (aged 22 and 27 years, mean age: 24.5±3.5 years) were acquired after written informed consent. The CSI-PRESS sequence was performed in the transversal plane, above the lateral ventricles. Excited VOI was placed parallel to the line between the anterior and posterior commissures (ac-pc line). The details of the acquisition were as follows: TE 30 ms and 144 ms; TR 1500 ms; FoV 160×160 mm^2; VOI: 80×80×15 mm^3; voxel size 10×10×15 mm^3; CSI matrix 16×16 voxels; number of averages 3; vector size of 512 oversampled to 1024 complex data points; and weighted k-space sampling scheme. As stated previously, the acquisition time for single CSI measurement took 6 min and 5 s.

Subsequently, the influence of the crusher gradients on the sidebands was evaluated for all gradient directions simultaneously and for a combination of gradients in *y*- and *z*-directions, without gradient in *x*-direction. In both cases, the strength of the gradients was set to be 11 (default value) and 5 mT/m. The spoiling effects of the applied crusher gradients were compared.

Postprocessing and quantification

The spectra were postprocessed with customized software written in Matlab (2011a MathWorks, Natick, MA, USA). After the acquisition spectra were zero-filled to 8k complex data points. Postprocessing incorporated the following steps: zero filling to 8k complex data points, frequency shift correction (water signal used as a reference), Hann-filtering with time constant of 400 ms, automated zero-order phase correction and baseline correction with a 4th degree polynomial function. In the case of spectra acquired from the

agar phantom frequency shift correction, phase correction and baseline correction were excluded from the postprocessing.

Quantification of the sidebands consisted of the assessment of the maximal value of intensity for each evaluated sideband.

3.3   Results

Fig. 3.1 shows the non-water-suppressed spectra measured for the water phantom for different directions and strengths of the crusher gradients. The spectra presented in Fig. 3.1 were taken from the central voxel of the VOI (marked with square- 3.1a). Evaluated sidebands are marked with the dashed lines. It can be seen that the sideband pattern for each physical gradient direction is different (3.1b, 3.1c, and 3.1d). The strongest artifacts can be seen for the measurements with the gradient in the x-direction (3.1b); thus, the
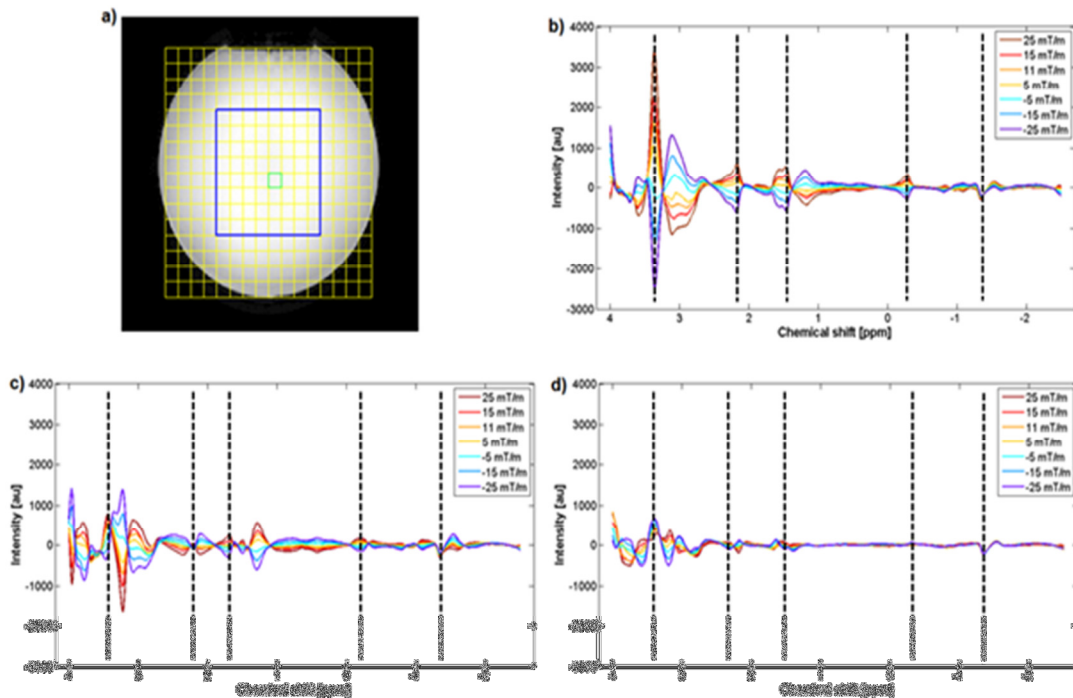

Fig 3.1: Localizer (a) and non-water-suppressed spectra measured for the water phantom (b-d). Measurements were performed for different gradient strengths (from 25 to -25 mT/m) and for different gradient directions (x-direction: b; y-direction: c; and z-direction: d).

spectra acquired with this gradient were used as a reference for determination of the sidebands for further evaluation. In total, five main groups of the sidebands were identified and included in quantification. These were located between 3.5 and 3 ppm, 2.5 and 2 ppm, 2 and 1.3 ppm, 0 and -0.5 ppm and -1 and -1.5 ppm. These sidebands are marked with
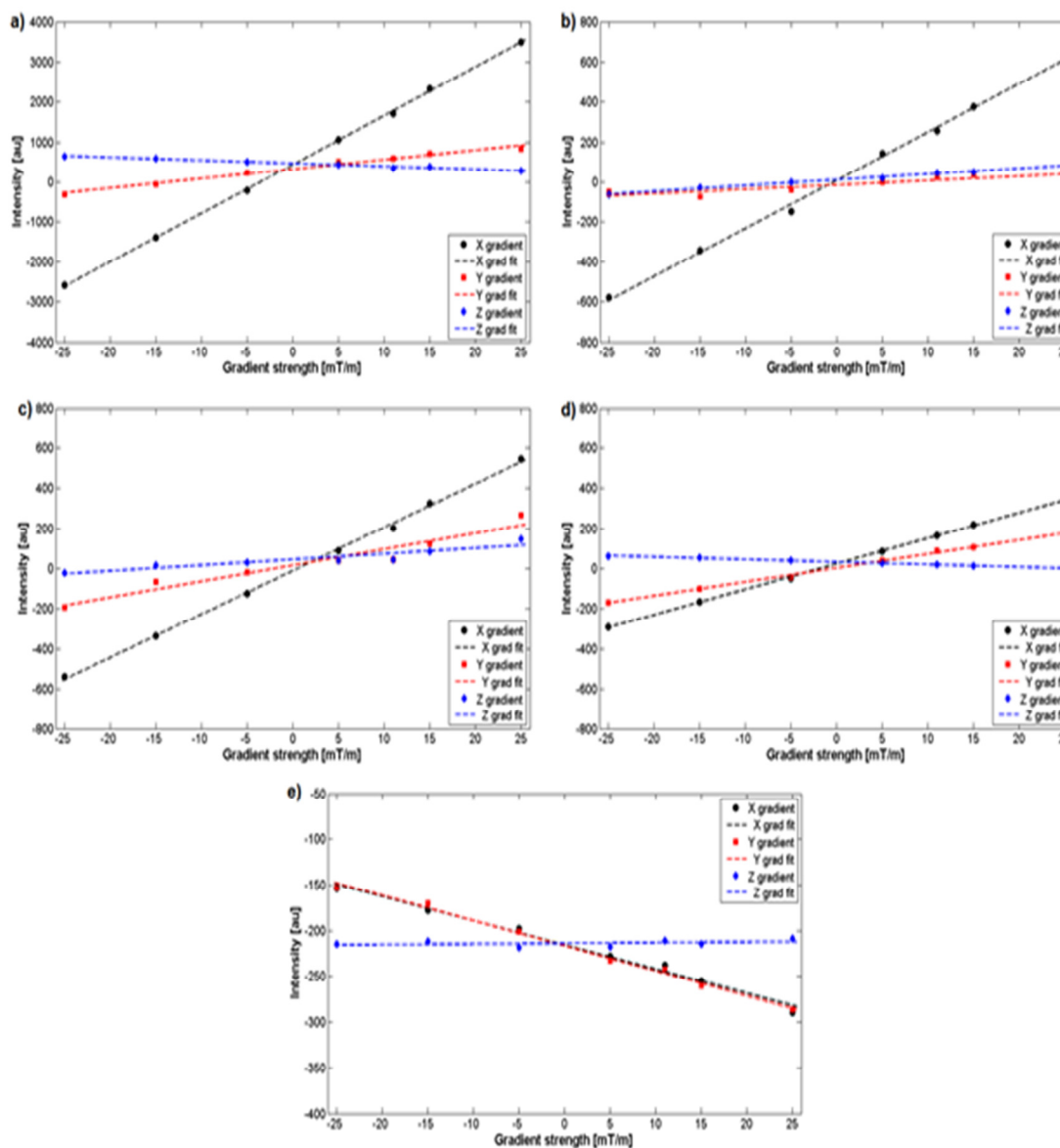

Fig. 3.2: Sidebands' amplitude as a function of crusher gradient strength for all the evaluated artifacts (from the 1st sideband: a; to the 5th sideband: e; respectively). Experimental values are marked with circles (x-gradient direction), squares (y-gradient direction), and diamonds (z-gradient direction) while linear best fit is denoted with the dashed lines.

dashed lines. For the spectra measured with y- (3.1c) and z-gradient (3.1d) the sidebands with similar behavior (positive amplitude for positive gradient strength) and from the corresponding position were chosen for evaluation.

A relationship between the intensity of the chosen sidebands and the strength of the crusher gradients is plotted in Fig. 3.2. As can be seen from the fitting (dashed lines), all artifacts show linear dependency from the gradient pulse strengths. The highest slope of the fitted line can be observed for the x-gradient (black line), and the lowest slope can be seen for the z-gradient (blue line, 3.2a -e). This confirms that the crusher in x-direction has the largest influence on the intensity of the sidebands (exception: 5th sideband; 3.2e), while the z-gradient shows the smallest influence. In most cases, the intensity of the artifacts goes to zero together with the strength of the crushers (3.2a -d). The only exception is the last sideband (3.2e), which seems to be independent of the amplitude of the second pair of the crusher gradients.

Figs. 3.1 and 3.2 show that the sidebands can be reduced by decreasing the strength of the crusher gradients. Subsequently, we investigated how much the gradient strength could be reduced without creating distortions produced during volume selection. This was examined with the agar phantom. Fig. 3.3 presents the spectra acquired from the agar phantom at two different locations: within the agar (3.3a, 3.3c) and within the air compartment (3.3b, 3.3d -f). It can be noted that in the spectra collected from the air compartment, a remaining water signal (3.3d -f) is still present. However, the intensity of this signal is approximately two orders of magnitude smaller than that of the water peak within the agar compartment (3.3c). From the measurements at different gradient strengths (3.3d -f), it can be seen that the increase in the contaminations produced during the volume selection is not noticeable for the strength of the gradients down to 5 mT/m (red line). Below this value, a slight increase in the amplitude and linewidth of the remaining water signal for the x- and z-direction can be observed. The most significant increase in the unwanted signals was noticed for the y-gradient (3.3e).

From the previous results, it appears that the reduction in the crusher gradient strength from 11 to 5 mT/m should not cause an increase in the contaminations produced during volume selection (Fig. 3.3). The sidebands should be significantly reduced in this

case, according to Figs. 3.1 and 3.2. This finding has been verified with in-vivo measurements, and the results are presented in Fig. 3.4. It can be seen that the major influence of the sidebands occurs between 3 and 4 ppm, and the resonances of choline (Cho), creatine (Cr1, Cr2), and myoinositol (mI) seem to be mostly affected, while the region of glutamine (Gln), glutamate (Glu), and N-Acetyl-aspartate resonances (from 2 to 3 ppm) appears to be almost unhampered (3.4b). As the strongest artifacts seem to be associated with the x-gradient (Fig. 3.1), further minimization of the sidebands could be achieved by the measurements performed with the y- and z-gradients only (3.4c). It can be
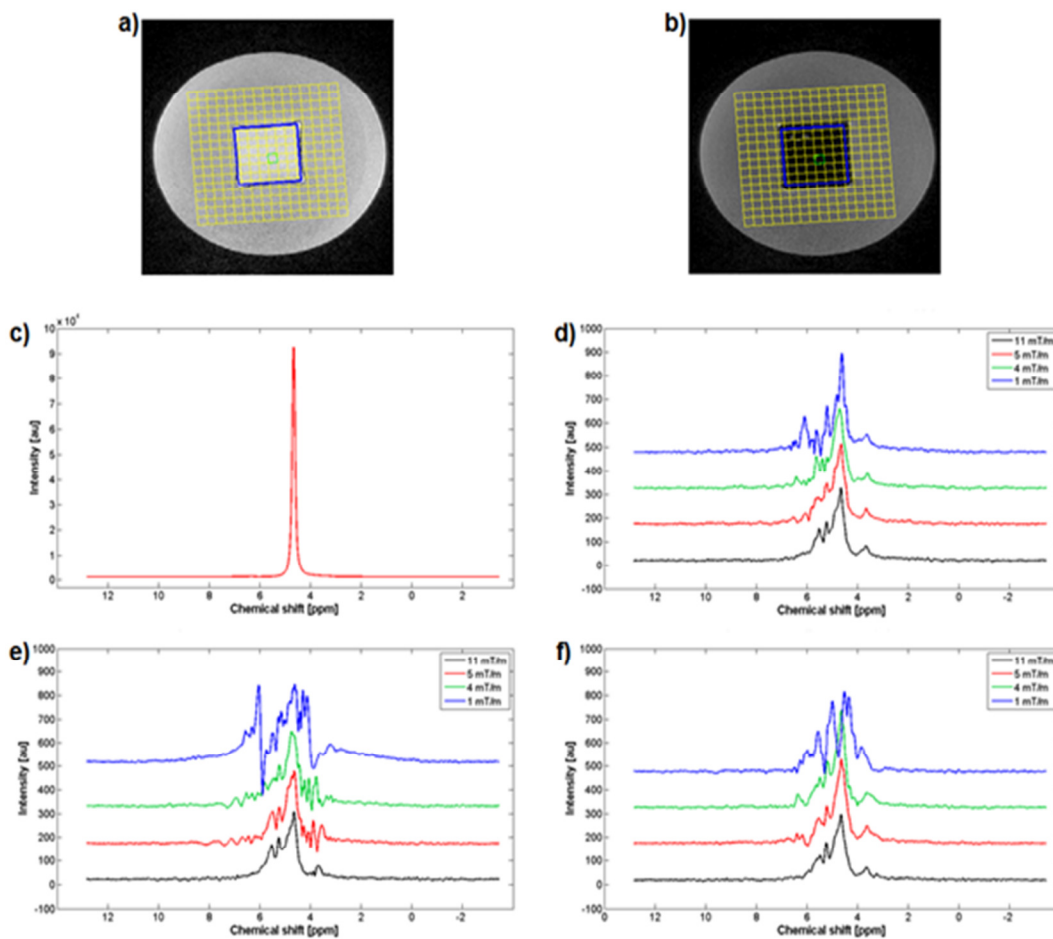
Fig. 3.3: Localizers at the reference area (a) within the air compartment (b) and non-water-suppressed spectra from the agar phantom acquired with different strengths of the gradients (11, 5, 4, and 1 mT/m) at the reference area (c), and from the air compartment for each direction of the gradient separately (x-direction: d; y-direction: e; and z-direction: f). Presented spectra (c -f) originate from the position indicated by the green marker seen on the localizers (a -b).

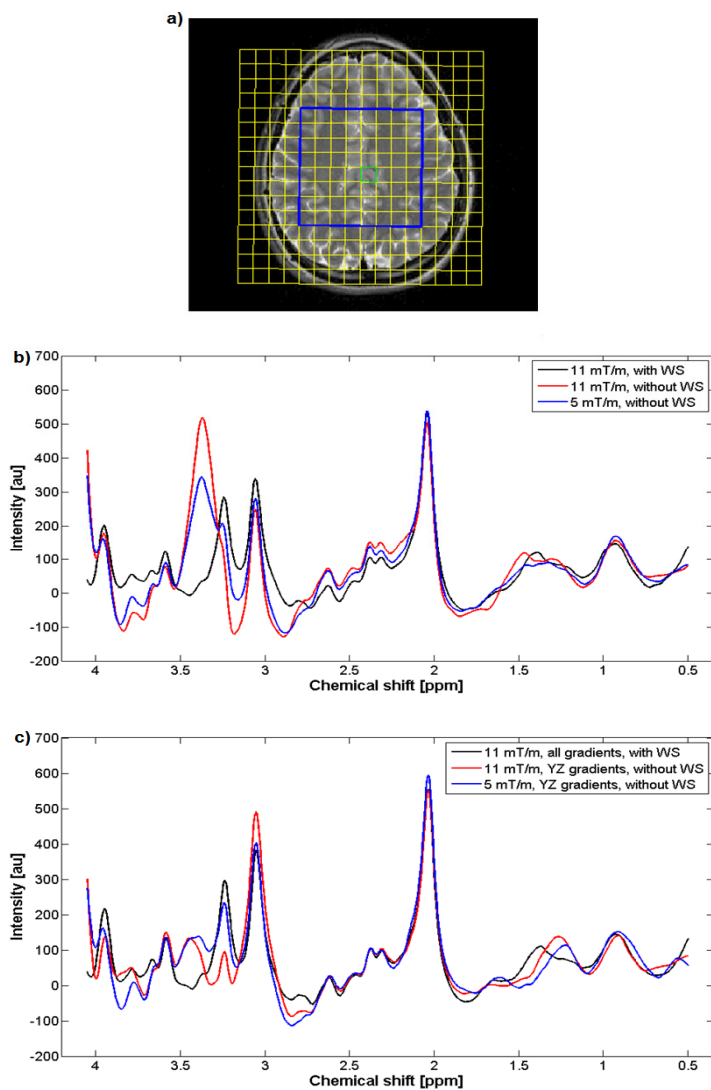*Fig. 3.4: Localizer (a) and in-vivo spectra (b -c) collected at short TE (30 ms) with different strengths of the crusher gradients. In vivo spectra obtained without water suppression at different strengths of the gradients (red and blue, without WS) were compared with the spectrum collected with water suppression and with all gradients at 11 mT/m (black, with WS).*

seen that the region of Glx, Gln and NAA is again almost unhampered; however, the sideband overlapping the Cho resonance is reduced. Moreover, it can be noted that the Cho signal in the spectrum measured with y- and z-gradients at 5 mT/m (3.4c, blue) is now comparable with the signal in the reference spectrum (black).

3.4   Discussion and conclusions

The aim of this study was to investigate the influence of the second pair of the crusher gradients on the generation of the sideband artifacts seen in CSI-PRESS sequence without water suppression.

It was shown that for the used magnet and gradient systems (Tim Trio, Siemens, Erlangen, Germany), each physical direction of the crusher gradient creates unique pattern of sidebands (Fig. 3.1). The highest intensities were observed for the crusher in x-direction, while the smallest were noted for the crusher in z-direction. This is confirmed in Fig. 3.2, where the highest slope of dependency between the strength of the gradients and intensity of the sidebands is visible for the x-direction. These results are in contrast to those described by Nixon et al. [8], who reported that the sidebands generated by different directions of the gradients were similar. In this study, however, a LASER excitation scheme and a 4 T Magnex magnet with Magnex (Magnex Scientific Ltd, Oxford, UK) gradient system have been used. As the occurrence of the sidebands is related to the mechanical vibration of the gradient coils [3] and its pattern may be associated with the excitation scheme [8], those dissimilarities can be explained by the differences in the localization scheme and the dissimilarities in the construction of the magnet and gradient systems.

Previous studies [3, 8] have reported a linear dependence between the sidebands' intensity and the strength of the crusher gradients. In our study, this dependence has been confirmed for almost all the evaluated sidebands (Figs. 3.1 and 3.2). The only exception seems to be the last artifact (between -1 and -1.5 ppm), where the dependence between the crusher strength and intensity is linear, but the intensity of this artifact does not converge to zero with the strength of the gradient pulses. Thus, this particular artifact could be possibly related to the first pair of the crusher gradients (between the first 180° refocusing pulse) or to the spoiler gradients.

For all the measurements, a weighted k-space sampling scheme was used. This reduced the amount of acquired k-space data to approximately 30% and increased the effective size of the CSI voxel [19] as well as the partial volume effect. This may explain the presence of the remaining water signal in the spectra measured within the air space of the agar phantom.

However, the water signal in those spectra is approximately two orders of magnitude smaller than the signal in spectra measured within the agar compartment, and, therefore, this effect could be neglected.

In-vivo measurements at short TE revealed that for the gradient system used, the sidebands mostly affected the resonances of Cr2, mI, Cho, and Cr1, while the peaks of Gln, Glu, and NAA seemed to be almost undisturbed. It has been demonstrated that decrease in the gradient strength from 11 to 5 mT/m reduces the sidebands by approximately 30%. On the other hand, such a reduction in the crusher's strength does not introduce additional disturbances from the unwanted signal produced during volume selection. For the gradient strength below 5 mT/m, a slight increase in the amplitude and width of the remaining water signal (especially for the crusher in y-direction, Fig. 3.3) could be observed. As the crusher in x-direction generated the strongest sidebands, further decrease in those could be achieved with the removal of this particular gradient. This is valid especially for the group between 3.5 and 3 ppm, where a large sideband overlapping the Cho signal was strongly reduced (Fig. 3.4c).

In this study, dependence between the sideband's intensity and the position of the voxel with regard to the magnet's isocenter has not been evaluated. This is because the CSI-PRESS sequence is prone to magnetic-field inhomogeneities and excitation profile, which could influence the results. In addition, all the spectra presented in this study have been taken from the voxel in the central part of the VOI.

We demonstrated that in our magnet and gradient systems (Tim Trio Siemens, Erlangen Germany), each gradient direction produces a unique pattern of the sideband artifacts. Moreover, it was possible to minimize the influence of those on non-water-suppressed spectra by decreasing the strength of the crusher gradients. A decrease in the strength of the crusher from 11 to 5 mT/m resulted in a reduction of those artifacts without causing an increase in the unwanted coherences produced during volume selection. However, this is valid for our MR system, and one may expect that as the pattern of the sidebands for different MR systems may be different, such a decrease of the gradient strength may be difficult to achieve. Nevertheless, with such a reduction of the sidebands in short TE non-water-suppressed spectra, it could be possible to reduce them further in

postprocessing, instead of using special acquisition strategies [7 -8] which may be time consuming or may require additional hardware modifications.

3.5 Acknowledgments

3.6 References

1. Van der Veen J, Weinberger DR, Tedeschi G, Frank JA, Duyn JH. Proton MR spectroscopic imaging without water suppression. Radiology 2000;217:296–300.

2. Hurd RE, Gurr D, Sailasuta N. Proton spectroscopy without water suppression: the oversampled J-resolved experiment. Magn Reson Med 1998;40:343-347.

3. Clayton DB, Elliott MA, Leigh JS, Lenkinski RE. 1H spectroscopy without solvent suppression: characterization of signal modulations at short echo times. J Magn Reson 2001;153:203-209.

4. Clayton DB, Elliott MA, Leigh JS, Lenkinski RE. Characterization of gradient- induced signal modulations: implications for proton MR spectroscopic methods. Book of abstracts Ninth Annual Meeting of the International Society of Magnetic Resonance in Medicine. Glasgow: ISMRM; 2001. p. 58.

5. Serrai H, Senhadji, Clayton DB, Zuo C, Lenkinski RE. Water modeled signal removal and data quantification in localized MR spectroscopy using a time-scale postacquisition method. J Magn Reson 2001;149:45-51.

6. Serrai H, Clayton DB, Senhadji L, Zuo Ch, Lenkinski RE. Localized proton spectroscopy without water suppression: removal of gradient induced frequency modulations by modulus signal selection. J Magn Reson 2002;154:53-59.

7. Dong Z, Dreher W, Leibfritz D. Experimental method to eliminate frequency modulation sidebands in localized in vivo 1H MR spectra acquired without water suppression. Magn Reson Med 2004;51:602-606.

8. Nixon TW, McIntyre S, Rothman DL, de Graaf RA. Compensation of gradient-induced magnetic field perturbations. J Magn Reson 2008;192:209-217.

9. Chadzynski GL, Klose U. Chemical shift imaging without water suppression at 3 T. Magn Reson Imaging 2010;28:669-675.

10. Dong Z, Dreher W, Leibfritz D. Toward quantitative short-echo-time in vivo proton spectroscopy without water suppression. Magn Reson Med 2006;55:1441-1446.

11. Wu Y, Chronik BA, Bowen C, Mechefske CK, Rutt BK. Gradient-induced acoustic and magnetic field fluctuations in a 4T whole-body MR imager. Magn Reson Med 2000;44:532-536.

12. Yao GZ, Mechefske CK, Rutt BK. Characterization of vibration and acoustic noise in a gradient-coil insert. MAGMA 2004;17:12-27.

13. Clayton DB, Elliott ME, Lenkinski RE. In vivo proton MRS of the human brain at 4T without solvent suppression. Book of abstracts Seventh Annual Meeting of the International Society of Magnetic Resonance in Medicine. Philadelphia (PA): ISMRM; 1999. p. 1602.

14. Bolan PJ, DelaBarre L, Baker EH, Merkle H, Everson LI, Yee D, Garwood M. Eliminating spurious lipid sidebands in 1H MRS of breast lesions. Magn Reson Med 2002;48:215-222.

15. Elliott M, Clayton D, Lenkinski R. 1H Spectroscopy without water suppression: removal of sideband modulation at short TE. Book of abstracts Ninth Annual Meeting of the International Society of Magnetic Resonance in Medicine. Glasgow: ISMRM; 2001. p. 1667.

16. Ozdemir MS, De Denee Y, Achten E, D'Asseler Y, Lemahieu I. Quantitative proton magnetic resonance spectroscopy in the presence of sidebands. IEEE Int. Symposium Biomed. Imag. 2007;4:1008-1011.

17. De Graaf R. In vivo NMR spectroscopy principles and techniques. Baffins Lane, Chichester: John Wiley & Sons Ltd, 1998.

18. Zhou XJ, Crusher gradients. In: Bernstein MA, King KF, Zhou XJ, editors. Handbook of MRI pulse sequences. Burlington MA: Elsevier Inc, 2004. p. 305-316.

19. Groger A, Chadzynski G, Godau J, Berg D, Klose U. Three-dimensional magnetic resonance spectroscopic imaging in the substantia nigra of healthy controls and patients with Parkinson's disease. Eur Radiol 2011;21(9):1962-1969.

Chapter 4:

Chemical Shift Imaging without Water Suppression at 3T

4.1   Introduction

In proton magnetic resonance spectroscopy (MRS) of the human brain the water signal is about 3 -5 orders in magnitude higher than the metabolite signals. To be able evaluate the metabolite peaks, the water signal must be suppressed. The most accepted method for water suppression uses selective suppressing pulses that are included in the sequence and are centered at the water frequency to suppress only the water signal.

This water suppression technique is straightforward and usually offers good quality of spectra. The technique however has its limitations and disadvantages. If the frequency of the water signal is shifted because of B_0 inhomogeneities, the suppressing pulses can miss the center of the water signal. The water signal is then only partially suppressed which complicates the analysis of the spectra. Furthermore, water suppressing pulses can interfere with the metabolite resonances, because of magnetization transfer effects [1, 2]. Finally, the use of the water suppressing pulses increases the total Radio Frequency (RF) power deposition [3].

Spectroscopy without water suppression avoids these problems. The intact water signal can be used as an internal reference in metabolite quantification and for baseline corrections [3, 4]. Moreover, the development of the 16-bit Analog-to-Digital Converters (ADC) and oversampling techniques [1, 4] eliminated the problem of the receiver's dynamic range. However, the major problems in spectroscopy without water suppression are the necessity of suppressing the water signal in postprocessing and the presence of sideband artifacts, which are caused by gradient coils vibrations [5 -7].

There are several possibilities to suppress the water signal in postprocessing. The most frequently approaches used are: fitting the free induction decay signal (FID) with a combination of monoexponential functions [8, 9] and methods based on decomposition such as the Singular Value Decomposition (SVD) [1, 10, 11] or the Matrix Pencil Method (MPM) [3, 12 -14].

Fitting the FID with a combination of monoexponential functions can reduce the water signal significantly. However, a monoexponential function does not correspond to the real shape of the water signal and can thus lead to additional distortions of the spectrum [9].

In the different decomposition based methods (SVD or MPM), the water signal is reconstructed by using several exponentially dampened sinusoids. The reconstructed water signal is then subtracted from the original signal. These methods offer good quality spectra and lead to almost complete removal of the water signal. Nevertheless, in the presence of magnetic field inhomogeneities the raw FID signal can be nonexponential. If such compromised data are analyzed with for example the MPM method, nonexponential signals are fitted with a sum of exponential functions. This leads to confusions in baseline assignment and reduces the efficiency of the MPM method [14]. Preprocessing of the data may solve this problem, but will result in prolongation of the total processing time [14].

Occurrence of the sideband artifacts in the spectroscopy without water suppression is related to vibrations of the gradient coils [7]. These artifacts consist of a group of spurious peaks whose number and amplitude depend on the position within the magnet, echo time, and gradient strength [5 -7]. These peaks overlap with the metabolite signal and need, therefore, to be reduced. Recently, software- and hardware-based methods for minimizing the influence of the sideband artifacts have been presented [3, 4, 7, 8, 11, 13, 15, 16].

Software-based applications are fast and easy to implement. The first approach uses the modulus of the FID signal to obtain a real spectrum; however, this method reduces the Signal-to-Noise Ratio (SNR) [8]. The second one uses a Hankel Lanczos Singular Value Decomposition (HLSVD) for the reduction of the water signal and sidebands [11]. HLSVD removes only first order harmonics of the sidebands and is not sensitive enough to remove smaller and broader second order harmonics.

The hardware-based solutions use different variations of opposite gradients and phase cycling techniques or are based on oversampling techniques. The first kind of hardware solution uses the gradient cycling technique combined with positive and negative crusher gradients [15], inversion of the gradients [16], or a combination of the opposite gradients and phase cycling [3, 13]. These methods are robust and lead to an almost complete cancellation of the sidebands. It is important to note that multiple excitations and careful adjustments of the gradients are needed to apply these techniques. Thus, they may be too time consuming for use in clinical routine. The oversampled J-resolved technique [4]

offers cancellation of the sidebands and prevents the overloading of the ADC. However, this method requires collecting data for multiple TE to produce a TE-averaged spectrum [17] and, therefore, may not be feasible for CSI. Recently, another hardware-based approach was presented by Nixon et al. [7]. It removes the sidebands by compensating the gradient coils vibration effects with appropriate B_0 field variations. This technique is fast and reduces the sidebands to the spectral noise level but it requires hardware modifications that are usually not possible in conventional whole body systems.

The aim of this study was to develop a fast and easy postprocessing method to apply CSI without water suppression in clinical routine with reduced sideband artifacts. The water signal was reduced with a simple method based on the use of Gaussian convolution for reduction for the water signal developed by Marion et al. [18] and commonly used in in vivo brain spectroscopy [19, 20]. For the reduction of the sidebands we compared the FID signal measured in a water phantom with the FID of the in vivo measurements.

4.2   Material and methods

CSI measurements were performed on a 3T (TimTrio, Siemens, Erlangen, Germany) scanner equipped with a 12-channel and a 32-channel head coil. For each volunteer, CSI data with and without water suppression were collected.

A Point RESolved Spectroscopy (PRESS) sequence was used for volume selection in all acquisitions. The parameters used in acquisitions were: TE = 144 ms, TR = 1500 ms, field of view: 160 mm x 160 mm, excited volume: 80 x 80 x 15 mm3, voxel size: 10 x 10 x 15 mm3, matrix size: 16 x 16 voxels, vector size: 512 data points, correction for chemical shift-dependent voxel position: -2 ppm, number of averages: 3, weighted phase encoding scheme, acquisition duration 6 min 7 sec. For suppressing the water signal CHEmical- Shift Selective saturation (CHESS) provided by the scanner was used. Spectra were acquired in the magnet's isocenter in a transversal plane with and without water suppression at the upper part of the lateral ventricles. With these parameters, CSI matrix with 64 spectra was obtained.

Ten healthy volunteers, 2 females and 8 males, participated in this study after informed written consent . Ages ranged from 24 to 30 years old (mean age 26.5 +/- 1.8). All volunteers were free from neurological diseases. Five volunteers were examined with a 12-channel and five with a 32-channel head coil. All volunteer measurements were approved by the local ethical committee. For the reference measurements, a spherical water phantom (1,25g NiSo4 x 6H2O per 1,000g of distilled water) with a diameter of 16 cm was used. Additional measurements of spatial dependence of the sidebands revealed that if the distance from the magnets' isocenter to the center of the acquisition plane is not greater than 40 mm the difference in amplitude of the sideband artifact is below 10%. Therefore, unsuppressed spectra from the phantom were collected at the magnets' isocenter with the same sequence and parameters used for the in vivo measurements.

Postprocessing

Postprocessing and quantitative analysis were performed using customized software developed in Matlab version 2007b. Postprocessing consisted of three steps: correction of the water peak position in unsuppressed phantom and volunteer datasets, reduction of the water signal by applying the Gaussian convolution [18], and reduction of the sideband artifacts, done by subtraction of the FID acquired for the phantom from the volunteer's FID. The first postprocessing step was performed in the frequency domain. Subsequently, the data were processed in the time domain. After postprocessing, spectra were quantified calculating the metabolite peak integrals.

Prior to postprocessing, the data were zerofilled to 2048 data points. The water peak position in volunteer and phantom spectra was corrected by shifting the water signal to the center of the spectrum (zero frequency). The signal was shifted by evaluating the water peak position for the unsuppressed spectrum in the frequency domain and correcting the frequency in the time domain accordingly. After this correction, the maximum of the water signal and sideband artifacts in each voxel of both datasets (water phantom and volunteer) were in the same position. The water peak amplitude was reduced for both volunteer and phantom datasets by approximating the shape of the water peak with Gaussian convolution of the unsuppressed FID as described by Marion et al. [18]:

$$FID_{conv}(j) = \sum_{k} FID(k+j) \cdot exp\left(-\frac{k^2}{\sigma^2}\right)$$

(4.1)

where: $FID_{conv}(j)$ denotes the j-th element of the low-pass filtered FID (j varies from 1 to 2048 ms), $FID(j+k)$ the j+k-th element of the unsuppressed FID, k varies from -50 to 50 and σ is the kernel of Gaussian function (here σ = 5ms, bandwidth = 2000Hz).

The fitting efficiency between the low-pass filtered and the original FID was improved by adding twenty data points before the start and after the end of the FID. To preserve the trend of the original data, points added at the beginning were extrapolated along a straight line fitted to the first 10 points of the original FID, whereas points at the end were set to zero. After these preparations the Gaussian convolution was performed and the low-pass filtered FID was calculated for the original data points only (2048 data points). With this manipulation very good agreement between the original data and the low-pass filtered FID was achieved (Fig. 1a and 1c). The filtered signal was then subtracted from the FID thereby eliminating the low frequency components associated with the water signal. Fourier transform of this FID shows that the water peak was strongly reduced (Fig. 4.1).

Sidebands in certain voxels of volunteer dataset were reduced by subtracting the FID signal from the corresponding voxels measured for the water phantom. To have the same spatial distribution of the sidebands both measurements were done in the magnet's isocenter however, as mentioned previously, in the range of 40 mm from the isocenter the differences between the amplitude of the sidebands were not greater than 10%. The FID measured for the water phantom had to be normalized because of the differences in the amplitudes between these two datasets (Fig. 4.1). The normalization factor was calculated as a ratio between the amplitude of the first point of the phantom and the in vivo unsuppressed FID.
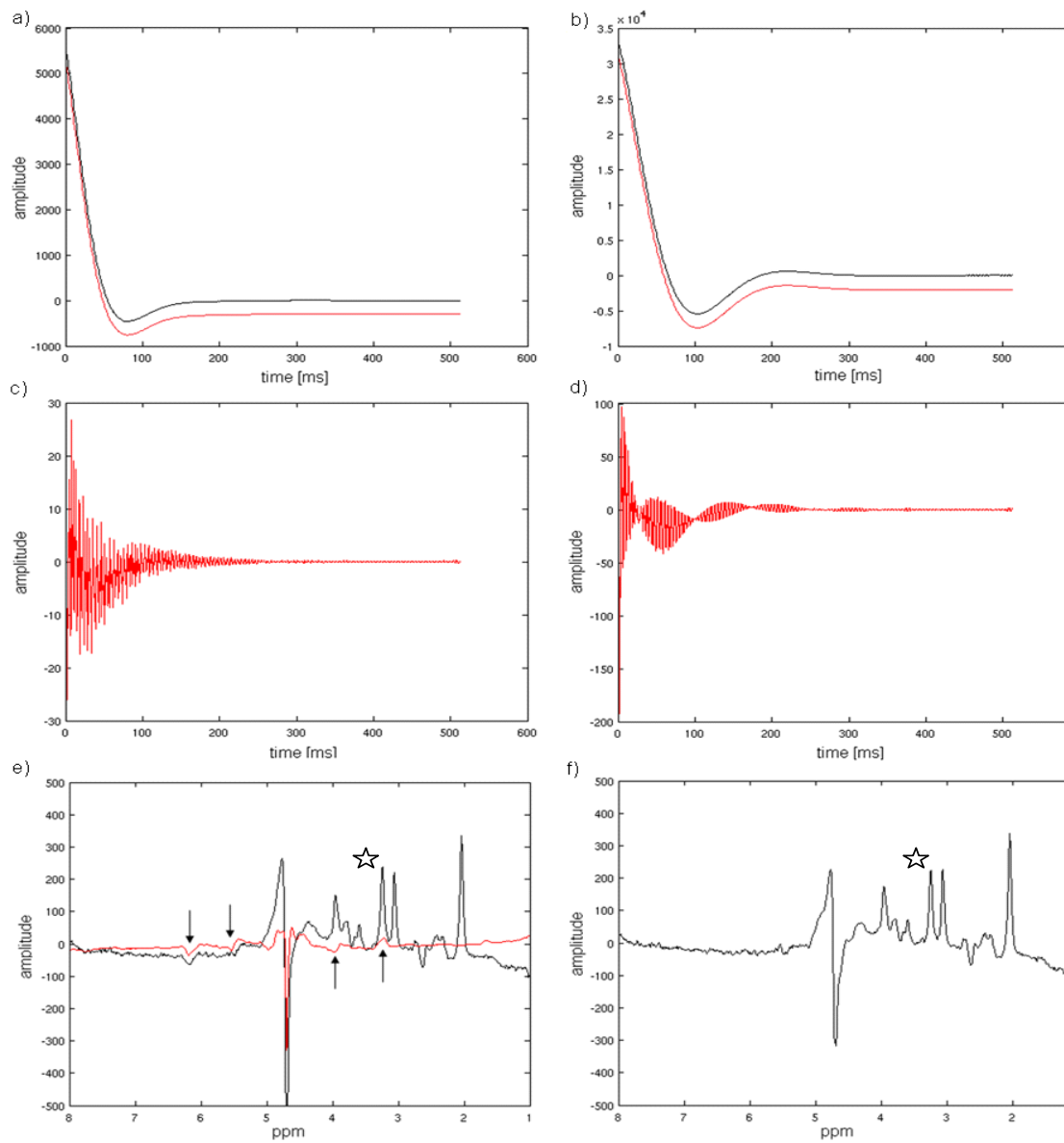
Fig. 4.1: Reduction of the water peak for the central voxel of CSI matrix. First 512 data points of the original FID signal (black) and the low-pass filtered FID (red, shifted down for better visualization) for a volunteer (a) and the water phantom (b). First 512 data points of the FID after subtraction of the low-pass filtered FID for a volunteer (c) and for the water phantom (d). Spectrum for a volunteer (black) versus spectrum for the water phantom (red) after reduction of the water signal (e). Sideband artifacts were marked with black arrows. In the upfield section of the spectrum, sideband artifacts overlap with the choline peak (marked with the star symbol). In vivo spectrum after reduction of the sidebands (f). The choline peak has now lower amplitude than before (marked with the star symbol).

Quantitative analysis

For a quantitative analysis of the processed data, the spectra obtained with the proposed method and spectra with RF suppressing pulses were compared. Peaks for three metabolites: choline, creatine, and N- Acetyl Aspartate (NAA), were investigated.

To calculate the peak integrals an appropriate baseline had to be defined. The baseline was estimated from the fragments of the spectrum for which no signals were expected: fragments were the entire downfield section of the spectrum without the water resonance and the upfield section of the spectrum between water and choline resonances, between creatine and NAA resonances, and after NAA resonance. A sixth degree polynomial function was fitted to these fragments with least square fitting procedure and used as a baseline.

The comparison for the quantitative analysis could only be done for spectra without phase problems in both measurements. Therefore, the mean peak integrals for both datasets were calculated from a selected area of 3 x 3 voxels in the entire CSI matrix to avoid phase problems present in the spectra acquired with water suppression.

4.3   Results

Even for long echo times (TE = 144 ms), the sideband artifacts affect the metabolites as shown in fig. 4.1. Before postprocessing, the main sidebands are situated at ~6.2 ppm and ~3.2 ppm. The choline peak has higher amplitude than creatine (fig. 4.1e). After the reduction of the sidebands choline peak is lower (fig. 4.1e). This is caused by the overlap between the choline signal and the sideband artifact in the upfield section of the spectrum (fig. 4.1e). The remaining part of the sideband at ~5.5 ppm and its mirrored part at ~3.9 ppm do not influence the main metabolites: choline (~3.2 ppm), creatine (~3.1 ppm) and NAA (~2.1 ppm).

Figure 4.2 shows good agreement in baseline and metabolite peak shape in the upfield section of the spectra acquired with water suppression and the method proposed in

this study. Moreover, in the spectrum collected with the new method, the main part of the sidebands was almost completely removed.

Figure 4.3 shows the results from two individual sets of CSI spectra. Both datasets were acquired for the same volunteer during one examination and originate from the same brain region. A 6 x 8 voxel CSI matrix was acquired at the upper level of the lateral ventricles (fig. 4.3a and 4.3b). In spectra with water suppression by RF pulses phase distortions are typically present in this area (fig. 4.3c). In spectra acquired without water suppression with the proposed postprocessing method no phase correction was necessary (fig. 4.3d). Identical behavior was observable for all 10 volunteers.

A quantitative analysis was achieved by comparing the metabolite peak integrals calculated from all volunteers; spectra with and without water suppressing pulses were used for the purpose. For these calculations, a 3 x 3 voxel CSI matrix with spectra without phase problems was chosen from each volunteer. The voxels in the CSI matrix were chosen to minimize the phase problems in spectra acquired with water suppression. Thus no linear or

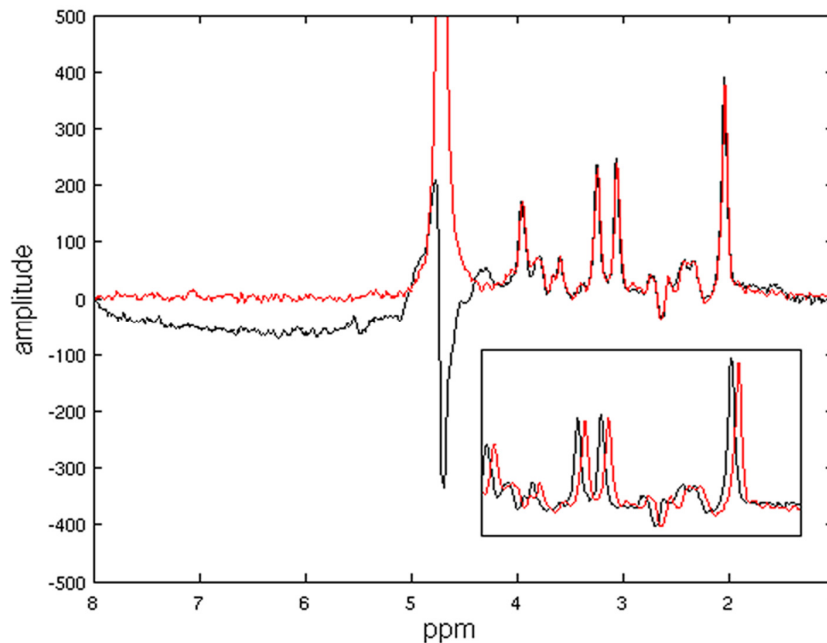

Fig. 4.2: Spectrum after reduction of the water signal and the sidebands (black) versus spectrum with water suppression CHESS pulses (red). The subplot shows a magnification of the metabolite area where the spectrum with water suppression was shifted relative to the spectrum without water suppression and the proposed postprocessing for better illustration of the similarities of the spectra.

constant phase correction of these spectra was needed. All differences calculated for all volunteers are given in percent and are generally larger for choline and creatine. The mean differences between the mean integrals obtained for spectra with and without water suppression were: 7.8 ± 2.6% (with a range of 4.2 to 10.4%) for choline, 7.6 ± 6% (with a range of 1 to 14.6%) for creatine, and 8.8 ± 5% (with a range of 2.7 to 16.2%) for NAA in
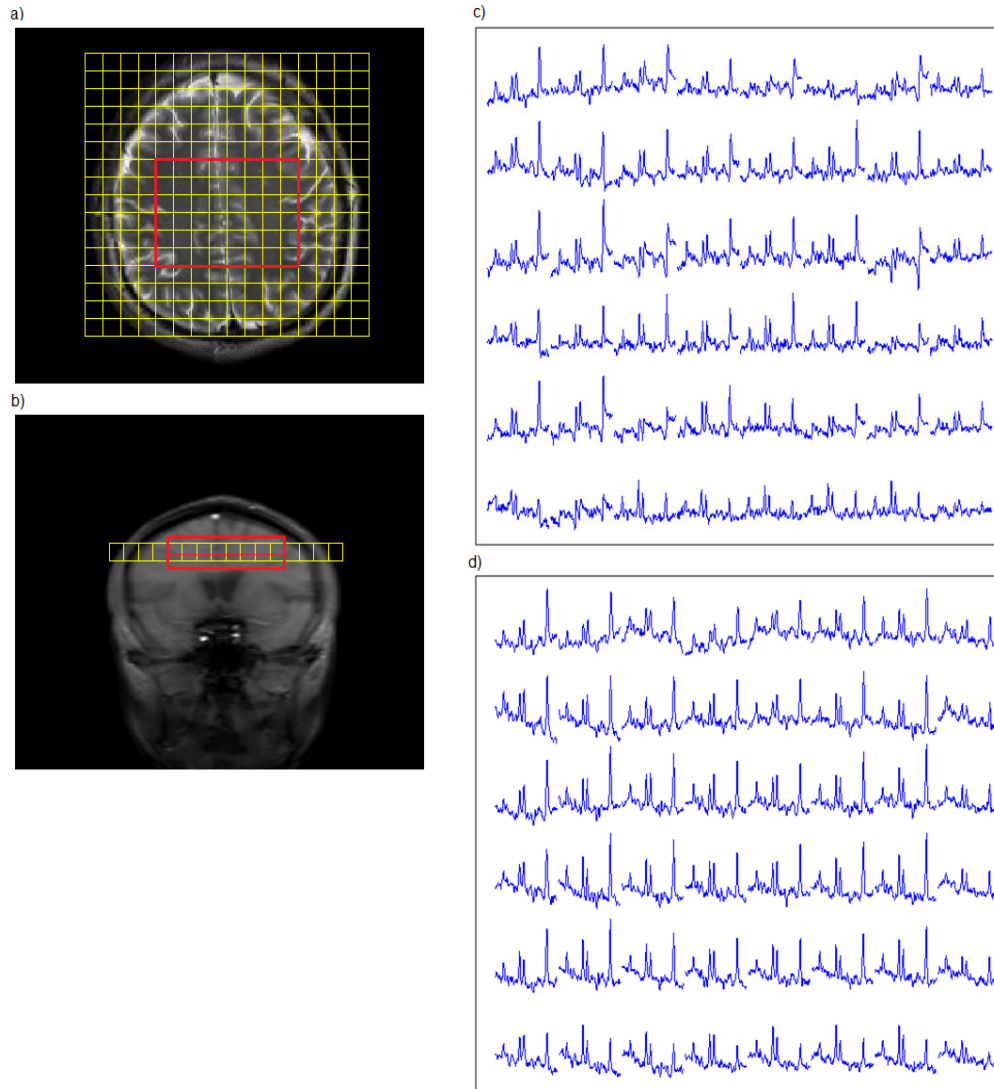

Fig. 4.3: CSI dataset from in vivo measurements. a) and b) reference images indicating the planes of the data acquisition. Red squares indicate the region where spectra were acquired. c) A 6 x 8 voxel CSI matrix of spectra with water suppressing RF pulses. d) Spectra for the same area, for the same volunteer acquired without water suppression, postprocessed with the proposed method.

measurements with the 12-channel head coil (5 volunteers). In measurements with the 32-channel coil (also 5 volunteers), those differences were: 13.8 ± 9.3% (with a range of 4.5 to 24.6%) for choline, 11.7 ± 5.9% (with a range of 4.7 to 19.1%) for creatine, and 8.8 ± 6.1% (with a range of 2.8 to 17.7%) for NAA. The overall mean differences calculated for all measured volunteers were: 10.8 ± 7.2% for choline, 9.7 ± 6% for creatine and 8.8 ± 5.3% for NAA.

4.4 Discussion

The method proposed in this manuscript allows an effective reduction of the amplitude of the water signal and the influence of the sidebands.

A low pass filter based on a Gaussian convolution is used for water signal reduction. Such filters have been proposed previously for liquid samples [18] and are often used in in vivo brain spectroscopy for reduction of the remaining water signal [19, 20]. In this manuscript Gaussian convolution is used to reduce the unsuppressed water signal in in-vivo CSI datasets. This method is not as sophisticated as the widely used MPM or SVD algorithms [1, 3, 10, 11, 13, 14] or the methods based on fitting the FID with exponential functions [8, 9]. However, as it needs less input parameters, it is more stable, is less complicated in computations, and offers sufficient water suppression.

Reduction of the sidebands is achieved by using the FID from a water phantom. This does not introduce additional SNR loss as opposed to the method proposed in [8], does not require multiple excitations as the techniques in [3, 13, 15, 16] or additional hardware development as described in [7]. The new method is not as time consuming as the oversampling techniques [4]. Because sidebands are considered to be unrelated with the load of the patient's bed [7], the sidebands generated in the water phantom can be used for reducing the ones in volunteers. To provide the same spatial distribution of the sidebands in phantom and in vivo data, as long as the distance between the acquisition plane and the isocenter is not greater than 40 mm, water phantom measurements can be performed at the magnets' isocenter with the same sequence parameters. As these phantom measurements have to be performed only once for certain geometrical conditions and sequence parameters

they are not as time consuming. This technique could, therefore, be feasible for clinical examinations.

Phase problems usually present in spectra acquired with multichannel coils and with water suppression may be explained by deficiencies in the automated phase correction. In this case the spectrum in each voxel is calculated as a weighted average of signals from each channel. Prior to the averaging, automated phase correction is applied and phase of the remaining water signal is used as a reference. If this signal is distorted or its amplitude is too small, the correct coefficients for the correction cannot be calculated from the algorithm responsible for phase correction. The presented technique avoids this problem because unsuppressed water signal can be used to calculate the correct phase correction factors. Thus spectra produced with this method do not need linear or constant phase correction applied as a postprocessing step. They are all in phase and are very similar to the spectra with water suppressing RF pulses in baseline shape and metabolite peak parameters. Calculated values of mean differences between peak integrals from spectra acquired with and without water suppressing pulses are larger in case of choline and creatine, than for NAA. Similar behavior was noticed previously [1, 2] that might be explained by magnetization transfer effects.

The proposed technique has two major limitations. Firstly, it was only successfully when applied for long echo times (144 ms). At TE of 144 ms, sidebands are strongly reduced in comparison to what can be seen at short echo times [5]. However, as presented in Fig. 4.1e, they can still hamper the metabolite signals (choline). Although measurements at short echo time are more favorable, CSI at long TE may still be useful. For instance lactate signal at long echo times is no longer overlapped with the lipids because of their short relaxation time. Moreover if the focus is on the three main metabolites (choline, creatine and NAA), acquisition with long echo times could be advantageous because of the less complicated baseline.

Moving to short echo times might be complicated because the amplitude and the number of the prominent sidebands increase with decreasing echo time [5, 6]. In case of the Siemens 3T MR systems a complete cancellation of those sidebands could be achieved with moving to echo times longer than 200 ms. The method could be improved further if the

gradient-induced oscillations could be compensated by B_0 field modulations, as was proposed by Nixon et al. [7]. Another possibility would be to perform an additional measurement with inverted gradients as described by Dong et al. [3, 13]. This would lead to cancellation of the sidebands when calculating the average spectrum from those two acquisitions.

The second limitation is related to the homogeneity of the magnetic field. In case of larger field inhomogeneities, the sideband artifacts as well as the metabolite peaks will be broader. Therefore, the presented method will have difficulties in reduction of the sidebands. This problem may be minimized by performing manual local shimming which will improve the magnetic field homogeneity; however, the total acquisition time will be longer.

The proposed method is more straightforward than the others [3, 7, 8, 13] as it uses a standard PRESS sequence available on most MR systems. It is not necessary to modify either the sequence or the hardware, which may be difficult for clinical whole-body systems.

In conclusion, the method offers sufficient quality of the spectrum even if some remnants of sidebands are still present.

4.5   Acknowledgments

4.6   References

1. Van der Veen J, Weinberger DR, Tedeschi G, Frank JA, Duyn JH. Proton MR spectroscopic imaging without water suppression. Radiology 2000;217:296–300.
2. Dreher W, Leibfritz D. Magnetization transfer MRS. NMR Biomed 2001; 14:65–76.

3. Dong Z, Dreher W, Leibfritz D. Experimental method to eliminate frequency modulation sidebands in localized in vivo 1H MR spectra acquired without water suppression. Magn Reson Med 2004;51:602–606.

4. Hurd RE, Gurr D, Sailasuta N. Proton spectroscopy without water suppression: the oversampled J- resolved experiment. Magn Reson Med 1998; 40:343–347.

5. Clayton DB, Elliott MA, Leigh JS, Lenkinski RE. 1H spectroscopy without solvent suppression: characterization of signal modulations at short echo times. J Magn Reson 2001;153:203–209.

6. Clayton DB, Elliott MA, Leigh JS, Lenkinski RE. Characterization of gradient- induced signal modulations: implications for proton MR spectroscopic methods. In: Book of abstracts Ninth Annual Meeting of the International Society of Magnetic Resonance Imaging, Glasgow: ISMRM;2001: p. 58.

7. Nixon TW, McIntyre S, Rothman DL, de Graf RA. Compensation of gradient- induced magnetic field perturbations. J Magn Reson 2008;192:209–217.

8. Serrai H, Clayton DB, Senhadji L, Zuo Ch, Lenkinski RE. Localized proton spectroscopy without water suppression: removal of gradient induced frequency modulations by modulus signal selection. J Magn Reson 2002;154:53–59.

9. Sukstanskii AL, Yablonskiy DA. Gaussian approximation in the theory of MR signal formation in the presence of structure- specific magnetic field inhomogeneities. J Magn Reson 2003;163:236–247.

10. Vanhamme L, Sundin T, Van Hecke T, Van Huffel S. MR Spectroscopy quantitation: a review of time domain methods. NRM Biomed 2001;14:233–246.

11. Elliott M, Clayton D, Lenkinski R. 1H Spectroscopy without water suppression: removal of sideband modulation at short TE. In: Book of abstracts Ninth Annual Meeting of the International Society of Magnetic Resonance Imaging, Glasgow, Glasgow: ISMRM;2001: p. 1667.

12. Lin YY, Hodgkinson P, Ernst M, Pines A. A novel detection- estimation scheme for noisy NMR signals: application to delayed acquisition data. J Magn Reson 1997;128:30–41.

13. Dong Z, Dreher W, Leibfritz D. Toward quantitative short- echo time in vivo proton MR spectroscopy without water suppression. Magn Reson Med 2006;55:1441–1446.

14. Dong Z, Dreher W, Leibfritz D. Quantification of proton MR spectroscopy without prior and post acquisition water suppression. In: Book of abstracts Eighth Annual Meeting of the International Society of Magnetic Resonance Imaging, Denver, CO: ISMRM;2000: p 1954.

15. Clayton DB, Elliott ME, Lenkinski RE. In vivo proton MRS of the human brain at 4T without solvent suppression. In: Book of abstracts Seventh Annual Meeting of the International Society of Magnetic Resonance, Philadelphia, PA: ISMRM;1999: p 1602.

16. Kreis R, Boesch C. Localized 1H-MRS without water saturation: techniques and initial results for human brain and muscle. In: Book of abstracts Sixth Annual Meeting of the International Society of Magnetic Resonance, Sidney: ISMRM;1998: p 24.

17. Bolan PJ, DelaBarre L, Baker EH, Merkle H, Everson LI, Yee D, Garwood M. Eliminating spurious lipid sidebands in 1H MRS of breast lesions. Magn Reson Med 2002; 48:215–222.

18. Marion D, Ikura M, Bax A. Improved solvent suppression in one- and two- dimensional spectra by convolution of time- domain data. J Magn Reson 1989;84:425–430.

19. Soher BJ, van Zijl PCM, Duyn JH, Baker PB. Quantitative proton MR spectroscopic imaging of the human brain. Magn Reson Med 1996;35:356–363.

20. Kreis R. Issues of spectral quality in clinical 1H-magnetic resonance spectroscopy and a gallery of artifacts. NRM Biomed 2004;17(6):361–381.

Chapter 5:

High Resolution Chemical Shift Imaging of the Human Brainstem and Cerebellum without Water Suppression at 3 T

5.1 Introduction

Proton Magnetic Resonance Spectroscopy (^{1}HMRS) can be realized with two approaches: Single Voxel Spectroscopy (SVS) and Chemical Shift Imaging (CSI). SVS is a single shot method, where only one voxel is excited and only one spectrum in obtained. Second approach, CSI consist of exciting extended region with multiple voxels. As a result a spectra matrix is obtained, where one voxel is represented by one spectrum. CSI is more sensitive to the magnetic field inhomogeneities, but offers spatial information about metabolite distribution.

The main problem in proton MRS is the amplitude of the water signal, which may be about four orders higher than the amplitude of the metabolite resonances. Therefore water signal must be suppressed for quantitative analysis. The most accepted method for water suppression is to use water suppressing pulses. However in the presence of mangeitc field inhomogeneities, water suppressing pulses may miss the main part of the water signal and suppress it partially. This leads to the complications in the baseline and hampers the quantitative analysis. Water suppressing pulses can affect the amplitude of metabolite resonances due to the magnetization transfer effects [1, 2].

CSI without water suppression is free from these problems. Additionally it offers the advantage of availability of the intact water signal. It may be used as a reference for quantitative analysis and baseline corrections [2, 3]. Moreover spectra acquired without water suppression do not need phase correction [4]. The drawbacks of spectroscopy without water suppression are the necessity to suppress water signal in postprocessing and the presence of the sideband artifacts caused by the vibrations of the gradient coils [5, 6].

The most frequently used postprocessing algorithms of suppressing the water signal are based on decomposition. These methods, like Singular Value Decomposition, (SVD) [1, 7] or Matrix Pencil Method (MPM) [2, 8- 10], decomposes FID signal into a group of exponentially damped sinusoids. Water signal is reconstructed from sinusoids with lowest frequencies and then subtracted for the original FID. This suppressing algorithm offers almost complete removal of the water signal. However in case of magnetic field inhomogeneities the FID may contain non-exponential components. Decomposition of such

data with for example MPM method leads to the situation when non-exponential signal is reconstructed with exponential functions and this reduces the efficiency of the MPM method [10]. Possible solution for this problem is additional preprocessing of these data, but this will result in prolongation of the total processing time [10].

In the proposed method reduction of the water signal was performed with Gaussian convolution. This is not as robust as SVS or MPM however offers sufficient reduction of the water signal. Moreover it is not as sensitive to the occurrence of the non-exponential components of the FID signal.

The sideband artifacts caused by the gradient coil vibrations consist of a group of spurious peaks which overlap with the metabolite resonances and need therefore to be suppressed. The most effective methods to do this are those based on the compensation of the sideband artifacts by the usage of the opposite gradients [1, 9] or the B_0 field modulations [6]. Both methods require however hardware modifications which are usually not possible in conventional whole body systems.

The proposed method uses the FID signal measured for the water phantom for reduction of the sidebands. Sideband artifacts are considered to be not related with the load of the patient's bed [6] and thus it is possible to reconstruct them with water phantom and subtract from the original data.

Since spectra obtained with the new method do not need phase corrections it is possible to use a few voxels which lies within the particular region of interest and calculate the mean spectrum [4]. With this procedure an additional gain in SNR may be obtained and measurements with smaller voxelsize can be performed.

The aim of this study is to demonstrate the feasibility of high resolution CSI without water suppression with the proposed postprocessing technique in the areas such as Substantia Nigra (SN) and Nucleus Dentatus (DN) which are known to introduce magnetic field inhomogeneities and therefore are difficult for MRS.

5.2   Material and Methods

Volunteers

Six healthy volunteers participated in this study (one female, five males). Ages ranged from 25 to 30 years old (mean age 29.2 ± 3.5). All volunteers were free form neurological diseases. Three of them were examined at the level of Substantia Nigra (SN) and the rest at the level of Nucleus Dentatus (DN). In accordance with institutional standards written informed consent was obtained from each volunteer prior the examination.

Data Acquisition

CSI measurements were performed at a 3T whole body scanner (TimTrio Siemens, Erlangen, Germany) equipped with a 32 channel head coil. A Point RESolved Spectroscopy (PRESS) sequence was used for volume selection.

Parameters of the CSI acquisition were: TR = 1350 ms, TE = 144 ms, field of view: $120 \times 120 \times 10$ mm^3 (DN) and $140 \times 140 \times 10$ mm^3 (SN) , excited volume of interest: $50 \times 50 \times 10$ mm^3 (DN) and $30 \times 40 \times 10$ mm^3 (SN), voxelsize $3.75 \times 3.75 \times 10$ mm^3 (DN) and $4.38 \times 4.38 \times 10$ mm^3 (SN), vectorsize: 1024 data points, weighted phase encoding scheme, automatic shimming for DN and manual shimming in case of SN. In all the cases total acquisition time was approximately 16 min.

For a comparison of spectral quality an additional single voxel spectroscopy (SVS) measurement with water suppression at the level of SN was performed. The parameters of this acquisition were as follows: TR = 1500 ms, TE = 144 ms, voxelsize: $20 \times 20 \times 20$ mm^3, vectorsize: 1024 data points, number of averages: 128, total acquisition time: ~3 min.

For the reference measurements a spherical water phantom (per 1000g of distilled water 1.25g $NiSO_4 \times 6H_2O$) with a diameter of 16 cm was used. Unsuppressed spectra from the phantom were collected with the same sequence and the same parameters as used for in-vivo measurements. For further postprocessing a mean FID signal for the water phantom was defined as a mean value over the whole excited volume (mean from the 64 FIDs)

Postprocessing

The whole postprocessing was done in four steps: zerofilling of all the unsuppressed FID signals, correction of the water peak position in unsuppressed phantom and volunteer datasets, reduction of the water signal by Gaussian convolution and reduction of the sideband artifacts by subtracting the FID acquired for water phantom from the volunteer's FID. First step was performed in the frequency domain and the rest of postprocessing was done in the time domain.

Detailed analysis of time domain data revealed that the first four points of each single FID signal tends to show abnormal oscillations (Fig. 5.1). This can be explained by the influence of the last pair of the crusher gradients (used for dephasing of unwanted coherences produced by volume selection) present in the PRESS sequence [11] on the acquired signal within the range of first milliseconds of the FID. As seen in Fig. 5.1 b, direct Fourier transformation of such distorted time-domain signal would give a rise to linear phase errors. Therefore, before zerofilling the acquired time domain data were corrected: undisturbed FID signal was extrapolated with a straight line. Then the first four points of the original FID signal were replaced with the points evaluated by extrapolation. Subsequently CSI data were zerofilled to 2048 points.

Afterwards the water signal was shifted to the center of the spectrum (zero frequency). This was done by evaluating the position of the water signal in frequency domain and applying this correction in the time domain. After this step maxima of the water signal in volunteer and phantom datasets were at the same positions.

Reduction of the water signal amplitude was done by approximating the shape of the water peak with Gaussian convolution [12, 13]. Since the calculated convoluted line converges to zero at its beginning, the fitting efficiency was improved by the extension of the data prior to the convolution. This was done by adding 40 data points to the original FID. Points added before the start (20 data points) were extrapolated along the straight line fitted to the first 10 points of the original data while point at the end (20 data points) were set to zero. Next to this manipulation the Gaussian convolution was performed. The convoluted line was calculated for the expanded dataset. However, the subtraction was

performed for the original dataset only (2048 data points). This extension of the original dataset allowed avoiding the situation in which the convoluted line subtracted from the original data would introduce additional distortions. As a result a FID signal without lowest frequency components associated with the water signal was obtained. Sideband artifacts were reduced by a subtraction the FID signal measured with the water phantom from the in-vivo FID. Prior to this reduction both datasets had to be normalized regarding to the amplitude of the water signal. The normalization factor, defined as a ratio between the amplitude of the first point of unsuppressed FID obtained with the water phantom and unsuppressed FID for volunteer was calculated and applied to the water phantom dataset.
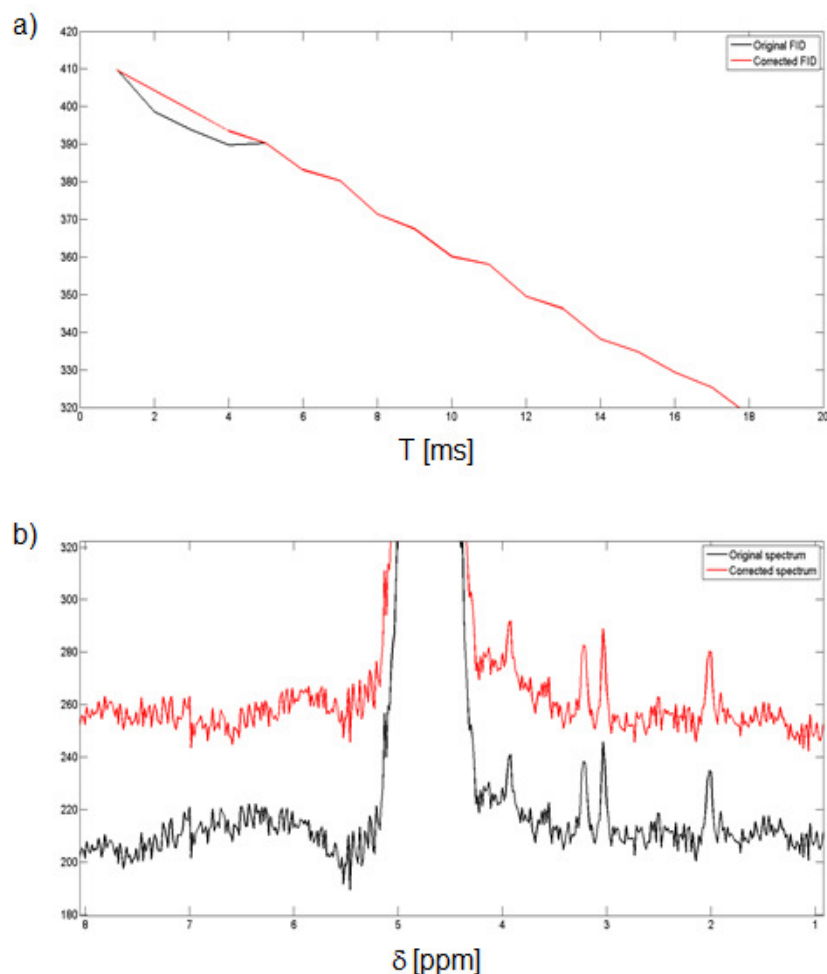

Fig. 5.1:Correction of the first 3 points of FID signal: original FID depicted in black (a), corrected FID depicted in red (b), original spectrum plotted in black (a) and corrected spectrum with artificial offset depicted in red (b).

Since SVS spectra were acquired with water suppression, they were postprocessed with the same steps, with the exclusion of water signal and sideband artifacts reduction.

Averaging procedure was applied to the postprocessed spectra for improving the SNR. The average spectrum was calculated as a mean from 9 spectra acquired for one central voxel and 8 nearest neighbors. All voxels were situated next to each other. The central voxel was situated directly in the middle of the measured structure (SN or DN). The dimensions of the volume for which the average spectrum was calculated were: $11.3{\times}11.3{\times}10$ and $13.1{\times}13.1{\times}10$ mm^3 for DN and SN respectively.

For comparison between SVS and CSI spectra acquired at the level of SN a summation spectrum from the CSI measurements was used. This spectrum was calculated as a sum of spectra from $4{\times}4$ voxels area placed directly in the center of the SN. In this case, the size of this volume was $17.5{\times}17.5{\times}10$ mm^3, so the in-plane dimensions were chosen to be comparable to the voxel size used for SVS acquisition ($20{\times}20{\times}20$ mm^3).

5.3   Results

The presented spectra and metabolite maps were acquired at the two different regions of the brain: Nucleus Dentatus (DN) and Substantia Nigra (SN).

On Fig. 5.2 spectra and the metabolite map for N-acetyl aspartate (NAA) from DN are presented. Localization of the excited volume is shown at the localizer image and is marked with the blue square (Fig. 5.2 a). The smallest red square denotes the localization of the single spectrum (Fig. 5.2 c), while bigger red square marks the localization of all spectra used for calculating the average spectrum (Fig. 5.2 d). The metabolite map (Fig. 5.2 b) show almost symmetrical distribution of NAA within the excited volume. This means, that all obtained spectra are in phase. It can be noticed that spectrum obtained without averaging procedure, offers good quality, however some noise is present (Fig. 5.2 c). This noise was minimized with the averaging procedure, as shown on Fig. 5.2 d. This was noticed for all the volunteers.

Fig. 5.3 shows spectra and again the metabolite map for N-acetyl aspartate from SN. The excited volume is shown on the localizer image and again marked with the blue square
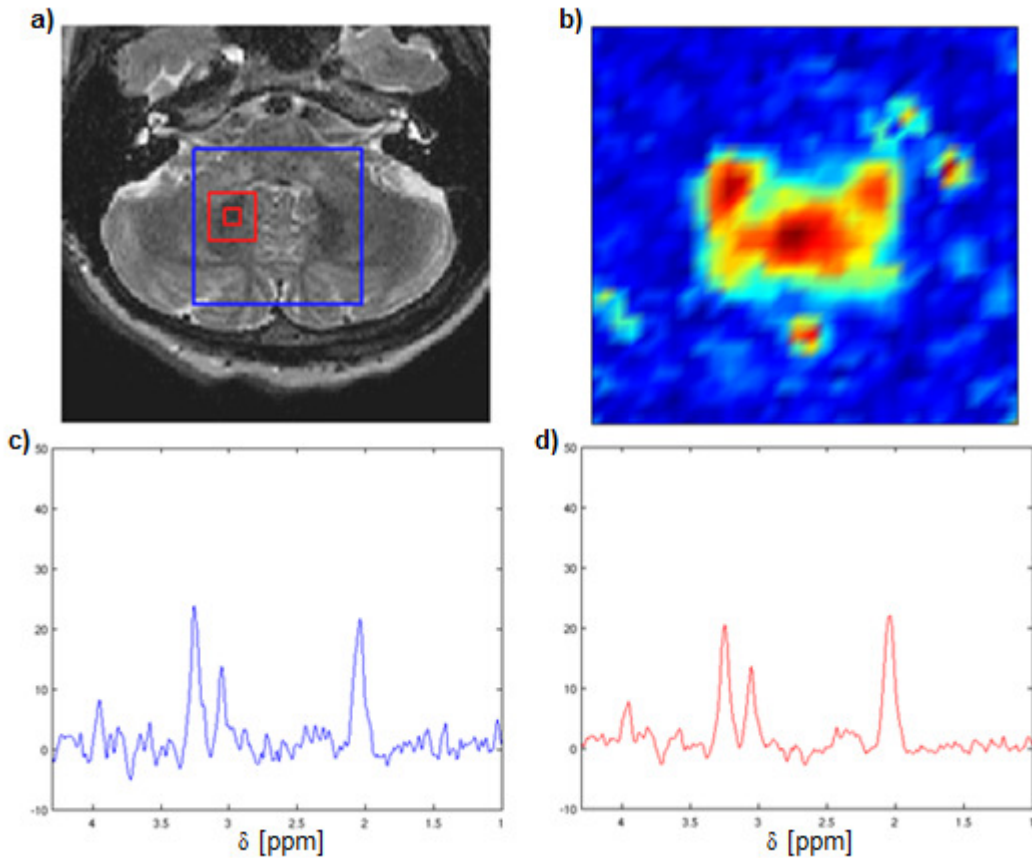
Fig 5.2: Results of the high resolution CSI at the level of DN. Localizer image (a), NAA intensity map (b), single spectrum from the center of SN (c) and average spectrum (d).

(Fig. 5.3 a). The region, where the single spectrum (Fig. 5.3 c) came from is denoted with the smallest red square, while bigger red square indicates the localization of voxels used to calculate the average spectrum (Fig. 5.3 d). Metabolite map (Fig. 5.3 b) also in this case demonstrates symmetrical distribution of NAA inside of the excited volume. Consequently this means that all spectra were free form phase distortions. Once more the gain in SNR in the case of average spectrum was obtained (Fig. 5.3 d). Again this was noticed for all the measured volunteers.

Metabolite maps presented on Fig. 5.2 b and Fig. 5.3 b were calculated within whole field of view and correspond to the size of the localizer images shown on Fig. 5.2 a and Fig. 5.3 a. Red color denotes the higher amplitude of the NAA signal and corresponds with the excited volume marked with blue square on localizer images (Fig. 5.2 a and Fig. 5.3 a). Both figures: 5.2 and 5.3 use the same scale. Smaller amplitude of the spectra from
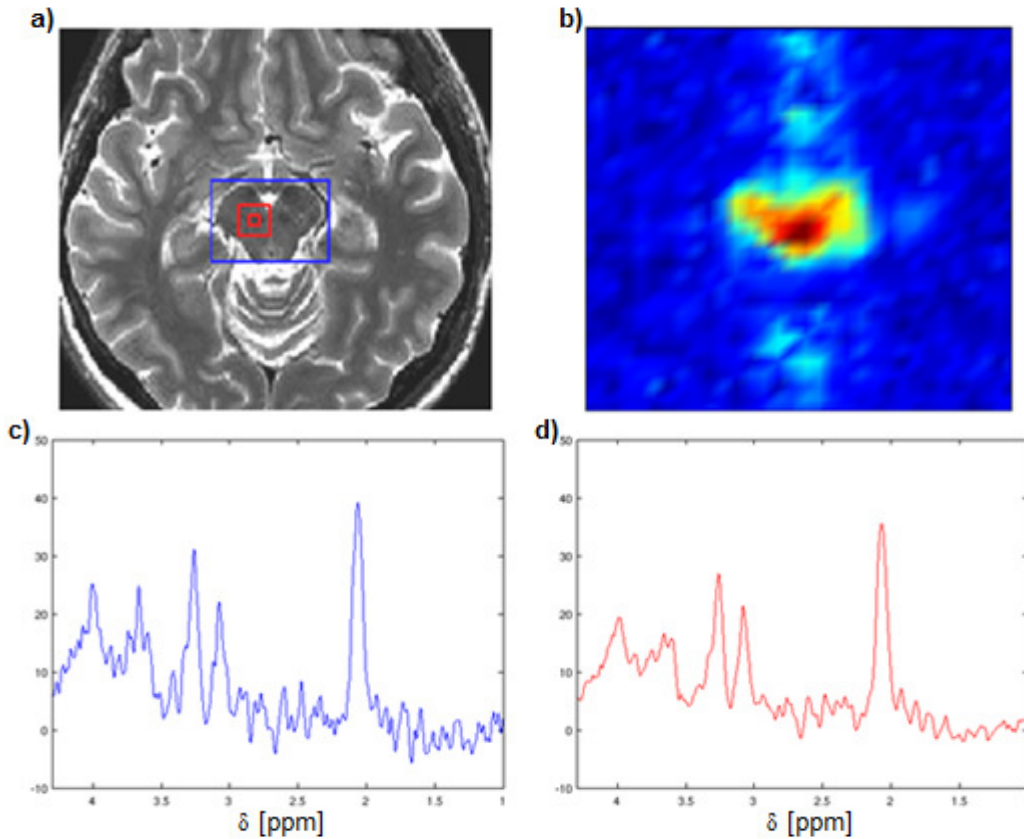
Fig 5.3: Results of the high resolution CSI at the level of SN. Localizer image (a), NAA intensity map (b), single spectrum from the center of SN (c) and average spectrum (d).

DN (Fig. 5.2 c and d) is caused by smaller voxelsize ($3.75 \times 3.75 \times 10$ mm^3). Voxel size of spectra from SN (Fig. 5.3 c and d) was $4.38 \times 4.38 \times 10$ mm^3.

Figure 5.4 demonstrates the comparison between SVS and CSI spectra acquired in the region of SN. Larger red square seen on the localizer image (5.4 a) denotes the volume which corresponds to the voxel size used for SVS acquisition. This area also corresponds to the 4×4 voxel area for which a summation CSI spectrum was calculated. It can be noticed that both CSI spectra: single and summation (5.4 c and d) shows better SNR and spectral resolution than the SVS spectrum (5.4 b). The differences in scale between the SVS and summation spectra seen in Fig 5.4 b and d respectively may be explained by the differences in the volume from which both the spectra were obtained (8 ml for SVS spectrum and 3.07 ml for summation CSI spectrum).
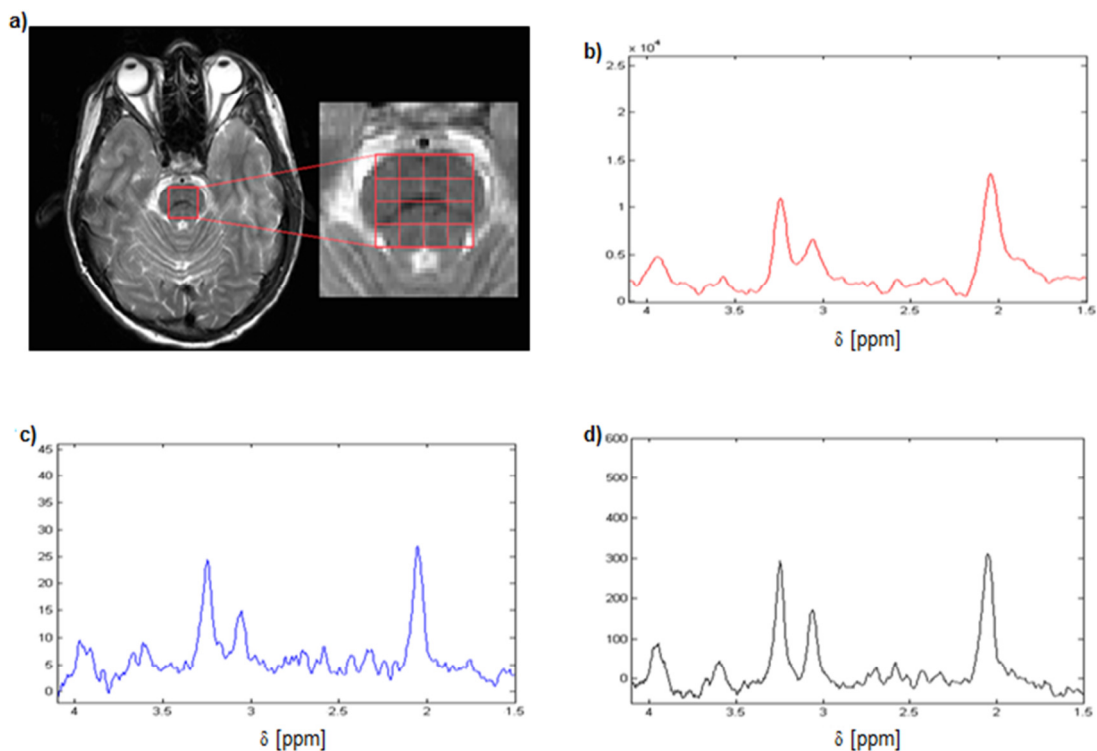
Fig. 5.4: Comparison of the SVS and CSI spectra acquired at the level of SN. Localizer image (a), SVS spectrum (b), single CSI spectrum (c) and summation CSI spectrum with frequency shift correction (d).

5.4   Discussion

The described method offers effective reduction of the water signal and the sideband artifact. Suppressing of the water signal is based on the usage of the low pass Gaussian filter. This was proposed previously for solid state samples [12]. Here Gaussian convolution was used for reduction of the water signal in iv-vivo CSI datasets. This is not as effective as the decomposition-based algorithms (MPM or SVD) [1, 2, 7, 9, 10]. However, the proposed method is less sensitive to the non-exponential components of the FID which are caused by B_0 field inhomogeneities [10] and offers sufficient water suppression.

As reported in previous studies [14- 19], both examined regions: DN and SN are known to be difficult to access with SVS or CSI. This is because of the presence of large

blood vessels which may introduce motion related artifacts and due large tissue heterogeneity of the both areas which can increase the B_0 field inhomogeneities. Moreover, the region of SN compared with DN is even more demanding, because of higher content of cellular iron which gives further increase in magnetic field inhomogenities [14, 15]. This results in increased linewidth of metabolite resonances and in more complicated shape of the spectral baseline. (Fig. 5.2 and Fig. 5.3). Therefore both regions SN and DN are not so often chosen as a target of CSI or SVS acquisition, despite of the fact that spectra acquired there may provide relevant information about different pathologies [14, 19].

Direct comparison of the obtained results with those published in the literature [17-19] is rather difficult. This is because of the differences in the acquisition details such as voxel size, echo time or even pulse sequence used for measurements. However as seen in Fig. 5.5, spectra acquired with the proposed method and postprocessed with the developed algorithms demonstrate better SNR and better spectral resolution, regardless of the fact that they were acquired from smaller volume.

The usage of the FID from the water phantom for reduction of the sidebands does not require additional hardware modifications as described in [1, 6, 9]. Furthermore sideband artifacts are supposed to be not related with the patients' bed load [6]. It is therefore reasonable to use the sidebands generated in the water phantom to reduce those in the patients. These phantom measurements have to be performed only once for the certain geometrical conditions, therefore it is not as time consuming and could be more feasible for clinical examinations.

Since the described postprocessing method offers spectra free from phase problems [4] it is possible to apply the averaging procedure and calculate the average spectrum. This spectrum offers higher SNR than single one. The gain in SNR was noticed for all volunteers. However, it should be pointed out that the typical voxel size used in CSI measurements ($4.38 \times 4.38 \times 10$ and $3.75 \times 3.75 \times 10$ mm^3) is still bigger than the size of measured anatomical structures therefore, the applied averaging procedure may lead to further increase in partial volume effects.

The proposed method has one major limitation. It can be applied only for long echo times (TE = 144 ms), because the amplitude of the sideband artifacts at short TE (30 ms) is

too high [13]. Despite of this fact, CSI without water suppression combined with the described postprocessing method may be feasible for acquisition in difficult and inhomogeneous areas such as Substantia Nigra or Nucleus Dentatus.
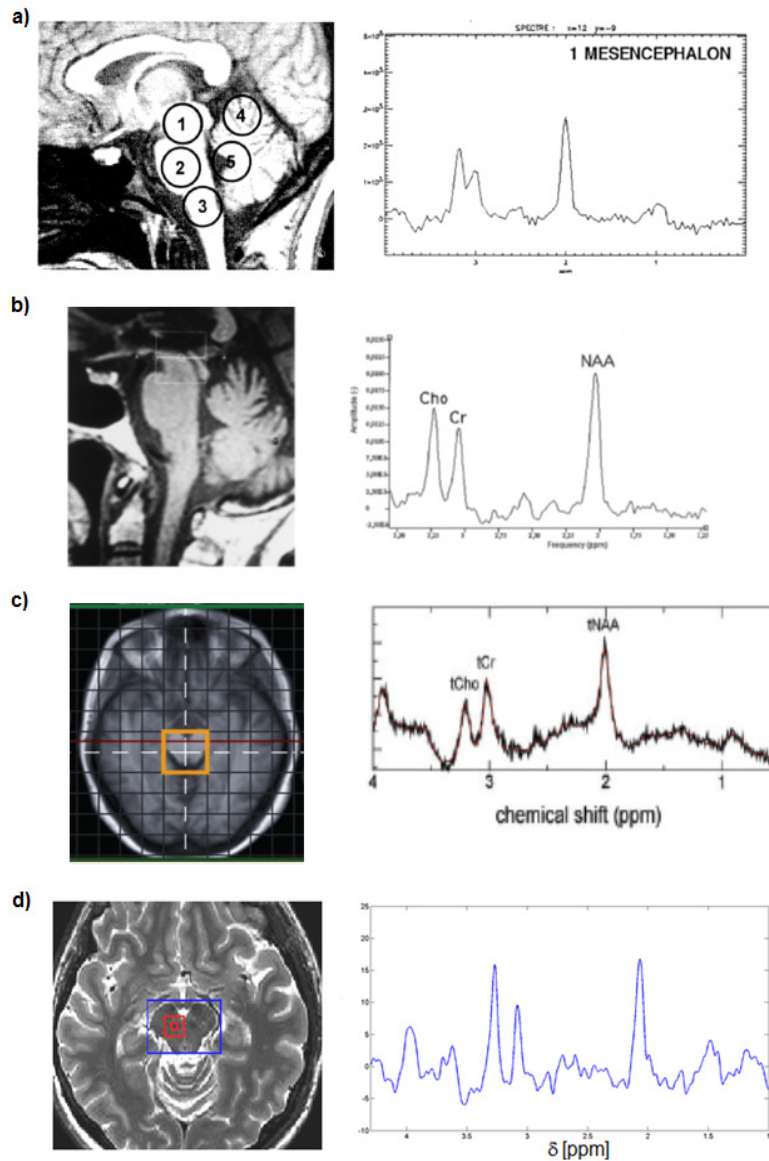
Fig. 5.5: Comparison of the spectra acquired from the brainstem: CSI spectrum from a healthy volunteer acquired at 1.5T with a home developed hamming shape pulse sequence with TE of 136 ms (a) [17], SVS spectrum from a healthy volunteer acquired at 1.5T with PRESS sequence with TE of 136 ms (b) [18], CSI spectrum from a patient with Parkinson's disease acquired at 3T with PRESS sequence at TE of 30 ms (c) [19], single CSI spectrum from healthy volunteer acquired at 3T with PRESS sequence with TE of 144 ms (this study, d)

Lack of the phase problems in acquired CSI spectra allows performing local frequency corrections even for a small voxelsize. With this correction application of the averaging procedure to acquired CSI data is possible. Moreover the average spectra may also be calculated for asymmetric areas which can better correspond to the certain anatomical structures.

5.5   Acknowledgments

5.6   References

1. Van der Veen J, Weinberger DR, Tedeschi G, Frank JA, Duyn JH. Proton MR spectroscopic imaging without water suppression. Radiology 2000;217:296–300.

2. Dong Z, Dreher W, Leibfritz D. Experimental method to eliminate frequency modulation sidebands in localized in vivo 1H MR spectra acquired without water suppression. Magn Reson Med 2004;51:602-606.

3. Hurd RE, Gurr D, Sailasuta N. Proton spectroscopy without water suppression: the oversampled J-resolved experiment. Magn Reson Med 1998;40:343-347.

4. Chadzynski GL, Klose U (2009) CSI of the human brain without water suppression at 3T. Book of abstracts Seventeenth Annual Meeting of the International Society of Magnetic Resonance in Medicine. Honolulu, HI: ISMRM; 2009. p. 2354.

5. Clayton DB, Elliott MA, Leigh JS, Lenkinski RE. 1H spectroscopy without solvent suppression: characterization of signal modulations at short echo times. J Magn Reson 2001;153:203-209.

6. Nixon TW, McIntyre S, Rothman DL, de Graaf RA. Compensation of gradient-induced magnetic field perturbations. J Magn Reson 2008;192:209-217.

7. Elliott M, Clayton D, Lenkinski R. 1H Spectroscopy without water suppression: removal of sideband modulation at short TE. Book of abstracts Ninth Annual Meeting of the International Society of Magnetic Resonance in Medicine. Glasgow: ISMRM; 2001. p. 1667.

8. Lin YY, Hodgkinson P, Ernst M, Pines A. A novel detection- estimation scheme for noisy NMR signals: application to delayed acquisition data. J Magn Reson 1997;128:30–41.

9. Dong Z, Dreher W, Leibfritz D. Toward quantitative short- echo time in vivo proton MR spectroscopy without water suppression. Magn Reson Med 2006;55:1441–1446.

10. Dong Z, Dreher W, Leibfritz D. Quantification of proton MR spectroscopy without prior- and post-acquisition water suppression. Book of abstracts Eighth Annual Meeting of the International Society of Magnetic Resonance in Medicine. Denver, CO: ISMRM; 2000. p. 1954.

11. De Graaf RA. In vivo NMR spectroscopy principles and techniques. Chichester West Sussex: John Wiley & Sons; 1998.

12. Marion D, Ikura M, Bax A. Improved solvent suppression in one- and two-dimensional spectra by convolution of time- domain data. J Magn Reson 1989;84:425–430.

13. Chadzynski GL, Klose U. Chemical shift imaging without water suppression at 3 T. Magn Reson Imaging 2010;28:669-675.

14. Groger A, Chadzynski G, Godau J, Berg D, Klose U. Three-dimensional magnetic resonance spectroscopic imaging in the substantia nigra of healthy controls and patients with Parkinson's disease. Eur Radiol, 2011;21(9):1962-1969.

15. Galazka-Friedman J, Friedman A, Bauminger ER. Iron in the brain. Hyperfine Interact 2009;189:31-37.

16. Ordidge RJ, Gorell JM, Deniau JC, Knight RA, Helpern JA. Assessment of relative brain iron concentrations using T2-weighted and T2*-weighted MRI at 3 Tesla. Magn Reson Med 1994;32:335-341.

17. Galanaud D, Le Fur Y, Nicoli F, Denis B, Confort-Gouny S, Ranjeva JP, Viout P, Pelletier J, Cozzone PJ. Regional metabolite levels of the normal posterior fossa studied by proton chemical shift imaging. Magn Reson Mater Phy 2001;13:127-133.

18. Mascalchi M, Brugnoli R, Guerrini L, Belli G, Nistri M, Politi LS, Gavazzi C, Lolli G, Argenti G, Villari N. Single-voxel long TE 1H-MR spectroscopy of the normal brainstem and cerebellum. J Magn Reson Imag 2002;16:532-537.

19. Hattingen E, Magerkurth J, Pilatus U, Mozer A, Seifried C, Steinmetz H, Zanella F, Hilker R. Phosphorus and proton magnetic resonance spectroscopy demonstrates mitochondrial disfunction in early and advanced Parkinson's disease. Brain 2009;132:3285-3297.

Chapter 6:

Tissue Specific Resonance Frequencies of Water and Metabolites within the Human Brain

6.1 Introduction

In proton magnetic resonance spectroscopy (^{1}H-MRS) water signal strongly dominates over metabolite resonances, therefore it is usually suppressed. This approach is straightforward, however it has some disadvantages: signals that are close to the water signal resonance frequency are partially suppressed [1], magnetization transfer effects can hamper the metabolite quantification [2] and water suppressing pulses may introduce phase distortions [3]. MRS without water suppression avoids these problems and additionally allows using unsuppressed water signal for absolute quantification as an internal reference. The potential drawback of this technique is the presence of unwanted sideband artifacts [4]. However, recently a couple of solutions for this problem have been demonstrated [1, 3, 5, 6]. Furthermore, analysis of resonance frequency of the water signal may provide additional information. Current studies have revealed that the resonance frequency of water can be influenced by various factors, like temperature [7 -11], pH value [12], water-macromolecule proton exchange [13] and susceptibility [13 -16].

The influence of temperature on the contrast of T_1 weighted MR images was proven almost 30 years ago [17]. Furthermore, it was also demonstrated that temperature and pH value affect the resonance frequency of water and other substances [7, 12]. This effect can be identified with proton spectroscopy and used for non- invasive temperature and pH mapping. Both physiological parameters can be estimated by calculating the frequency distance between water and metabolites (choline, creatine and N-acetyl aspartate (NAA)) [8, 10].

Proton exchange between water and macromolecules and susceptibility effects are known to be responsible for frequency shifts of the water signal. Both effects are suggested to contribute to the contrast between gray (GM) and white matter (WM) within the human brain seen in gradient -echo phase MR images [14 -16, 18]. Proton exchange effect consists of movement of protons between water and macromolecules, mostly proteins, in exchange between bounded and free water and in spin -spin interactions between free water and macromolecules, as known from magnetization transfer studies [14]. Those mechanisms influence the shielding constant of protons in the water molecule and therefore lead to the

shift of the water resonance frequency. They also influence the T_1 and T_2 relaxation times of water and contribute to the phase contrast between GM and WM [14, 15]. Another factor responsible for those frequency shifts are susceptibility variations caused by chemical composition and geometrical arrangement of the brain tissue. Non-heme iron compounds [19 -22], deoxyhemoglobin and proteins [23, 24] were proposed as chemically based sources of those variations. Moreover, the relationship between MR signal phase/frequency and magnetic susceptibility depends on tissue architecture on subcellular and cellular levels that is determined by the structural arrangement of susceptibility inclusions (non -heme iron, deoxyhemoglobin or proteins) [15]. This can be addressed as a geometrically based source of susceptibility variations and it has been found to give a frequency difference between GM and WM of approximately 15.7 parts per billion (ppb) [15]. Recently, Luo et al. [13] have evaluated the contribution of susceptibility variations and proton exchange effects to the shift of the resonance frequency of water. These authors demonstrated that the effects related to susceptibility are approximately two times stronger than proton exchange effects and shift the resonance frequency in the opposite direction.

All these observations refer to the behavior of the water signal only. MRS without water suppression allows accessing the resonance frequency of water and the resonance frequencies of the main metabolites. In combination with chemical shift imaging (CSI) the behavior of resonance frequencies can be described simultaneously for different locations.

In this study, the resonance frequencies of water and metabolites within the central part of the human brain have been examined. A CSI sequence without water suppression at the level of the lateral ventricles was performed to assess the resonance frequencies of water, total choline (tCho), total creatine (tCr) and NAA. The accuracy of data acquisition procedure was corrected with respect to the chemical shift displacement in the slice-selection direction. This has been done by calculating the metabolite-specific chemical shift displacement values. As a result, CSI acquisition was repeated for the slices with the position corrected accordingly.

The aim was to determine if there are any regional differences in resonance frequencies of water and metabolites within the central part of the human brain.

Furthermore, the potential influence of chemical shift displacement in slice-selection direction on the mentioned frequency differences was evaluated.

6.2   Materials and Methods

All unsuppressed CSI spectra were acquired with a 3- Tesla MR scanner (TimTrio, Siemens, Erlangen, Germany) equipped with a 32-channel receive- only head coil.

Point resolved spectroscopy (PRESS) localization technique was used for excitation. A 2D CSI matrix was placed above the lateral ventricles, parallel to the line between the anterior and posterior commissures (ac -pc line). Parameters of this acquisition were as follows: TE = 144 ms, TR = 1350 ms, field of view (FOV): 140×140 mm^2, excited volume of interest (VOI) $70 \times 70 \times 7$ mm^3, voxel size: $5.8 \times 5.8 \times 7$ mm^3, CSI matrix: 24×24 voxels (interpolated to 32×32 voxels), vector size: 512 complex data points, correction for chemical shift-dependent voxel position: -2 parts per million (ppm), number of averages: 4, spectral bandwidth: 1000 Hz and weighted phase encoding scheme. With these acquisition parameters total scanning time for the single CSI slice was 15 min 56 s.

Elliptical weighted k-space sampling was used in one of our previous studies [25]. The algorithm omits the high k-space frequencies, while the low k-space frequencies according to the apodization during acquisition were more pronounced to improve the sensitivity over detail and resolution [25]. This scheme reduced the amount of the k-space data to approximately 30% and increased the effective voxel size.

The chemical shift displacement in the slice-selection direction was evaluated to be 1.1 mm, 1.2 mm and 1.9 mm, for total choline, total creatine and NAA slices respectively [26].

Data acquisition was repeated for the slices with the position corrected for chemical shift displacement of evaluated metabolites. Since the difference in position of the slices for tCho and tCr was negligible (approximately 0.1 mm) three CSI slices were acquired: the reference slice, 2nd slice shifted by 1.2 mm and 3rd slice shifted by 1.9 mm in slice-selection direction. Frequency adjustments were done manually and the adjusted volume was

expanded from 7 to 11 mm, to cover all three CSI slices. With this manual shimming procedure performed with linear field gradients only, the full width at half maximum of water signal in all measurements was between 13.9 to 17.8 Hz and T_2^* time was from 18 to 23 ms.

For reference measurements, a spherical water phantom (8.07 mmol $NiSO_4$ per $1dm^3$ of distilled water) was used. Water phantom data were collected with the same sequence parameters as volunteer data. Those measurements were done for a single slice only.

In -vivo spectra were acquired from 9 volunteers, 4 females and 5 males, after informed written consent in accordance with the local ethical committee. Ages ranged from 24 to 31 years (mean age 27.5 ± 1.5 years). Volunteers reported no known neurological diseases.

CSI spectra were postprocessed with customized software written under Matlab (2009b, MathWorks, Natick, MA, USA). After the acquisition, data were zero-filled to 2048 complex data points. After the Fourier transformation (FFT), the resonance frequency of the water signal was determined. Subsequently the amplitude of water signal was reduced. This was achieved in time domain by convolution of the unsuppressed FID signal with a Gaussian function (low-pass filter) with full width at half maximum (FWHM) of 5 ms and subtraction of the convoluted line from the original data set [3]. For minimization of the gradient related sidebands, present in the unsuppressed *in -vivo* spectra, the FID signal measured for the water phantom was used. Sidebands in *in -vivo* voxels were reduced by subtracting the FID signal from the corresponding voxel in water phantom measurements [3]. To reduce noise in postprocessed FID signals, a Hanning filter with time constant of 200 ms was applied. An example of spectra from WM and GM for one representative volunteer is demonstrated in Fig. 6.1.

Quantitative analysis consisted in comparison of resonance frequencies of water, tCho, tCr and NAA and evaluation of differences in frequency distances between water and those metabolites for voxels in GM and WM. Resonance frequencies and frequency distances were calculated in each CSI slice from three selected regions of interest (ROI) within VOI: central corresponding to GM voxels, left and right, both correspondingto WM

voxels. Each single ROI consisted in 6 × 2 voxels. Both WM ROI were pooled together, so in total there were 12 voxels associated with GM (single ROI) and 24 with WM (both left and right ROI). The influence of chemical shift displacement was evaluated by comparing the frequency distances between water and metabolites calculated for ROI within the reference slice (no correction for chemical shift displacement) with frequency distances calculated between the ROI in reference slice and ROI in 2nd slice (correction for chemical shift displacement between water and tCho and water and tCr) and frequency distance between the ROI in reference slice and ROI in 3rd slice (correction for chemical shift displacement between water and NAA). Since chemical shift displacement occurred in the caudal direction, resonance frequencies of all metabolites were taken from the reference
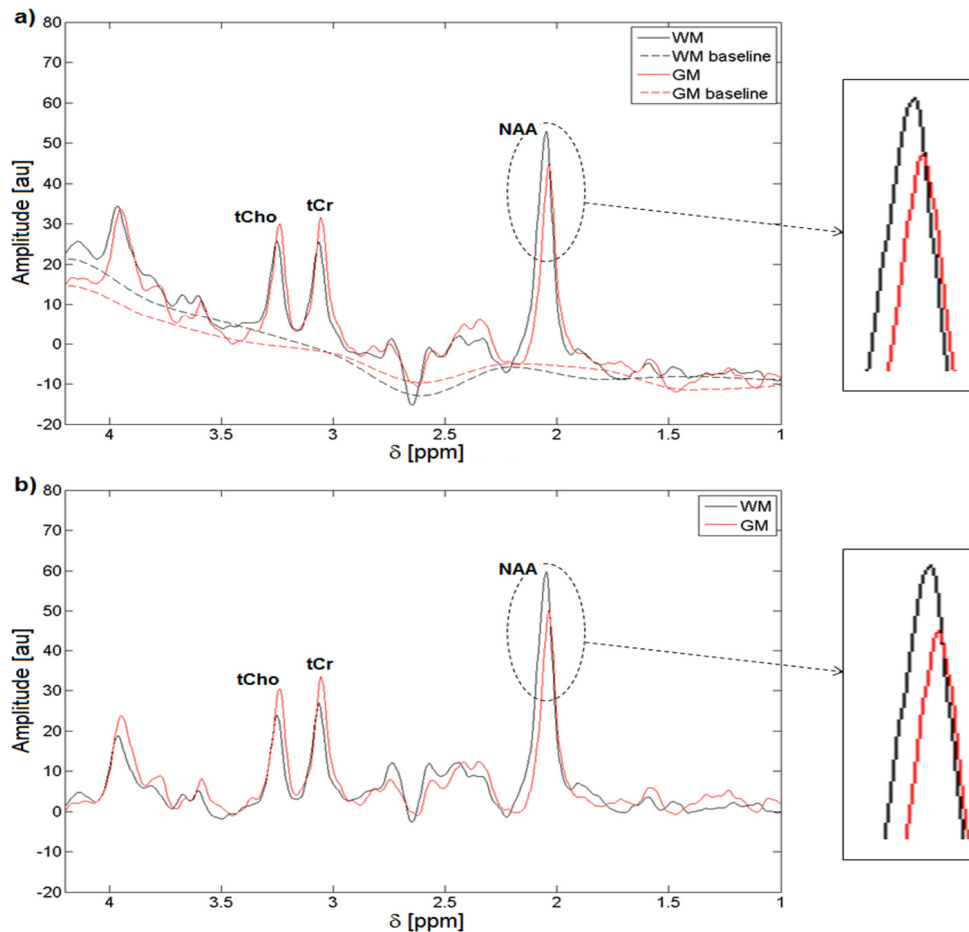

Fig. 6.1: Typical spectra from single voxel in WM (black) and GM (red) from one representative volunteer before (a) and after (b) baseline correction. The upper part of the NAA peak was magnified for better visualization of the differences in peak position.

slice, while resonance frequency of water was taken from the 2nd slice (tCho to water and tCr to water frequency distances) and from the 3rd slice (NAA to water frequency distance).

Prior to calculation of frequency distances, all measured resonance frequencies had to be corrected with respect to the systematic intra-slice differences.

Robustness of calculation of resonance frequencies was improved by baseline evaluation for each spectrum. Assessment of baseline was done with shape-preserving piecewise cubic interpolation, which is a part of the Bioinformatics Toolbox (version 3.4) in Matlab. The resonance frequencies of the water and metabolites were estimated by fitting their peaks with a Gauss function. This was done with a least square root differences approach based on the Nedler-Mead simplex algorithm, which is a part of the Curve Fitting Toolbox (version 2.1) in Matlab.

6.3   Results

Fig. 6.1 shows a comparison of typical spectra from single voxels in WM and GM before (a) and after (b) baseline estimation. Additional chemical shift correction was applied to all spectra so that the water signal was at the same position (4.7 ppm). It can be noticed that all metabolite peaks (tCho, tCr and NAA) have slightly different positions, while after frequency correction the water signals in both spectra had the same position. Moreover, the baseline correction has no influence on this effect. The NAA peak in WM is slightly higher compared to the NAA peak in GM. This is in contradiction to the observed NAA concentration [27] but can be explained by T$_1$ saturation effect, due to the short TR of 1.3 s.

In Fig. 6.2 the average resonance- frequency maps of tCho, tCr, NAA and water are demonstrated. Frequency maps for the metabolites were calculated from the reference slice, while the frequency maps for water from the 2nd and 3rd slices originate from the same localization as the maps for metabolites. Both frequency maps for water are almost identical: areas with higher frequencies are located in both lateral parts (left and right) and in the medial- anterior part of the VOI while the medial- posterior part is associated with lower frequency values. In maps for metabolites higher values of frequency in the medial-

Fig. 6.2: Resonance frequency maps for tCho (a), tCr (b), NAA (c) and water (d, e). All maps were calculated as an average across all measured volunteers. Frequency maps for metabolites (a -c) were calculated from the reference slice while maps for water from 2nd (d) and 3rd (e) slices, so that they all originate from the same location.

anterior part is smaller and for the, medial-posterior part with lower frequencies it is bigger. Even maps for metabolites demonstrate different pattern. In maps for tCho and tCr the region of higher resonance frequencies associated with the medial-anterior part of the VOI is more extensive than for the frequency map for NAA.

Previous finding is confirmed by the frequency profiles seen in Fig. 6.3. In case of water, voxels from the medial part of the VOI were associated with higher frequency

values, whereas for NAA analogous voxels were associated with lower values. For tCho and tCr the increase of frequency in the center of the VOI is compensated by the B_0 field inhomogeneities. This distribution of NAA resonance frequency may correspond to the B_0 field inhomogeneities and appears to show no regional dependence. In contrast to this, frequency profiles of water, tCho and tCr indicate that beside the influence of B_0 field inhomogeneities there is a regional dependency: higher frequencies appear to correspond to GM voxels (medial part of the VOI), while lower frequencies are associated with voxels corresponding to WM (both left and right lateral parts of the VOI).
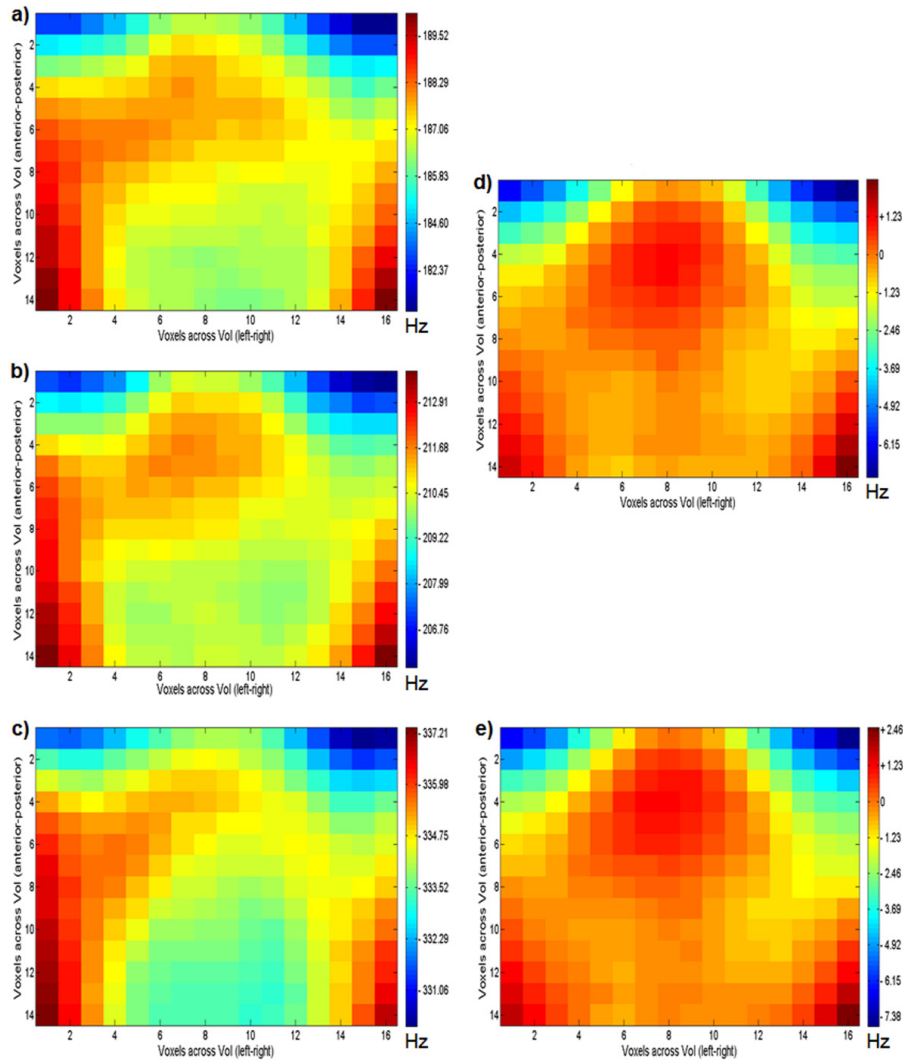

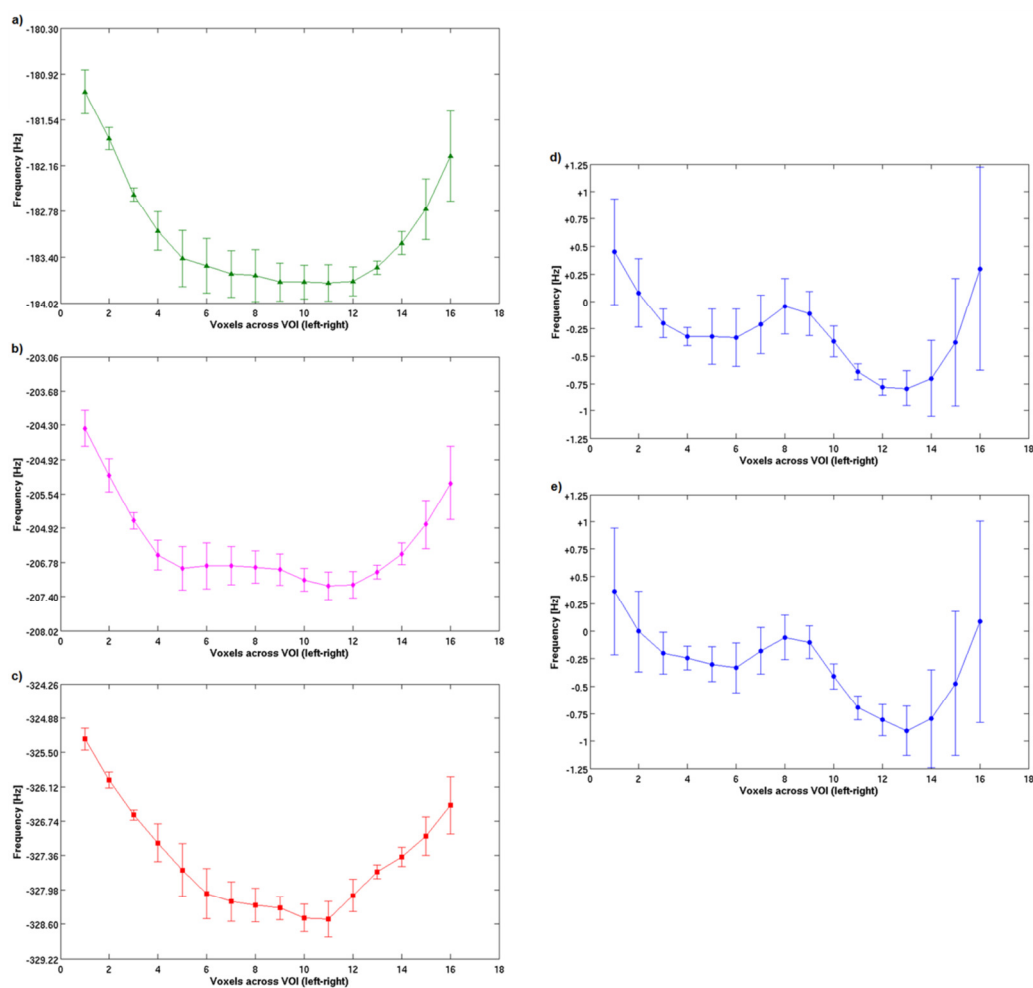Fig. 6.3: Resonance frequency profiles for tCho (a), tCr (b), NAA (c) and water (d, e). Profiles were calculated as an average across all measured volunteers, from rows 8th to 12th of the VOI. Frequency profiles for metabolites (a -c) were calculated from the reference slice while profiles for water from the 2nd (d) and 3rd (e) slices, so that they all originate from the same location.

To minimize the influence of B_0 variations the frequency distance maps between water and tCho, water and tCr and water and NAA (Fig. 6.4) were calculated and used for further analysis. In this case, the effect of B_0 field inhomogeneities on the frequency distance is compensated because both water and metabolite resonances are affected equally. Fig. 6.4 shows localizer images and frequency distance maps for all metabolites calculated without and with correction for chemical shift displacement. Rectangular ROI indicate the voxels from which spectra were included in the quantitative analysis (Fig. 6.4b). It can be seen that maps of frequency distances between water and all metabolites show similar tendencies: frequency distances in the medial part of the VOI are higher compared to both the lateral sides. The most legible differences however, can be noticed for water to NAA frequency distance. Comparison of uncorrected and corrected frequency maps suggests that the correction of chemical shift displacement in slice-selection direction has a minor influence on the frequency distance maps. Both corrected and uncorrected data sets demonstrate similar distribution of frequency distances. This behavior is reproducible for all the measured volunteers.

A comparison of mean values of GM to WM frequency distance differences between water and metabolites calculated without and with correction of chemical shift displacement is illustrated in Fig. 6.5. The frequency distances between water and tCho, water and tCr and water and NAA in all measured volunteers show similar tendencies. A slight movement of the subject's head between the measurements could be the reason for the observed differences between the corrected and uncorrected data sets. The frequency distances between water and metabolites are greater in GM (blue line) compared to WM (green and red lines). Moreover, the GM to WM differences in water to tCho and water to tCr frequency distances are smaller compared to the differences obtained for water to NAA frequency distance. One can see that both uncorrected and corrected data sets show a comparable trend, though the applied chemical shift displacement correction appears to increase the intra-volunteer variations in the frequency distances (especially for WM).
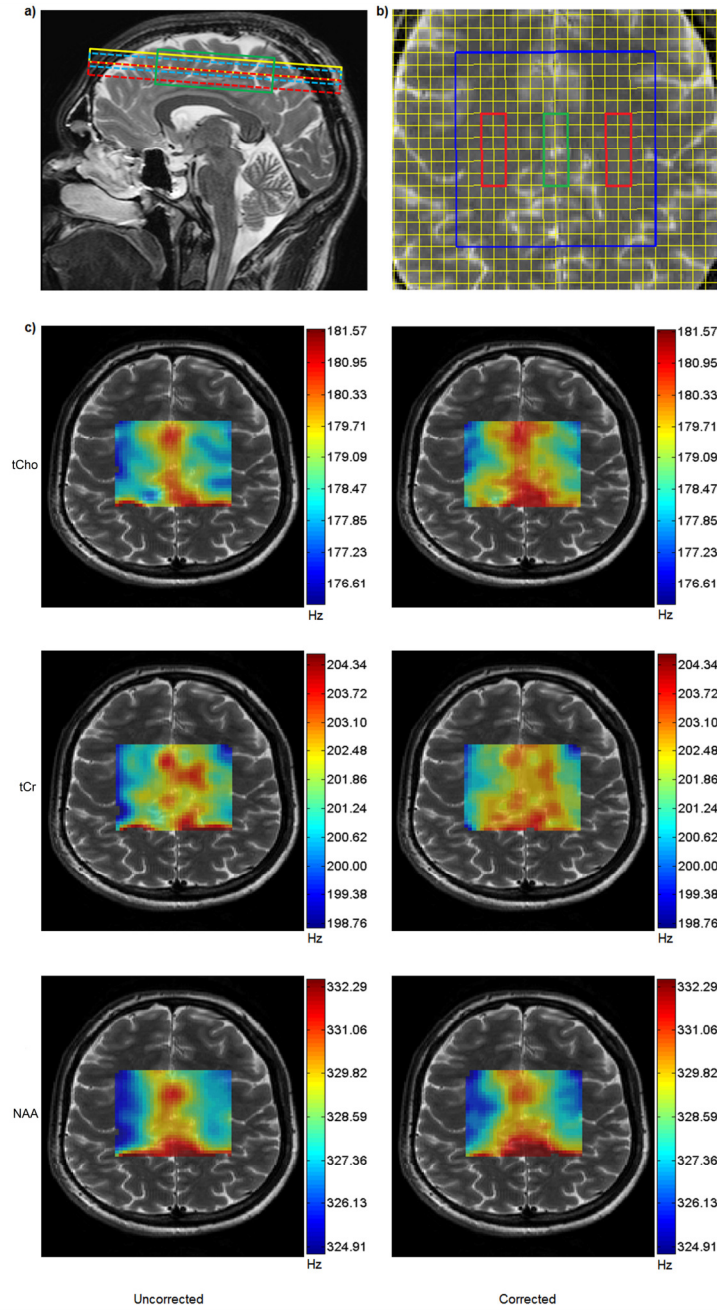
Fig. 6.4: Sagittal localizer (a), transversal localizer (b) and frequency distance maps between water and all measured metabolites (c) calculated without and with chemical shift displacement correction. Sagittal localizer (a) shows the placement of all measured CSI slices (reference slice: solid yellow, 2nd slice- dashed blue and 3rd slice: dashed red) and the adjusted volume (green). Transversal localizer (b) shows the plane of CSI acquisition, VOI (blue square) and the ROI (red: WM, green: GM), from which voxels were included for quantification. For better visualization of the resonance frequencies distribution, the frequency ranges on each map were adjusted individually.

Detailed results of the quantitative analysis are presented in Table 6.1, which contains the mean GM to WM differences in the frequency distances between water and tCho, water and tCr, and water and NAA obtained without and with correction for the chemical shift displacement. In all cases, the frequency distances between water and metabolites were greater for GM than for WM. The highest GM to WM differences were observed for water to NAA frequency distance (13.9±1.9 ppb), while for tCho those differences were approximately 30% less (9.4±2.8 ppb) and for tCr approximately 50% less
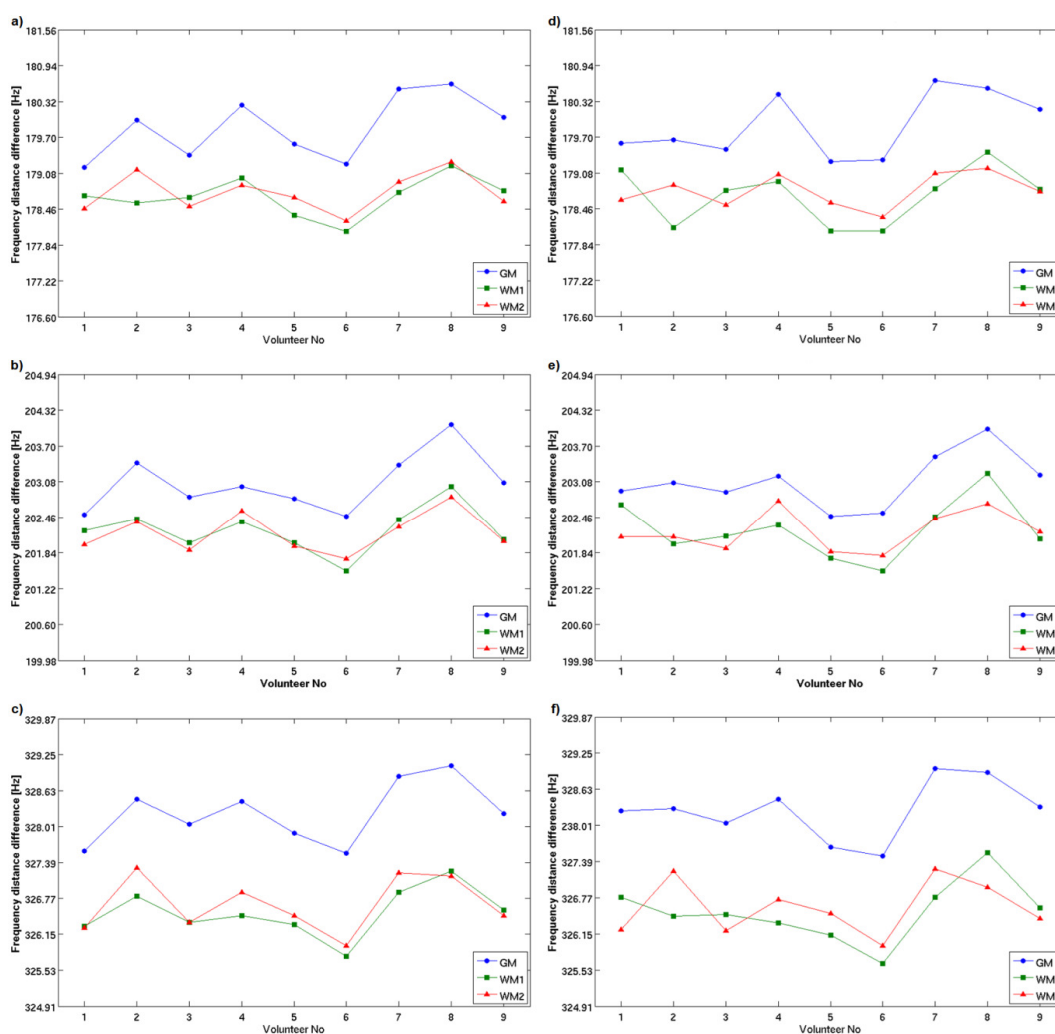
Fig. 6.5: Mean differences in water to tCho (a, d), water to tCr (b, e) and water to NAA (c, f) frequency distances between WM (red and green) and GM (blue). Values were calculated for all measured volunteers, without (a -c) and with (d -f) correction for chemical shift displacement.

(7.2±2.1 ppb). A small movement of the subject's head could cause relatively high values of standard deviations that were calculated for single volunteers. The differences between the uncorrected and corrected mean frequency difference values for single volunteers are higher for water to NAA frequency distance (in the range of 3.2 ppb) than for tCho to water and tCr to water frequency distances (both in the range of 1.5 ppb). However, the differences between the mean values calculated across all volunteers are smaller (in the range of 0.4 ppb). Results in Table 6.1 reveal that the correction for chemical shift displacement leads to an increase of intra-volunteer variations. This is confirmed not only by the plots seen in Fig. 6.4 but also by higher standard deviations across all volunteers after the correction for chemical shift displacement.

Tab. 6.1: Comparison of mean values of differences in water to total choline (tCho), water to total creatine (tCr) and water to NAA frequency distance between GM and WM voxels obtained without and with chemical shift displacement correction.

WM to GM differences	Uncorrected			Corrected		
Volunteer No.	tCho GM - WM [ppb]	tCr GM - WM [ppb]	NAA GM - WM [ppb]	tCho GM - WM [ppb]	tCr GM - WM [ppb]	NAA GM - WM [ppb]
1	5.1 ± 0.9	4.3 ± 1.3	10.7 ± 1.0	4.8 ± 0.2	4.0 ± 1.6	13.9 ± 1.5
2	9.2 ± 0.9	8.0 ± 2.0	11.6 ± 1.7	9.2 ± 1.3	8.1 ± 1.1	11.8 ± 1.3
3	6.4 ± 1.3	6.3 ± 1.2	14.3 ± 0.6	6.7 ± 0.3	6.5 ± 0.7	13.8 ± 1.1
4	9.8 ± 2.0	4.8 ± 1.0	13.1 ± 1.5	10.9 ± 0.4	6.0 ± 1.4	14.6 ± 1.7
5	9.1 ± 0.6	5.9 ± 2.3	12.2 ± 2.4	7.6 ± 1.2	4.4 ± 0.8	10.3 ± 1.4
6	9.4 ± 1.8	7.7 ± 0.8	14.2 ± 0.4	9.4 ± 1.5	7.8 ± 0.5	14.1 ± 1.9
7	13.8 ± 1.3	9.0 ± 1.6	15.5 ± 1.9	14.4 ± 0.9	9.6 ± 1.9	16.7 ± 1.6
8	11.6 ± 0.9	10.1 ± 1.9	15.6 ± 1.6	10.8 ± 1.5	9.2 ± 2.8	14.6 ± 2.1
9	10.4 ± 0.5	9.0 ± 1.9	13.9 ± 0.8	10.7 ± 0.5	9.3 ± 1.7	15.8 ± 2.4
Mean	**9.4**	**7.2**	**13.5**	**9.4**	**7.2**	**13.9**
SD	**± 2.6**	**± 2.0**	**± 1.7**	**± 2.8**	**± 2.1**	**± 1.9**

6.4   Discussion and Conclusions

The aim of this work was to examine whether the known tissue-specific differences in resonance frequency for water also exist for the metabolites: tCho, tCr and NAA. The influence of chemical shift displacement in slice-selection direction on the obtained results was also evaluated. The differences in resonance frequency between WM and GM for water were superimposed by the B_0 field inhomogeneities in CSI measurements, which additionally have a decreased spatial resolution compared to the high-field phase images [15]. Nevertheless, an increase of the water resonance frequency within GM in the central part of the brain could be confirmed (Fig. 6.2 and 6.3). A similar effect for tCho, tCr and NAA is not clearly visible in a direct comparison of the GM and WM regions (Fig. 6.1). Therefore, the frequency differences between water and metabolites within the selected regions were examined.

Calculated frequency distance differences in all cases were higher for voxels associated with GM than for voxels associated with WM. The mean values of the differences between WM and GM calculated across all volunteers (Tab. 6.1) were the highest in case of water to NAA frequency distance. Therefore, the pattern seen on water to NAA frequency distance maps (Fig. 6.4) is the most legible, while the pattern on water to tCho and water to tCr maps appeared to be more dispersed. This behavior could be explained by an analysis of the distribution of resonance frequencies (Fig. 6.2). The patterns seen on average frequency maps for water and all metabolites were influenced by the B_0 field inhomogeneities. However, the average frequency maps of water (Fig. 6.2), tCho, tCr and NAA showed different tendencies. Additional effects, which might influence the resonance frequencies, could explain this behavior. This was confirmed by the average frequency profiles (Fig. 6.3). Both frequency profiles for water frequencies associated with the medial part of the VOI are strongly elevated. Similar behavior can be seen on profiles for tCho and tCr. However, this effect was not as strong for tCho and tCr as it is for water. In contrast, frequency profile for NAA shows no increase of resonance frequencies for voxels corresponding to the medial part of the VOI. These differences in behavior of resonance frequencies of water and metabolites explains why GM to WM differences in

frequency distances for water to tCho and water to tCr are approximately 30% (tCho) and 50% (tCr) lower than for water to NAA.

The resonance frequencies of the evaluated metabolites may be influenced by superimposed signals, like myo-inositol (mI), and Glutamine/Glutamate (Glx). However, at the long TE (144 ms) the amplitude of those additional signals (mI and Glx) is reduced compared to what can be seen at the short TE (30 ms) [28, 29], thus their influence on the main signals (tCho, tCr and NAA) can be neglected. The same is valid for taurine (Tau) [29].

Reduced k-space sampling enlarged the effective voxel size; however, it was necessary for the reduction of the data acquisition time. Larger effective voxel size increases the signal overlap between adjacent voxels [25] and increases the contribution of the signal from tissue water and cerebro-spinal fluid (CSF), especially in the GM spectra. Nevertheless, frequency differences between WM and GM were still observable for all the measured volunteers. In addition, large dimensions of WM and GM ROI ($11.6 \times 34.8 \times 7$ mm^3 each) compared to the nominal voxel size ($5.8 \times 5.8 \times 7$ mm^3) could reduce the influence of this effect.

Correction of chemical shift displacement in slice-selection direction had a minor influence on the obtained GM to WM differences in frequency distances. Chemical shift displacement correction only slightly improved the quality of the frequency distance maps (Fig. 6.4), but it increased the intra-volunteer variations in the differences in frequency distances between the water and metabolites (Fig. 6.5, Tab. 6.1) as well as the intra-slice variations in the resonance frequency of water. This can be caused by insufficient correction of the intra-slice differences in the resonance frequency of water. However, without this frequency correction, the intra-volunteer differences in frequency distances would be even higher. On the other hand the difference in the localization of the slices caused by the chemical shift displacement is from 1.3 mm (tCho, tCr) to 1.9 mm (NAA), therefore the influence of this effect on the obtained results could be neglected.

It was previously shown that resonance frequency may be influenced by temperature [7 -11, 17, 18], pH value [12], proton exchange [16] and susceptibility [13, 15, 19] The differences in water to NAA resonance frequency distances between WM and GM

would correspond to a temperature difference of approximately 1K [8]. The temperature sensitivity for the evaluated metabolites differ maximally by 5% [8]. Therefore, temperature differences are not a likely explanation. Relatively low sensitivity of the endogenous substances to pH changes [12] causes the influence of the pH on tCho, tCr and NAA to be negligible. Theoretically, resonance frequency of water could be affected by the pH changes. However, then the differences in the frequency distances between WM and GM should be the same for all metabolites. This is not the case since the greatest differences between WM and GM is observed for the water to NAA frequency distance (Tab. 6.1). On the other hand, comparable differences in the resonance frequency of water between WM and GM have been shown by phase image studies [13, 15, 19]. He et al. [15] reported an approximate difference of 15.7 ppb. This is very close to the highest difference found in this study (13.9 ppb, Tab. 6.1), which suggest that the resonance frequency of water is shifted while the resonance frequency of NAA appears to be constant. This is in good agreement with Fig. 6.2. The slight difference to the results by He et al. [15] can be explained by the larger voxel size and therefore, higher contribution of partial volume effects.

For that reason, the most probable explanation of the observed GM to WM frequency distance differences are the influences of proton exchange and susceptibility effects also found in the phase images. In addition to phase imaging studies it has been found that not only the resonance frequency of water is influenced but also the resonance frequencies of tCho and tCr. This could explain the smaller differences in values between GM and WM obtained for tCho to water and tCr to water compared to NAA to water frequency distances (Tab. 6.1). It is known that water is present in both extracellular and intracellular spaces, while NAA is characteristic to intraneuronal space [30]. Therefore, different behavior of the three metabolites could be caused by microstructural arrangement of the brain tissue and its alignment to the B_0 field, which according to He et al. [15] may enhance the susceptibility effects. Additionally, in this study, the central part of the brain was examined. In this region, the WM fibers are mostly parallel to the B_0 field (corticospinal tract). In other localizations within the WM, where fibers have different alignment, one could expect different results. Nevertheless, measurements that are more

detailed would be necessary to clarify to what extent those effects contribute to the shifts in the resonance frequencies of water and metabolites.

In conclusion, we demonstrated that in the central part of the brain there are regional differences in frequency distances between the water and metabolites. We also found that chemical shift displacement has a minor influence on the obtained results and therefore, correction of this effect can be neglected. This suggests that the water signal measured with CSI without water suppression may contain relevant information and this can be used not only as an internal reference in absolute quantification. The analysis of unsuppressed spectra can also provide important additional information about tissue-dependent variations of resonance frequencies of water and metabolites.

6.5   Acknowledgments

6.6   References

1. Dong Z, Dreher W, Leibfritz D. Experimental method to eliminate frequency modulation sidebands in localized in vivo ^{1}H MR spectroscopy acquired without water suppression. Magn Reson Med. 2004;51:602-606.
2. Leibfritz D, Dreher W. Magnetization transfer MRS. NMR Biomed. 2001;14:65-76.
3. Chadzynski GL, Klose U. Chemical shift imaging without water suppression at 3T. Magn Reson Imaging. 2010;28:669-675.

4. Clayton DB, Eliott MA, Leigh JS, Lenkinski RE. [1]H spectroscopy without solvent suppression: characterization of signal modulations at short echo times. J Magn Reson. 2001;153:203-209.

5. Hurd RE, Gurr D, Sailasuta N. Proton spectroscopy without water suppression: the oversampled J-resolved experiment. Magn Reson Med. 1998;40:343-347.

6. Nixon TW, McIntyre S, Rothman DL, de Graf RA. Compensation of gradient- induced magnetic field perturbations. J Magn Reson. 2008;192:209-217.

7. Kuroda K, Suzuki Y, Ishihara Y, Okamoto K, Suzuki Y. Temperature mapping using water proton chemical shift obtained with 3D-MRSI: feasibility in vivo. Magn Reson Med. 1996;35:20-29.

8. Zhu M, Bashir A, Ackerman JJ, Yablonskiy DA. Improved calibration technique for in vivo proton MRS thermometry for brain temperature measurement. Magn Reson Med. 2008;60:536-541.

9. Samson RS, Thornton JS, McLean MA, Williams SCR, Tofts PS. ^{1}H-MRS internal thermometry in test-objects (phantoms) to within 0.1 K for quality assurance in long-term quantitative MR studies. NMR Biomed. 2006;19:560-565.

10. Corbett R, Laptook A, Weatherhall P. Noninvasive measurements of human brain temperature using volume-localized proton magnetic resonance spectroscopy. J Cerebr Blood F Met. 1997;17:363-369.

11. Laptook AR, Corbett RJT, Sterett R, Garcia D, Tollefsbol G. Quantitative relationship between brain temperature and energy utilization rate measured in vivo using ^{31}P and ^{1}H magnetic resonance spectroscopy. Pediatr Res. 1995;38:919-925.

12. Coman D, Trubel HK, Rycyna RE, Hyder F. Brain temperature and pH measured by ^{1}H chemical shift imaging of thulium agent. NMR Biomed. 2009;22:229-239.

13. Luo J, He X, d'Avignon DA, Ackerman JJH, Yablonskiy DA. Protein-induced water ^{1}H MR frequency shifts: contributions from magnetic susceptibility and exchange effects. J Magn Reson. 2010;202:102-108.

14. Henkelman RM, Stanisz GJ, Graham SJ. Magnetization transfer in MRI: a review. NMR Biomed 2001;14:57- 64.

15. He X, Yablonskiy DA. Biophysical mechanisms of phase contrast in gradient echo MRI. Proc Natl Acad Sci. 2009;106:13558-13563.

16. Zhong K, Leupold J, von Elverfeldt D, Speck O. The molecular basis for gray and white matter contrast in phase imaging. NeuroImage. 2008;40:1561-1566.

17. Parker DL, Smith V, Sheldon P, Crooks LE, Fussel L. Temperature distribution measurements in two-dimensional MRI imaging. Med Phys. 1983;10:321-325.

18. Childs C, Hiltunen Y, Vidyasagar R, Kauppinen RA. Determination of regional brain temperature using proton magnetic resonance spectroscopy to assess brain-body temperature differences in healthy human subjects. Magn Reson Med. 2007;57:59-66.

19. Dyun JH, van Gelderen P, Li TQ, de Zwart JA, Koretsky AP, Fukunaga M. High-field MRI of brain cortical substructure based on signal phase. Proc Natl Acad Sci. 2007;104:11796-11801.

20. Haacke MA, Cheng NYC, House MJ, Liu Q, Neelavalli J, Ogg RJ, Khan A, Ayaz M, Kirsch W, Obenaus A. Imaging iron stores in the brain using magnetic resonance imaging. Magn Reson Imaging. 2005;23:1-25.

21. Schenck JF, Zimmerman EA. High-field magnetic resonance imaging of brain iron: a birth of a biomarker? NMR Biomed. 2004;17:433-445.

22. Schenck JF. Magnetic resonance imaging of brain iron. J Neurol Sci. 2003;207:99-102.

23. Spees WM, Yablonskiy DA, Oswood MC, Ackerman JJH. Water proton MR properties of human blood at 1.5 Tesla: magnetic susceptibility, T_1, T_2, T_2^* and non-lorenzian signal behavior. Magn Reson Med. 2001;45:533-542.

24. He X, Zhu M, Yablonskiy DA. Validation of oxygen extraction fraction measurement by qBOLD technique. Magn Reson Med. 2008;60:882-888.

25. Groeger A, Chadzynski G, Godau J, Berg D, Klose U. Three-dimensional magnetic resonance spectroscopic imaging in the substantia nigra of healthy controls and patients with Parkinson's disease. Eur Radiol, 2011;21(9):1962-1969.

26. Bernstein MA, King KF, Zhou XJ. Imaging Gradients, in: Bernstein MA, editor. Handbook of MRI pulse sequences, Elsevier Inc, Burlington MA, 2004. p 243-273.

27. Wang Y, Li SJ. Differentiation of metabolic concentrations between gray matter and white matter of human brain by in vivo ^{1}H magnetic resonance spectroscopy. Magn Reson med. 1998;39:28-33.

28. Traeber F, Block W, Lamerichs R, Gieseke J, Schild HH. 1H metabolite relaxation times at 3.0 Tesla: measurements of T1 and T2 values in normal brain and determination of regional differences in transverse relaxation. J Magn Reson Imaging 2004;19:537- 545.

29. Xin L, Gambarota G, Mlynarik V, Gruetter R. Proton T_2 relaxation time of J-coupled cerebral metabolites in rat brain at 9.4T. NMR Biomed. 2008;21:396-401.

30. Moffet JR, Ross B, Arun P, Madhavarao CN, Namboodiri AMA. N-Acetylaspartate in the CNS: from neurodiagnostics to neurobiology. Prog Neurobiol 2007;81:89-131.

Chapter 7:
Conclusions

The aims of this thesis were to develop a robust and reliable non-water-suppressed MRSI technique and to test its performance in *in-vivo* measurements. Since proton spectra acquired without water suppression are hampered by the sideband artifacts [11], in order to achieve the aims it was necessary to optimize the existing measurement techniques, to develop additional postprocessing strategies and to validate the developed technique in *in-vivo* measurements. This has been achieved in three steps. The first step consisted in assessment of the sideband artifacts and investigation of their dependency from the crushing gradients. All the development necessary for *in-vivo* validation of non-water-suppressed CSI was performed within the second step. Finally, in the third step the quantitative analysis of the unsuppressed water signal was performed.

MRSI measurements with spherical water phantom (Siemens, Erlangen, Germany) and with home-build agar phantom confirmed the results from the other studies [11, 50] where a linear dependency between the sidebands and the gradient strength was reported. However, in contradiction to the mentioned literature [11, 50] those measurements revealed that for the used magnet and gradient system (TimTrio, Siemens, Erlangen, Germany) each physical direction of the crusher gradient generates unique pattern of the sidebands, where the greatest artifacts were associated with the gradient in *x*-direction while the smallest with the gradient in *z*-direction. It has been shown that decrease in gradient strength from 11 (default value) to 5 mT/m leads to approximately 30% reduction of all the sidebands without giving a rise in unwanted signals produced during volume selection. Further reduction has been achieved by the removal of the crusher in *x*-direction. The obtained results however are valid for the used MR system and as the pattern of the sidebands for different MR systems may be different, such a decrease of the gradient strength may be difficult to achieve. Nevertheless, with the achieved reduction of sideband artifacts, it could be possible to reduce their remaining part in postprocessing, instead of using special acquisition strategies [12, 50] which may be time consuming or may require additional hardware modifications.

Postprocessing routines developed for the purpose of *in-vivo* non-water-suppressed CSI were successfully applied to spectra acquired from the human brain at long TEs (144 ms). In comparison to the other studies [12, 50, 55], the developed technique is more

straightforward as it uses standard PRESS sequence which is available on most modern MR systems. This method does not require multiple excitations as proposed by Dong et al. [12] or additional hardware modifications as presented by Nixon et al. [50] and is not as time consuming as the oversampling technique proposed by Hurd et al. [55]. The main advantage of the developed technique is the fact that obtained spectra do not require additional manual phase correction, which in the case of CSI measurements may be time consuming and may not be objective. This is because the unsuppressed water signal may be used as a reference for the automated phase correction which is applied by the scanner's software individually to the signals measured by the each channel of the multichannel coil before calculating the final spectrum. If the water signal is distorted or its amplitude is too small the algorithm may not be able to calculate correct coefficients needed for phase correction. There are however two major limitations of the developed technique. The first one is that this method was not successful when applied to the unsuppressed spectra acquired at short TE (30 ms). This is because the number and the amplitude of the sidebands increase with decreasing echo time [11]. The second limitation is related to the homogeneity of the B_0 field. In the presence of large field inhomogeneities, water and sideband peaks will became broader and the presented method may have problems with reduction of the sidebands. This may be overcome by performing manual local shimming. Another problem of the developed approach is the necessity of using water phantom as an external reference for sidebands reduction. However, since sidebands are independent from the load of the patient's bed [50], it is enough to perform new phantom measurements only once for certain geometrical conditions and sequence parameters.

The robustness of the developed technique has been examined in further *in-vivo* experiments. Non-water suppressed spectra were acquired in the human brain at the level of substantia nigra (brainstem) and nucleus dentatus (cerebellum), which are known to be difficult to access with proton MRSI. Additionally, the region of substantia nigra compared to the nucleus dentatus is even more demanding because of the higher content of cellular iron which leads to further increase of magnetic field inhomogeneities [45, 56]. Therefore within those areas only a few studies have been performed which demonstrated limited quality of the obtained spectra [57- 59]. Despite of this fact, spectra acquired in SN and DN

may provide important additional information about pathologies (i.e. Parkinson's disease) [45, 57]. It has been demonstrated that the non-water-suppressed spectra acquired from SN and DN offers good SNR and spectral quality. Since the described postprocessing method offers spectra free from phase problems it was possible to apply the averaging procedure and to calculate the average spectrum. This spectrum showed higher SNR compared to the single one. The gain in SNR was noticed for all volunteers. However, it is important to note that the typical voxel size used in CSI measurements is still bigger than the size of measured anatomical structures therefore, the applied averaging procedure may lead to further increase in partial volume effects. Regardless of the fact that the presented method is limited to the long echo times (TE = 144 ms), CSI without water suppression combined with the developed postprocessing method may be feasible for acquisition in difficult and inhomogenous areas such as substantia nigra and nucleus dentatus. Moreover, lack of the phase problems in acquired CSI spectra allows performing local frequency corrections even for a small voxelsize which enabled the application of the averaging procedure and led to further increase of SNR and spectral resolution. Additionally it is possible to calculate the average spectra for asymmetric areas which can better correspond to certain anatomical structures.

Further in vivo measurements performed in the human brain revealed that there are tissue dependent differences in frequencies of water and metabolite resonances. Since the local distribution of resonance frequencies of water and metabolites were superimposed with the B_0 field inhomogeneities, for further evaluation the frequency distances between water and metabolites were calculated. The analysis of spatial distribution of frequency distances revealed that in all the cases higher values of those frequency distances were associated with GM voxels, while lower values with voxels from WM and the highest GM to WM differences were observed for water to NAA distance. Obtained WM to GM differences in frequency distances were similar to the differences in frequency of the water signal reported in phase image studies [60- 62]. This suggest that the most probable reason for the observed WM to GM differences in the distribution of frequency distances is the influence of proton exchange and susceptibility effects. However, in addition it was found that not only the water signal is affected but also the resonance frequencies of Cho and Cr.

This could explain why WM to GM differences in frequency distances between water and those two metabolites were smaller compared to those obtained for NAA. Moreover, as it is known that NAA is characteristic to intraneuronal space while Cho and Cr are present in both extracellular an intracellular space [63], different behavior of the three metabolites could be caused by microstructural arrangement of the brain tissue and its alignment to the B_0 field, which according to He et al. [61] may enhance the susceptibility effects.

The method presented in this thesis focuses on ^{1}H CSI at long echo times (144 ms) and at field strength of 3 T. The problem connected with the application of the presented technique to the measurements at short echo times remains still unsolved. Nevertheless, CSI measurements at long echo times may still be useful, especially for assessment of the Lac signal, which at longer TE is no longer overlapped with the lipids because of their short relaxation time. Moreover, if the focus is on the three main metabolites (Cho, Cr and NAA), acquisition with long echo times could be advantageous because of the less complicated baseline. Moving to short TE might be realized by a combination of the approach based on minimization of the sideband artifacts by decreasing the strength of the crusher gradients with the technique based on reduction of sidebands by subtraction of the FID measured from the water phantom. This could be verified in the future studies.

Another question to be answered is whether the obtained tissue specific differences in water to metabolite frequency distances would correspond to the direction of the neuronal fibers found in deep white matter of the human brain. This could be realized by a correlation of the differences in frequency distances between water and metabolites accessed with the developed technique with the direction of the neuronal fibers within the WM measured with DTI.

Since several years a strong development of applications for ultra-high field MR scanners can be observed. In recent studies it has been reported that proton MRS is feasible at magnetic fields as strong as 7 [8], 9.4 [9] or even 16.4 T [10]. Since the presented method was developed at field strength of 3 T, another future perspective would be to adapt this technique to the measurements at ultra-high magnetic fields where it could benefit from increased sensitivity in detecting various metabolite resonances.

The results presented in this thesis showed that proton MRSI without water suppression may be a valuable tool as it offers the availability of full water signal which can be used for absolute quantification of the metabolites or for spectral corrections. The strong advantage of the developed technique is that obtained unsuppressed spectra do not require additional phase correction which in the case of multiple voxel measurements may be time consuming. Additionally, full water signal can be accessed and used for absolute quantification without the necessity of performing additional measurements which can increase the total scanning time. Finally, it was demonstrated that the analysis of unsuppressed water signal may provide important additional information, especially about region dependent differences in resonance frequencies. In summary this technique offers strong advantages which may have a high potential to be used in the field of clinics

References

Since the each chapter of the results section has its own literature list, the following list of references describes the literature used in the chapter 1 (Introduction), chapter 2 (Theory) and chapter 7 (Conclusions) of the dissertation.

1. Purcell EM, Torrey HC, Pound RV. Resonance absorption by nuclear magnetic moments in a solid. Phys Rev 1946;69:37-38.
2. Bloch F, Hansen WW, Packard ME. Nuclear induction. Phys Rev 1946;69:127.
3. Bloch F. Nuclear induction. Phys Rev 1946;70:460-473.
4. Brateman L. Chemical shift imaging: a review. AJR 1986;146:971-980.
5. Haacke ME, Brown RW, Thompson MR, Venkatesan R. Magnetic resonance imaging: physical principles and sequence design. New Jork: John Wiley & Sons; 1999.
6. De Graaf RA. In vivo NMR spectroscopy principles and techniques. Chichester West Sussex: John Wiley & Sons; 1998.
7. Ernst RR, Anderson WA. Applications of Fourier transform spectroscopy to magnetic resonance. Rev Sci Instrum 1966;37:93-102.
8. Tkac I, Andersen P, Adriany G, Merkle H, Ugrubil K, Gruetter R. In vivo ^{1}H NMR spectroscopy of the human brain at 7 T. Magn Reson Med 2001;46:451-456.
9. Deelchand DK, Van de Moortele PF, Adriany G, Iltis I, Andersen P, Strupp JP, Vaughan JT, Ugrubil K, Henry PG. In vivo ^{1}H NMR spectroscopy of the human brain at 9.4 T: initial results. J Magn Reson 2010;206:74-80.
10. Hong ST, Balla DZ, Pohmann R. Determination of regional variations and reproducibility in in vivo 1H NMR spectroscopy of the rat brain at 16.4 T. Magn Reson Med 2011;66:11-17.

11. Clayton DB, Eliott MA, Leigh JA, Lenkinski RE. [1]H spectroscopy without solvent suppression: characterization of signal modulations at short echo times. J Magn Reson 2001;153:203-209.

12. Dong Z, Dreher W, Leibfritz D. Experimental method to eliminate frequency modulation sidebands in localized in vivo ^{1}H MR spectroscopy acquired without water suppression. Magn Reson Med 2004;51:602-606.

13. Zhu M, Bashir A, Ackerman JJ, Yablonskiy DA, Improved calibration technique for in vivo proton MRS thermometry for brain temperature measurement. Magn Reson Med 2008;60:536-541.

14. Coman D, Trubel HK, Rycyna RE, Hyder F. Brain temperature and pH measured by ^{1}H chemical shift imaging of thulium agent. NMR Biomed 2009;22:229-239.

15. Lange T. Detection of J-coupled metabolites in magnetic resonance spectroscopy. Zurich: Dissertation; 2007.

16. Marion D, Ikura M, Bax A. Improved solvent suppression in one- and two-dimensional spectra by convolution of time-domain data. J Magn Reson 1989;84:425-430.

17. Sukstanskii AL, Jablonskiy DA, Gaussian approximation in the theory of MR signal formation in the presence of structure- specific magnetic field inhomogeneities. J Magn Reson 2003;163:236-247.

18. Van der Veen J, Weinberger DR, Tedeschi G, Frank JA, Duyn JH. Proton MR spectroscopic imaging without water suppression. Radiology 2000;217:296-300/

19. Lin YY, Hodgkinson P, Ernst M, Pines A. A novel detection- estimation scheme for noisy NMR signals: application to delayed acquisition data. J Magn Reson 1997;128:30-41.

20. Gideon P, Henriksen O, Sperling B, Christiansen P, Olsen TS, Jorgensen HS, Arlien-Soborg P. Early time course of N-acetylaspartate, creatine and phosphocreatine, and compounds containing choline in the brain after acute stroke. A proton magnetic resonance study. Stroke 1992;23:1566-1572.

21. Kugel H, Heindel W, Ernestus RI, Bunke J, du Mesnil R, Friedmann G. Human brain tumors: spectral patterns detected with localized H-1 MR spectroscopy. Radiology 1992;183(3):701-709.

22. Arnold DL, Matthews PM, Francis G, Antel J. Proton magnetic resonance spectroscopy of human brain in vivo in the evaluation of multiple sclerosis: assessment of the load of disease. Magn Reson Med 1990;14(1):154-159.

23. Pouwels PJW, Frahm J. Regional metabolite concentrations in human brain as determined by quantitative localized proton MRS. Mang Reson Med 1998;39:53-60.

24. Corbett RJ, Laptook AR, Tollefsbol G, Kim B. Validation of a noninvasive method to measure brain temperature in vivo using 1H NMR spectroscopy. J Neurochem 1995;64(3):1224-1230.

25. Bates TE, Williams SR, Kaupinen RA, Gadian DG. Observation of cerebral metabolites in an animal model of acute liver failure in vivo: a 1H and 31P nuclear magnetic study. J Neurochem 1989;51(1):102-110.

26. Berridge MJ, Irvine RF. Inositol phosphates and cell signaling. Nature 1989;341:197-205.

27. Ross B, Kreis R, Ernst T. Clinical tools for the 90s: magnetic resonance spectroscopy and metabolite imaging. Eur J Radiol 1992;14:128-140.

28. Ross BD, Bluml S. New aspects of brain physiology. NMR Biomed 1996;9:279-296.

29. Michaelis T, Helms G, Merboldt KD, Hanicke W, Bruhn H, Frahm J. Identification of scyllo-inositol in proton NMR spectra of human brain in vivo. NMR Biomed 1993;6:105-109.

30. Fenstermacher MJ, Narayana PA. Serial proton magnetic resonance spectroscopy of ischemic brain injury in humans. Invest Radiol 1990;25:1034-1039.

31. Behar KL, den Hollander JA, Stromski ME, Ogino T, Shulman RG, Petroff OA, Prichard JW. High-resolution 1H nuclear magnetic resonance study of cerebral hypoxia in vivo. Proc Natl Acad Sci USA 1983;80:4945-4948.

32. Duijn JH, Matson GB, Maudsley AA, Hugg JW, Weiner MW. Human brain infarction: proton MR spectroscopy. Radiology 1992;183:711-718.

33. Vink R, McIntosh TK, Faden AI. Nonedited 1H NMR lactate/n-acetyl aspartate ration and the in vivo determination of lactate concentration in brain. Magn Reson Med 1988;7:95-99.

34. Hwang JH, Graham GD, Behar KL, Alger JR, Prichard JW, Rothman DL. Short echo time proton magnetic resonance spectroscopic imaging of macromolecule and metabolite signal intensities in the human brain. Magn Reson Med 1996;35:633-639.

35. Saunders DE, Howe FA, van den Boogaart A, Griffiths JR, Brown MM. Discrimination of metabolite from lipid and macromolecule resonances in cerebral infarction in humans using short echo proton spectroscopy. J Magn Reson Imaging 1997;7:1116-1121.

36. Mader I, Seeger U, Weissert R, Klose U, Naegele T, Melms A, Grodd W. Proton MR spectroscopy with metabolite-nulling reveals elevated macromolecules in acute multiple sclerosis. Brain 2001;124:953-961.

37. Mader I, Seeger U, Karitzky J, Erb M, Schick F, Klose U. Proton magnetic resonance spectroscopy with metabolite nulling reveals regional differences of macromolecules in normal human brain. J Magn Reson Imaging 2002;16:538-546.

38. Klose U. Measurement sequences for single voxel proton MR spectroscopy. Eur Radiol 2008;67:194-201.

39. Hahn EL. Spin Echoes. Phys Rev 1950;80:580-594.

40. Moonen CTW, von Kienlin M, van Zijl PCM, Cohen J, Gillen J, Daly P, Wolf G. Comparison of single-shot localization methods (STEAM and PRES) for in-vivo proton NMR spectroscopy. NMR Biomed 1989;2:201-208.

41. Bottomley PA, Foster TH, Darow RD. Depth-resolved surface coil spectroscopy (DRESS) for in vivo ^{1}H, ^{31}P and ^{13}C NMR. J Magn Reson 1984;59:338-342.

42. Bottomley PA. Spatial localization in NMR spectroscopy in-vivo. Ann N Y Acad Sci 1987;508:333-348.

43. Maudsley AA, Matson GB, Hugg JW, Weiner MW. Reduced phase encoding in spectroscopic imaging. Magn Reson Med 1994;36:645-651.

44. Skoch A, Jiru F, Bunke J. Spectroscopic imaging: basic principles. Eur Radiol 2008;67:230-239.

45. Groger A, Chadzynski G, Godau J, Berg D, Klose U. Three-dimensional magnetic resonance spectroscopic imaging in the substantia nigra of healthy controls and patients with Parkinson's disease. Eur Radiol, 2011;21(9):1962-1969.

46. Duyn JH, Moonen CT. Fast proton spectroscopic imaging of human brain using multiple spin-echoes. Magn Reson Med 1993;30409-414.

47. Dreher W, Leibfritz D. Parametric multiecho proton spectroscopic imaging: application to the rat brain in vivo. Magn Reson Imaging 1995;13:753-761.

48. Dreher W, Ernhard P, Leibfritz D. Fast three-dimensional proton spectroscopic imaging of the human brain at 3 T by combining spectroscopic missing pulse steady-state free precession and echo planar spectroscopic imaging. Magn Reson Med 2011 [Epub ahead of print].

49. Dreher W, Leibfritz D. Magnetization transfer MRS. NMR Biomed 2001;14:65-76.

50. Nixon TW, McIntyre S, Rothman DL, de Graaf RA. Compensation of gradient-induced magnetic field perturbations. J Magn Reson 2008;192:209-217.

51. Bolan PJ, DelaBarre L, Baker EH, Merkle H, Everson LI, Yee D, Garwood M. Eliminating spurious lipid sidebands in ^{1}H MRS of breast lesions. Mang Reson Med 2002;48:215-222.

52. Eliott M, Clayton D, Lenkinski R. 1H Spectroscopy without water suppression: removal of sideband modulation at short TE. Book of abstracts: Ninth Annual Meeting of the International Society of Magnetic Resonance in Medicine. Glasgow: ISMRM; 2001. p. 1667.

53. Serrai H, Clayton DB, Senhadji L, Zuo Ch, Lenkinski RE. Localized proton spectroscopy without water suppression: removal of gradient induced frequency modulations by modulus signal selection. J Magn Reson 2002;154:53-59.

54. Ozdemir MS, De Denee Y, Achten E, D'Asseler Y, Lemahieu I. Quantitative proton magnetic resonance spectroscopy in the presence of sidebands. IEEE Int. Symposium Biomed. Imag. 2007;4:1008-1011.

55. Hurd RE, Gurr D, Sailasuta N. Proton spectroscopy without water suppression: the oversampled J-resolved experiment. Magn Reson Med 1998;40:343-347.

56. Galazka-Friedman J, Friedman A, Bauminger ER. Iron in the brain. Hyperfine Interact 2009;189:31-37.

57. Hattingen E, Magerkurth J, Pilatus U, Mozer A, Seifried C, Steinmetz H, Zanella F, Hilker R. Phosphorus and proton magnetic resonance spectroscopy demonstrates

mitochondrial disfunction in early and advanced Parkinson's disease. Brain 2009;132:3285-3297.

58. Galanaud D, Le Fur Y, Nicoli F, Denis B, Confort-Gouny S, Ranjeva JP, Viout P, Pelletier J, Cozzone PJ. Regional metabolite levels of the normal posterior fossa studied by proton chemical shift imaging. Magn Reson Mater Phy 2001;13:127-133.

59. Mascalchi M, Brugnoli R, Guerrini L, Belli G, Nistri M, Politi LS, Gavazzi C, Lolli G, Argenti G, Villari N. Single-voxel long TE 1H-MR spectroscopy of the normal brainstem and cerebellum. J Magn Reson Imag 2002;16:532-537.

60. Luo J, He X, d'Avignon DA, Ackerman JJH, Yablonskiy DA. Protein-induced water ^{1}H MR frequency shifts: contributions from magnetic susceptibility and exchange effects. J Magn Reson. 2010;202:102-108.

61. He X, Yablonskiy DA. Biophysical mechanisms of phase contrast in gradient echo MRI. Proc Natl Acad Sci. 2009;106:13558-13563.

62. Dyun JH, van Gelderen P, Li TQ, de Zwart JA, Koretsky AP, Fukunaga M. High-field MRI of brain cortical substructure based on signal phase. Proc Natl Acad Sci. 2007;104:11796-11801.

63. Moffet JR, Ross B, Arun P, Madhavarao CN, Namboodiri AMA. N-Acetylaspartate in the CNS: from neurodiagnostics to neurobiology. Prog Neurobiol 2007; 81:89-131.

Acknowledgments

First and foremost, I would like to thank Professor Uwe Klose for his patience, knowledge and support. He is the best supervisor I ever had and a real 'Doktorvater'.

I would like to thank Dr. Michael Erb and Bernd Kardatzki for their assistance in Matlab and C/C++ programing. Without them learning the principles of those programing languages would take much more time.

Many thanks to Dr. Adriane Gröger for her help in preparation of the thesis and for valuable comments to the thesis and to my manuscripts.

I would like to acknowledge Filip Jiru from the MR Unit in the Department of Diagnostic and Interventional Radiology at Institute for Clinical and Experimental Medicine in Prague, Czech Republic for his help in software development.

I would also like to acknowledge Professor Dmitriy Jablonskiy from Mallinckrodt Institute of Radiology at Washington University in St. Louis (MO), USA for a valuable discussion we had during his visit in Tübingen.

My thanks go to Barbara Wasserka and to Franziska Hoesl for their support in dealing with all the administrative issues. Without them and with my lack of skills in German, this would be extremely difficult.

Many thanks to our technical assistants: Mathias Röger, Cornelia Veil and Albertine Stiens. I would like to acknowledge them for their assistance during the measurements.

Last but not least, I would like to thank to my parents for their support in difficult moments of my life. Dear Parents, I would like to apologize for the fact, that due the nature of my work we cannot see each other as frequent as we would like to.

I would like to dedicate this thesis to Marta, who is the most important woman in my life.

Curriculum Vitae

Grzegorz Łukasz Chądzyński

24.02.1983, Katowice, Poland

School Education

09.1990-06.1998	Primary School, Kłobuck, Silesian Voivodship, Poland
09.1998-06.2002	High-School, Kłobuck, Silesian Voivodship, Poland

Higher Education

10.2002-07.2005	Bachelor Studies, Department of Medical Physics, Faculty of Mathematics, Physics and Chemistry, University of Silesia, Katowice, Poland
10.2005-9.2007	Master Studies, Department of Medical Physics, Faculty of Mathematics, Physics and Chemistry, University of Silesia, Katowice, Poland
Since 10.2007	PhD studies (**Dr. sc. hum**), Faculty of medicine, Eberhard-Karls Universität, Tübingen, Germany

Professional Experience

07.2004-08.2004	Student's apprenticeship (Computed Tomography and Magnetic Resonance Imaging), Silesian Center of Diagnostic Imaging HELIMED, Katowice, Poland
10.2007-12.2008	Scientific co-worker, EU Marie Curie host fellowship, Section for Experimental MRI of CNS, Department of Diagnostic and Interventional Neuroradiology, Universitätsklinikum ,Tübingen, Germany
01.2009-09.2011	Scientific co-worker, MR Research Group, Department of Diagnostic and Interventional Neuroradiology, Universitätsklinikum, Tübingen, Germany
Since 10.2011	Scientific co-worker, Department of Neuroimaging and MR Physics, Universitätsklinikum and guest scientist, Department of Ultra-High Field Magnetic Resonance, Max Planck Institute for Biological Cybernetics, Tübingen, Germany

Appendix: Declaration of Contribution of Coauthors to the Publications

In this appendix all the publications used for this dissertation are listed in the chronological order. The list includes the title of the publication, all the coauthors together with description of their contribution to the manuscript, and the name of the journal in which the manuscript was published.

"Chemical Shift Imaging without Water Suppression at 3T". <u>Grzegorz L. Chadzynski</u>, Uwe Klose. Published in June 2010 in Magnetic Resonance Imaging (Magn Reson Imaging 2010; 28:669-675).

The first author performed all the MRSI measurements, all the software development, the entire data postprocessing and wrote the manuscript. Professor Klose contributed to the development of software necessary for data postprocessing and evaluation. Moreover he aided with the interpretation of the results and assisted during corrections of the manuscript.

"Tissue Specific Resonance Frequencies of Water and Metabolites within the Human Brain". <u>Grzegorz L. Chadzynski</u>, Benjamin Bender, Adriane Groeger, Michael Erb, Uwe Klose. Published in September 2011 in Journal of Magnetic Resonance (J Magn Reson 2011;212:55-63).

The first author performed all the MRSI measurements, all the software development, data postprocessing and wrote the manuscript. Dr. Erb and Professor Klose contributed to the software development necessary for data evaluation. Additionally,

Professor Klose aided with physical interpretation of the results. Dr. Groeger and Dr. Bender assisted in medical interpretation of obtained results. All the coauthors assisted during the manuscript preparatios and corrections.

"Evaluation of Gradient Induced Sidebands for the Purposes of Proton Chemical Shift Imaging without Solvent Suppression". Grzegorz L. Chadzynski, Uwe Klose. Submitted in October 2011 to Magnetic Resonance Imaging (current status: under review).

The first author of this manuscript was responsible for the all the MRSI measurements, for data postprocessing done for this manuscript and prepared the publication. Professor Klose assisted in data evaluation and interpretation of the results. Moreover, he assisted during manuscript preparations and corrections.

"High Resolution Chemical Shift Imaging of the Human Brainstem and Cerebellum without Water Suppression at 3 T". Grzegorz L. Chadzynski, Uwe Klose. Currently under preparations, will be shortly submitted. Parts of the results presented in this manuscript has been already published in the book of abstracts of 'World Congress on Medical Physics and Biomedical Engineering' conference (Proceedings IFMBE 2009;25/2:177-180).

The first author performed all the MRSI measurements and data postprocessing necessary for this manuscript and prepared the text. Professor Klose aided in data evaluation and interpretation of the results. Moreover, he assisted during manuscript preparations and corrections.